Jiun-Lin Yan

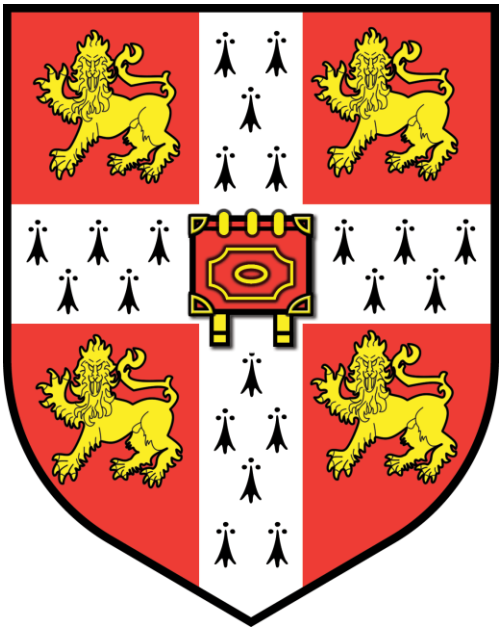

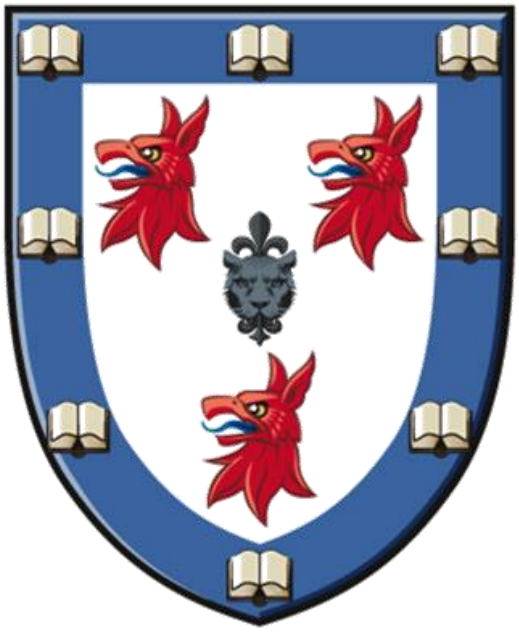

Cambridge Tumour Imaging Laboratory,

Division of Neurosurgery,

Department of Clinical Neuroscience,

and Homerton College,

University of Cambridge

Characterising Peritumoural Progression of Glioblastoma using Multimodal MRI

June 2017

This dissertation is submitted for the degree of Doctor of Philosophy

To Jade, with love

Declaration

- This dissertation is the result of my own work and includes nothing which is the outcome of work done in collaboration except as declared in the Preface and specified in the text.
- It is not substantially the same as any that I have submitted, or, is being concurrently submitted for a degree or diploma or other qualification at the University of Cambridge or any other University or similar institution except as declared in the Preface and specified in the text. I further state that no substantial part of my dissertation has already been submitted, or, is being concurrently submitted for any such degree, diploma or other qualification at the University of Cambridge or any other University or similar institution except as declared in the Preface and specified in the text
- It does not exceed the prescribed of 60,000 words limit.

Abstract

Title: Characterising Peritumoural Progression of Glioblastoma using Multimodal MRI

Jiun-Lin Yan

Glioblastoma is a highly malignant tumor which mostly recurs locally around the resected contrast enhancement. However, it is difficult to identify tumor invasiveness pre-surgically, especially in non-enhancing areas. Thus, the aim of this thesis was to utilize multimodal MR technique to identify and characterize the peritumoral progression zone that eventually leads to tumor progression.

Patients with newly diagnosed cerebral glioblastoma were included consecutively from our cohort between 2010 and2014. The presurgical MRI sequences included volumetric T1-weighted with contrast, FLAIR, T2-weighted, diffusion-weighted imaging, diffusion tensor and perfusion MR imaging. Postsurgical and follow-up MRI included structural and ADC images.

Image deformation, caused by disease nature and surgical procedure, renders routine coregistration methods inadequate for MRIs comparison between different time points. Therefore, a two-staged non-linear semi-automatic coregistration method was developed from the modification of the linear FLIRT and non-linear FNIRT functions in FMRIB's Software Library (FSL).

Utilising the above mentioned coregistration method, a volumetric study was conducted to analyse the extent of resection based on different MR techniques, including T1 weighted with contrast, FLAIR and DTI measures of isotropy (DTI-p) and anisotropy (DTI-q). The results showed that patients can have a better clinical outcome with a larger resection of the abnormal DTI q areas.

Further study of the imaging characteristics of abnormal peritumoural DTI-q areas, using MRS and DCS-MRI, showed a higher Choline/NAA ratio (p = 0.035), especially higher Choline (p = 0.022), in these areas when compared to normal DTI-q areas. This was indicative of tumour activity in the peritumoural abnormal DTI-q areas.

The peritumoural progression areas were found to have distinct imaging characteristics. In these progression areas, compared to non-progression areas within a 10 mm border around the contrast enhancing lesion, there was higher signal intensity in FLAIR (p = 0.02), and T1C (p < 0.001), and there were lower intensity in ADC (p = 0.029) and DTI-p (p < 0.001). Further applying radiomics features showed that 35 first order features and 77 second order features were significantly different between progression and non-progression areas. By using supervised convolutional neural network, there was an overall accuracy of 92.4% in the training set (n = 37) and 78.5% in the validation set (n=14).

In summary, multimodal MR imaging, particularly diffusion tensor imaging, can demonstrate distinct characteristics in areas of potential progression on preoperative MRI, which can be considered potential targets for treatment. Further application of radiomics and machine learning can be potentially useful when identifying the tumor invasive margin before the surgery.

CONTENTS

Acknowledgement

I am so grateful for all the instruction and supervision from my supervisor, Mr. Stephen Price who not only leads me into academic neurosurgery but also provide me plenty of material for research. As a neurosurgeon, I learn the way to do research together with clinical service at same time from my supervisor which need to devote great effort. He told me that the purpose of the Ph.D. is to learn how to answer a good question completely which may need a thorough study design and step by step approach. In addition, Mr. Stephen Price always be very supportive and friendly to my research and my life in Cambridge.

To Cambridge Brain Tumour Imaging Laboratory

Dr. Timothy Larkin was the post-doc in our lab who provide great help in imaging analysis and computer science. He taught me not only the Matlab function and Unix function from scratch, but also the application of the programing into imaging analysis. Moreover, he kept helping even after he returned to Australia.

Dr. Natalie Boonzair is my senior PhD student who graduated from our lab in 2016. I am very thankful to have her teach me and share everything she know to me. Many of the materials in the thesis, such as patient characteristics were collected by Natalie. Besides for the research methods, she also helps me a lot in writing which is one of my weakness.

I also like to thank Dr. Anouk van der Hoorn, a visiting researcher and radiologist from the University of Groningen, Netherland. Her enthusiasm in research kept my research going. She introduced many techniques in the radiology field in to my thesis and together we finished several studies including the coregistration methods, the perioperative ADC change in GBM, and the extent of resection study.

Danial Fountain is a visiting medical student in our lab, although not for a long period, he together with Timothy Larkin develop a 3D voxel wise approach in MRS data retrieve. Bart van Dijken, a visiting junior medical doctor from the University of Groningen, Netherlands. He spent many efforts in doing several imaging preprocessing and we had done some progress on the imaging study of the subventricular zone.

I would like to thank Chao Li for all the discussion, learning and teaching in the advanced computation imaging analysis such as radiomics or machine learning. Since these are not well established, he help me through many of the techniques together.

To Department of Clinical Neuroscience, Wolfsan Brain Imaging Center and Department of Radiology

I would like to thank Professor Joe Herbert, Dr. Adrian Carpenter, and Dr. Ruma Raha-Chowdhury for the guidance for my PhD life and good constructive feedback from every student seminar presentation and the annual review. Special thanks to Dr. Adrian Carpenter that help me go through my personal difficulty when my family needed back in Taiwan in the middle of the PhD.

I wish to thank Dr. Tomasz Mayts from the department of Radiology for collecting many of the follow up data from various source. He also provided several critical feedbacks as a radiologist to my study. I also like to thank Dr. Guy Williams to guide me through several obstacles in both MR physics and Matlab coding.

To my family

I am so grateful that all my family members encouraged me to study in Cambridge. Their supports are not only mental but also substantial. Since both my parents studied abroad in their early life, their understanding and help are tremendous. My wife, Jade

Lin, selfless supportive me all the time as my strongest backup in every aspect of my life. And I would also like thank to all the family member (Justin Chang, Alice Yan, Johnny Chen…) for their support.

To my finding body Chang Gung Medical Foundation

The Chang Gung Medical Foundation, Chang Gung Memorial Hospital provides the majority of the financial support for me to study in Cambridge. All my tuition fee, and part of the daily expense were supported through the foundation. Here, I would like to thank all my teachers in the department of Neurosurgery, Chang Gung Memorial Hospital who encourage me to study further. And I also like to thank secretaries of Keelung Chang Gung Memorial Hospital for all the administration works.

Lastly, I would like to expression my deepest gratitude to all the patients who devote themselves into medical research. Without their participation, this study can never be done. Since there is no additional treatment benefit, their volunteer showed their great love and contribution to the GBM research.

Abbreviations

2-HG	2-hydroxyglutatrate
5-ALA	5-aminolevulinic acid
ADC	Apparent diffusion coefficient
ATRX	ATP-dependent helicase
BCNU	1,3- bis (2-chloroethyl)-1-nitrosourea
CCRT	concomitant chemoradiotherapy
CE	T1 weighted contrast enhanced
Cho	Choline
CNN	Convolutional neural network
CT	Computed tomography
CTV	Clinical target volume
DCE-MRI	Dynamic contrast enhanced MRI
DICOM	Digital Imaging and Communications in Medicine
DIR	Difformation Imaging Registration
DTI	Diffusion tensor imaging
DSC-MRI	Dynamic susceptibility contrast MRI
DWI	Diffusion weighted imaging
EGFR	Epidermal growth factor receptor
EOR	Extent of resection
FA	Fractional anisotropy
FDT	FMRIB's diffusion toolbox
FLAIR	Fluid-attenuated inversion recovery
FSL	FMRIB Software Library
GBM	Glioblastoma
GTR	Gross total resection
GLCM	Gray level co-occurrence matrix
GTV	Gross target volume
IDH	Isocitrate dehydrogenase
KPS	Karnofsky performance score
MD	Mean diffusivity
MGMT	O^6-methylguanine DNA methyltransferase
MPRAGE	Magnetization-prepared rapid gradient-echo
MRI	Magnetic resonance imaging
MRS	Magnetic resonance spectroscopy
MTT	Mean transit time
NAA	N-acetyl aspartate

NADPH	Nicotinamide adenine dinucleotide phosphate
NAWM	Normal appearing white mater
NF1	Neurofibromatosis type 1
Nifti	Neuroimaging Informatics Technology Initiative
OS	Overall survival
PET	Positron emission tomography
PFS	Progression free survival
PpIX	Protoporphyrin IX
PTEN	Phosphatase and tensin homolog
PTV	Planning-target volume
RANO	Response assessment in neuro-oncology
rCBF	Relative cerebral blood flow
rCBV	Relative cerebral blood volume
RMS	Root mean square
ROI	Regions of interest
RTOG	Radiation therapy oncology group
SSIM	Structure Similarity Map
STR	Subtotal resection
TERT	Telomerase reverse transcriptase
TP53	Tumour protein 53
TTP	Time to peak
VEGF	Vascular endothelial growth factor
WBIC	Wolfson Brain Imaging Center

CHAPTER 1

Introduction

1.1 Background and Epidemiology

Epidemiology

Glioblastoma (GBM) is the most aggressive and the most common malignant primary brain tumour. The overall age adjusted incidence in England is 4.64 per 100,000 population,[14] and 3.19/100,000 in United States and further causes up to 256,213 deaths annually worldwide.[94] Although the overall incidence is lower than other common cancers of the body, its mortality rate is higher than most of the other cancers, and is the number one cause of death in cancer patients under 40 years old. Furthermore, the prognosis of GBM is poor, the median overall survival (OS) including patients without any treatment regime is only 6.1 month.[14] With the extensive standard multimodal treatment schemes including maximal, safe surgical resection followed by radiotherapy with concomitant and adjuvant temozolomide chemotherapy, the median OS can only increase to about 14.8 month, and one, 2 and 5 years overall survival are only 64.3%, 28.7% and 6.6% respectively.[14]

Risk factors

The exact cause of GBM is unknown. A systemic review focusing on occupational and environmental risk factors showed that exposure to ionizing radiation, high voltage power lines and agriculture pesticides were the possible risk factors for malignant brain tumour.[38] However, most GBM cases were sporadic, and only about 5% of the GBM

patients had family history of glioma, and some of these familial type were reported to be associated with rare genetic syndrome such as Li-Fraumeni syndrome, Lynch syndrome, Turcot's syndrome and neurofibromatosis type1 and 2.[93,160]

Symptoms of GBM

Headache is the most common symptom of GBM, however, it is usually non-specific. Associated headache characteristics includes, recent onset with progressive increase in severity and frequency, morning headache, accompanied with focal neurologic sign, seizure, age more than 50 years old may be red flags of GBM. Other symptoms such as nausea, vomiting, gait disturbance, cognitive changes or urinary incontinence can also be seen in GBM patients.[92] As these are common features to present to primary care, much interest at present focuses on the combination of symptoms for the early detection of brain tumours.

1.2 Pathology and the Biologic Basis of GBM

1.2.1 The Emerging of Pathology Diagnosis

Glioblastoma is a highly diverse and complex malignant brain tumour. Traditionally, the diagnosis of GBM was largely based on histopathology findings, including hypercellularity, nuclear atypia, cellular pleomorphism, mitotic activity, microvascular proliferation and necrosis[160]. However, these microscopic findings were unable to explain the variation of patients' prognosis in the same category. The entity of GBM is now clearer due to the advance in genomic technology. In 2008, the TCGA research network identified and validated several commonly mutated genes in GBM, such as tumour protein 53 (*TP53*), phosphatase and tensin homolog (*PTEN*), neurofibromosis type 1 (*NF*1), epidermal growth factor receptor (*EGFR*), human epidermal receptor growth factor 2 (Her2/ ErbB2), retinoblastoma protein (RB1), PIK3R1, and PIK3CA by using large scale multidimentional analysis[15]. In 2010, Verhaak proposed a robust gene expression-based molecular classification of GBM into classical, mesenchymal, proneural and neural type according to the aberration and expression of *EGFR*, *NF*1, and platelet derived growth factor receptor alpha (*PDGFA)*/ Isocitrate dehydrogenase-1 *(IDH*1).[153] Although not statistically significant, a slightly better clinical prognosis was observed in the proneural type. In 2016, an update of WHO GBM classification firstly incorporate molecular markers, such as *IDH* mutation status, into classification for GBM.[74] The 1p/19q co-deletion, together with *IDH* mutation as suggested an essential criterion to diagnose oligodengroglioma, and K27 mutation in the histone H3 gene H3F3A is for the diagnosis of diffuse midline glioma that are commonly seen in children/young adults. The emergence of molecular biomarkers can provide us a better way for subdividing GBM to hopefully help with diagnosis and treatment.

1.2.2 Origin of GBM and molecular biomarkers

The cell origin of the glioma remains a complicated topic. Many genetic alterations have been identified[155] as being responsible for transforming a normal neural stem cell, stem cell derived astrocyte, or oligodendrocyte progenitor cell to a cancer cell.[160] Two major pathways of the transformation of GBM from precursor cell, primary and secondary, were identified (Figure 1.1)[155].

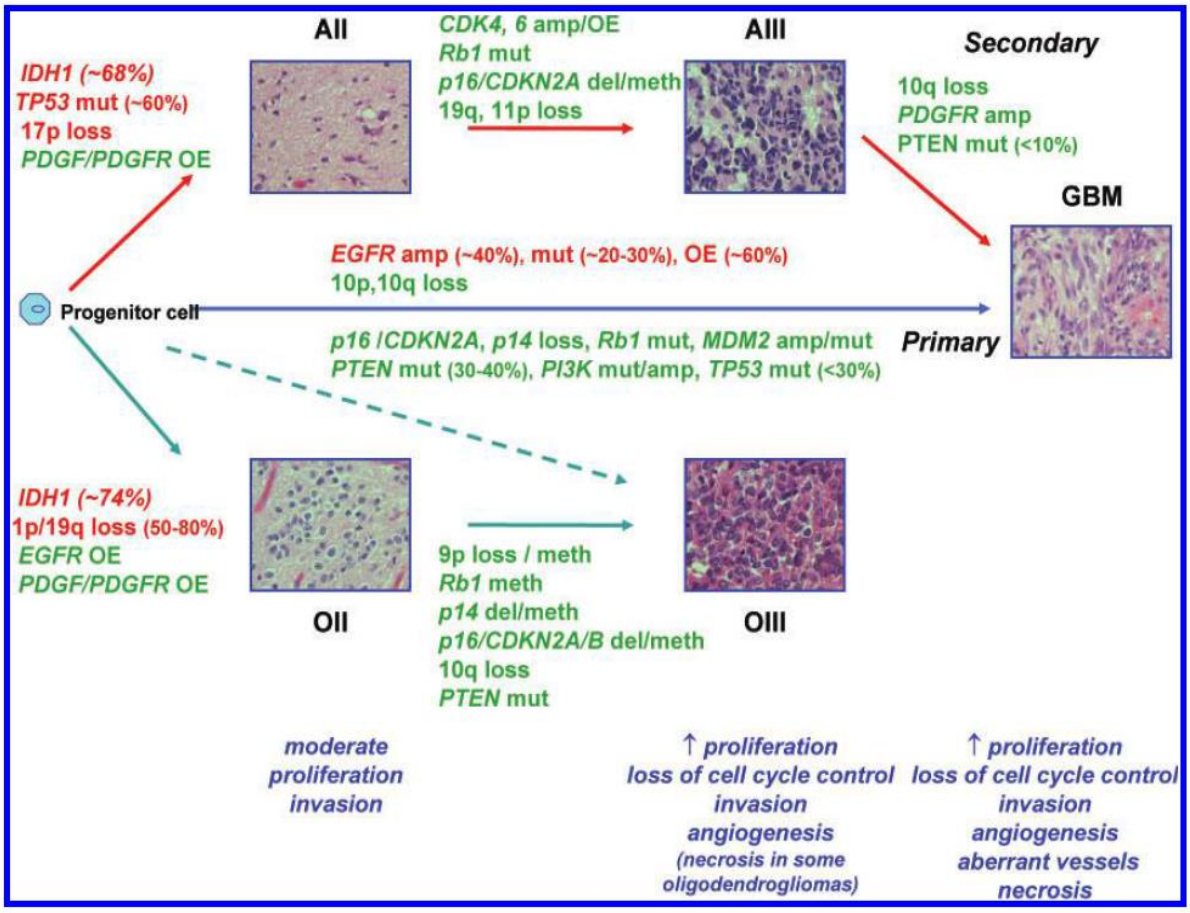

Figure 1.1

This figure shows primary and secondary malignant transformation pathway from progenitor cells into GBM.

(The British Journal of Radiology, 84 (2011), S90–S106)

IDH-wild type GBM

Primary GBM, or *IDH*-wild type GBM, which arises de novo and is associated with *EGFR* proto-oncogene amplification, *PTEN*, tumour suppressor gene mutation and telomerase reverse transcriptase (*TERT*) promoter mutation.[2] The *IDH*-wild type GBM accounts for 90% of the GBM and occurs more in the older population (~ 62 years old) with a worse prognosis.

One of the most important mutation is the amplification of *EGFR* which occurs in 35% of all *IDH*-wild type primary GBM and only exceptional case in *IDH*-mutant.[74] However, the Radiation Therapy Oncology Group (RTOG) 0211 phase I/II trial with gefitinib (an *EGFR* tyrosine kinase inhibitor) for concurrent chemo- radiotherapy showed that the median survival is no better than historical control cohort treated with radiation alone[18]. This is due to about half of the tumours with *EGFR* amplification expressed *EGFRvIII* which is the active form of *EGFR* that promote tumour growth. Further immunotherapy targeted on EGFRvIII-positive GBM by using Rindopepimut™ (a EGFRvIII peptide vaccine) showed a promising result on phase II clinical trial[123]. However, a recent phase III study showed no benefit on OS[53].

PTEN, is another gene mutation involve in about 24% of the primary GBM. It is a tumour suppressor gene that down regulates the phosphatidylinositol 3-kinase pathway that involves the cellular apoptosis and proliferation.[160]

Human telomerase reverse transcriptase (*TERT*) promoter mutation is also a common mutation in primary GBM, which occurs in about 72% of the cases but less frequent in secondary GBM and pediatric GBM. The telomerase normally regulates the length of DNA which further affect the life cycle of the cell. Studies had shown that *TERT* mutation is an independent poor prognostic risk factor in all primary GBM, and the authors suggest a more aggressive treatment for these patients.[127]

***IDH*-mutation GBM**

The secondary GBM, diagnosed with IDH-mutation, have more frequent mutation in TP53, and ATP-dependent helicase (ATRX).[2] It arises from the malignant transformation of anaplastic astrocytoma or diffuse astrocytoma. The secondary GBM accounts for 10% of all GBM, it occurs more in young patients (~44 years old), and locates more in frontal lobe. It has a better prognosis, compared to primary GBM. The most common is the point mutation in codon 132 of IDH-1 or less commonly in codon 172 of IDH-2) is the most distinctive markers of secondary GBM[99] and the diagnostic criteria for oligodendroglioma. There are different types of the R132 mutation in IDH-1, including the most prevalent R132H (CGT arginnine→ CAT histine), followed by R132C, R132L, R132S and R132G. The main functions of IDH-1 are the lipid synthesis and the cellular glucose sensing. The detection of the IDH-1 mutation can be done by using immunochemistry staining or DNA sequencing and the concordance between this two methods was 99-99%[171]. IDH-1 is the catalytic enzyme oxidase carboxylation of isocitrate to α-ketoglutarate and resulting in the increase of nicotinamide adenine dinucleotide phosphate (NADPH) from NADP+ which further prevent cell damage from oxidative stress and irradiation injury.[42] Therefore, a mutation in IDH-1 can cause the decrease production of NADPH and α-ketoglutarate which further increase the sensitivity to chemo- radiotherapy. In addition, tts neoformic activity leads to the transformation of α-ketoglutarate to 2-hydroxyglutatrate (2-HG) which further interfere with normal epigenetic regulation of cells[42], for example, induce the hydroxylation of the hypoxia-inducible factor-1α subunit resulting tumourogensis in hypoxic environment[168].

A less common gene abnormality is the *PDFRA* gene. There is approximately 30% of all glioma have the amplification of *PDGFRA*. It is the most important characteristics

in the proneural type GBM.[95] This gene plays an important role in organ development, wound healing and tumour progression. Amplification of *PDGFRA* and *PDGF* can result in the stimulation of glial tumour cell via autocrine and paracrine loop.[87]

Neurofibromatosis type 1 gene (*NF1*) loss or mutated in about 15% of all GBM, and mostly in the mesenchymal type of GBM. It is a tumour suppression gene that produces neruofibromin 1 which further negatively regulates *Ras* and *mTOR* pathway. Therefore, loss of *NF1* can result in the development of mesenchymal GBM.

Except for the *IDH* mutation status, one of the most clinical important marker is the methylation of the O^6-methylguanine DNA methyltransferase (*MGMT)* promoter. *MGMT* is a DNA repairing gene that modulates the effect of alkylating agent. It can restore guanine from O-6-methyguanine which is induced by the chemotherapy. Therefore, the GBM become more vulnerable to DNA damage from radiotherapy or chemotherapy after the methylation of MGMT promoter. Studies have shown that MGMT methylation is an independent favorable outcome predictor for GBM patients treated with temozolomide concomitant chemoradiotherapy (median survival 21.7 months versus 15.3 months).[46] In further 5 years follow up of the EORTC-NCIC phase III trial also showed this benefit can last for up to 5 years.[138] In addition, MGMT methylation status also correlates with the pattern of GBM progression after treatment. In a study of 79 recurrent GBM, 51 out of 63 *MGMT* promoter unmethylated patients had local recurrent GBM, whist 11 out of 33 *MGMT* promoter methylated patients were locally recurred.[13]

1.2.3 Mechanism of GBM invasion

Most of the GBMs will recur within 1-2 cm of the primary site after surgical resection[101,125]. It rarely metastasizes outside of the central nervous system due to short survival time, blood-brain-barrier, and local immune system. In 1938, Dr. Scherer published a systemic study in the invasion of high grade glioma based on the pathology observation.[121] He proposed that glioma invades through secondary structures, (1) perineural and neuronophagic growth (brain parenchymal invasion), (2) surface growth (subarachnoid invasion), (3) perivascular growth, and (4) perifascicular growth (white mater invasion).

These findings may tell us where the GBM goes, however, the progression of the GBM has two key factors: proliferation and migration[165]. In this “going and growing” theory[8] suggests that, GBM cells migrate less when in the highly proliferation status (“growing” phenotype), and the highly proliferative GBM cells are less invasive. The changing between this two phenotypes are largely determined by the environmental factors through various pathways. For example, with radiotherapy, chemotherapy or hypoxia, the GBM cells may adapt from the proliferation phenotype to a migration phenotype which further complicated the treatment by promoting invasion.

The primary source of GBM invasiveness can be explained by the cancer stem cell hypothesis[21]. The main idea is that GBM, in some circumstances, is transformed from the neuroprogenitor cells or stem cells that has the ability to migrate through the whole brain. After this transformation, these cancer cells can still migrate as the neuroprogenitor cells,[21] and actively seek out vessels and migrate alone with them. In addition, it will secrete glutamate as a growth factor to support itself, a process similar to neuron development in the cerebellum. The invading glioma cell can undergo substantial volume and shape change in order to disrupt the normal astrocyte-vascular

interface (end feet), to have a better position for nutrition and interfere with the normal neurophysiological function. Moreover, these cancer cells can produce proteases and metalloproteases to breakdown extracellular matrix which cause damage to normal brain tissue.

Hypoxic induced angiogenesis also plays an important role in GBM proliferation and invasion[165]. When tumours rapidly proliferate it results in high oxygen demand, and inadequate nutrient supply which can cause hypoxia at the tumour core. This can induce some of the cancer cells migrate from core to the margin, and also produce pro-angiogenic factors to induce angiogenesis. The new vasculature is rebuilt to restore the blood supply that facilitate cancer cells to migrate and further expand the tumour margin. With the very rapid growth seen in GBM the tumour can outstrip its blood supply leading to tumour necrosis – a common histological feature.

In summary, the nature of GBM cells and its invasion involve numerous complex regulations from the genetics, epigenetics mutation to extracellular matrix interference. In the early stage of the GBM invasion, although some cellular changes can be observed, only little can be seen in tissue level which is difficult to detect by using the MRI.

1.3 Treatment of the GBM

Standard treatment of the GBM includes maximal safe resection, followed by radiotherapy with concomitant and adjuvant temozolomide chemotherapy[140]. After the initial imaging diagnosis, surgical resection is the first choice for treatment and to obtain specimen for definite pathology diagnosis. Many studies had shown benefit of the extent of tumour resection on the outcome and further tried to maximize it[3,45,48,68,119]. In a large cohort study of 1229 GBM patients, they found that, the median survival time was significant longer in the patients with gross total resection than subtotal resection (15.2 versus 9.1 months, $p < 0.0001$)[73]. Furthermore, the resection of > 53.21% of the FLAIR abnormal area beyond the contrast enhancing lesion showed a significant longer median survival (20.7 versus 15.5 months, $p < 0.001$)[73]. Other studies also showed that a surgical resection 1- 2 cm beyond contrast enhancing lesion can lower the local recurrent rate from 87.5% to 67%.[23]

5-aminolevulinic acid (5-ALA) assisted surgery showed a better complete resection of the contrast enhanced tumour than using the light microscope only[135]. 5-ALA is a biochemical precursor of heme synthesis in mammalian cells. In normal cell, the 5-ALA was metabolized to the endogenous fluorescent protoporphyrin IX (PpIX) in the mitochondria, and the addition of Fe^{+2} by the action of ferrochelatase on PpIX generate the heme[144]. In GBM cell, studies found a down regulation of the ferrochelatase[145] and increase expression of the ATP-binding cassette transporter 6. Therefore, oral intake of high concentration exogenous 5-ALA can result in the accumulation of the PpIX. This produces visualization of violet-red fluorescence after excitation by the 405nm wavelength blue light. Therefore, this can be applied to differentiate normal cells from GBM cells by using a filtered fluorescent microscope during surgery. Although the negative predictive value of the 5-ALA fluorescence guided surgery varied from

22~91%, it has a fairly good positive predict value[43]. In a study of 13 GBM resections, the 5-ALA guided resection volume is larger than the contrast enhancing lesion (84cm^3 versus 39 cm^3) with a mean distance of 6 mm from contrast enhanced margin[122]. Stummer et al also showed a significant improvement of total resection with the aid of 5-ALA (60% vs. 36% without) and a higher 6-month PFS (41% vs. 21.1%)[135]. Further meta-anlysis showed that the gross total resection rate can be up to 75.4% (95% CI: 67.4–83.5, $p < 0.001$)[27].

For the post-surgical patients or those who are not surgical candidate, concomitant chemo- radiotherapy is an option. Stupp in 2005, showed that radiation plus concomitant temozolomide followed by six cycles of adjuvant temozolomide had a better median survival compared to radiation alone (14.6 months versus 12.1 months)[139], especially in patient with MGMT promoter methylation (median survival: 21.7 months versus 15.3 months)[47]. A longer follow-up of this European Organization for Research and Treatment of Cancer (EORTC)/ National Cancer Institute of Canada Clinical Trail Group (NCIC) showed the benefit of adjuvant temozolomide with radiation therapy can last throughout 5 years follow-up (5 year survival rate 9.8% versus 1.9%).[138]

The standard fractionated intensity modulated three-dimensional radiotherapy was given to patient with a total dose of 60 Gy in 30 daily fractions in every weekday in six weeks period. The gross target volume (GTV) was defined by T1-weighted MR with contrast. In EORTC, the clinical target volume (CTV) of 60 Gy was defined as extension of 2 cm from GTV, and planning target volume (PTV) was defined a further 0.5 cm extension from CTV. Other modes of radiation therapy have also been studied to improve the tumour control rate, for example using different imaging modalities re-delineate target volume. The RTOG defined GTV by using the post-operative

FLAIR/T2 abnormality. A comparison study showed that there was no difference in the recurrent pattern between two methods, however, the median volume percent of brain irradiated to high doses was significantly smaller in the EORTC method[80]. DTI defined high risk volume for radiotherapy also showed the reduction of 50% of the CTV[7] and 35% of the PTV[57].

Temozolomide is an oral alkylating chemotherapy that alkylates DNA (mostly at the N-7 or O-6 positions of guanine residues). Therefore, its clinical benefit can be largely affected by the methylation status of the MGMT promoter (also see section 1.2.2). The standard dosage was adjusted by patient body weight with 75mg per body surface area per day (75mg/m^2/day). After 28 days' break, patients received six cycles of adjuvant Temozolomide (150–200 mg/m^2) treatment for 5 days monthly.

Other chemotherapy agents have been developed against GBM, however, majority of them showed limited clinical benefit. Bevacizumab, a mono-clonal antibody against vascular endothelial growth factor (VEGF), failed to improve survival in newly diagnosed GBM.[35] Carmustine (an alkylating chemotherapy) wafer implantation during surgery into surgical resection tumour bed was designed to enhance local control rate due to the difficulty in identifying tumour invasive margin. In a phase three clinical trial, the use of carmustine wafer showed a modest benefit.[162] Patients with carmustine wafers implanted had the median survival of 13.9 months, which is longer than the control group (11.6 months). However, in another study of using carmustine wafer implantation for local chemotherapy control, the local failure rate was still 80% (33 out of 41 patients).[26]

There is only limited alternative treatment for GBM. Many treatments targeted growth factor pathway, angiogenic pathway, intracellular pathway or combination multi-

targeted kinase inhibitors have been shown limited therapeutic benefit[164]. And until now, although many efforts have been done in the immunotherapy, there is still no sustained clinical benefit in GBM. Tumour treatment field (Optune, Novocure) is a new FDA approved treatment for GBM. It is a non-invasive portable device using low intensity, intermediate frequency electric field to control tumour. In a phase 3 clinical trial compared with best physician chemotherapy in recurrent GBM patients, although there was no difference in overall survival, the efficacy of this tumour treatment field device was comparable with chemotherapy regime and with lower incidence of adverse effect and also provided a better quality of life for patients.[141] More recently, a phase 3 clinical trial (EF-14) testing the efficacy and safety of tumour treatment field showed that a longer median PFS (6.7 versus 4.0 months, p = 0.00005) and median overall survival (20.9 versus 16.0 months, p = 0.00006) were found in the tumour treatment field group[114].

1.4 MRI in the Diagnosis of Glioblastoma Invasive Margin

MRI, due to its high contrast between different soft tissues, is currently the standard of diagnosis before the pathology examination from the surgical resection or biopsy specimen. MRI can not only be used to make diagnosis, but also provides information about the location of the lesion for further treatment planning. Standard sequence for diagnosis including a T2 fluid-attenuated inversion recovery (FLAIR), pre-gadolinium T1, and post-gadolinium T1.[77] These sequence can be obtained with high-resolution or 3D volumetric sequences. The typical presentation of GBM by the conventional structure MRI is a large heterogeneous mass with central necrosis, hemorrhage, contrast enhancement and peritumoural oedema. However, there are several limitations of structure MRI which facilitate the emergence of numerous advanced MR techniques.

1.4.1 Structure MRI and Its Limitation

Studies had shown several limitations of the conventional MRI[112]. In a cohort of 160 GBM patient, the sensitivity, specificity, positive predict value and negative predict value using conventional structure MRI for the diagnosis of GBM are 72.5%, 65.0%, 86.1%, and 44.1% respectively[69]. Another study comparing structure MRI diagnosis and histopathology diagnosis, only 42.5% sensitivity and 95.6% specificity were noted in the high grade astrocytoma.[61]

T1 weighted with gadolinium contrast enhancement can show the breakdown of blood brain barrier and thought to be related with high grade tumours. Although contrast enhancing is the main finding in GBM, however, reports had shown that it is difficult to differentiate low grade and high grade glioma only from the enhancement[124]. In addition, it is difficult to differentiate GBM from other high grade tumour by contrast ring enhancement, and many lesions, such as abscess, also share this feature.

The hyperintensity in T2/FLAIR presents the vasogenic oedema in the peritumoural area. It is not only the exclusive feature of GBM, but also fail to represent the tumour infiltration. In a biopsy study, normal signal in conventional T1 and T2 MRI showed 16% and 4% of false negative rates respectively.[109] Besides, in the latest modification of the Response Assessment in Neuro-Oncology (RANO), T2/FLAIR for the assessment of tumour response has been removed due to its complex physiology meaning.[31] Therefore, the accurate assessment of treatment response in GBM cannot be achieved by using only structure MRI due to the lack of the biology information. Gruso et. al.in 2005 used methionine positron emission tomography for the radiation therapy target planning showed that the uptake of methionine area was different from both contrast enhancement and T2 weighted MRI in the postoperative GBM[40]. And the study concluded that the methionine PET can provide a more accurate gross target volume for radiation therapy.

Pseudo- progression and pseudo-response are also another two challenges in the assessment of treatment response in GBM. Pseudo-progression is a temporary contrast enhancement in about 20-30% of the patients after surgical resection and radiation therapy.[161] This is due to the disruption of the vascular permeability by surgery or radiation effect which cannot be easily differentiate by using T1 post contrast MR. The pseudo-progression happens mostly on within 3 months after radiation therapy, therefore a true progression within 3 months can be only defined by the progression mainly outside of the radiation field[161]. The pseudo-progression can be affected by the temozolomide, and the MGMT promoter methylation status which further complicated the treatment decision.[12] Pseudo-response on the other hand, showed marked decrease of the lesion enhancement after patient been treated with bevacizumab or other types of anti-angiogenic agents. Structural MRI is unable to

distinguish pseudo-progression and true progression, and these phenomena address the limitation of T1 contrast enhancement MRI in the tumour biology.

In addition, although we know conventional structure MRI cannot accurately identify the full extent of the disease, surgical and RT planning as well as clinical follow-up, are mostly base on T1 contrast enhanced MRI. This weakens the efficacy of the standard treatment, and inevitably results in the tumour recurrence, which often happens within two centimeters beyond the surgical margin[32]. In order to overcome these problems, numerous imaging methods are now being developed[154].

1.4.2 Diffusion MR

The diffusion weighted imaging is based on the measurement of the Brownian motion of the water molecule. When protons been excited by a homogenous magnetic field in MRI, protons can spin likes gyroscope with same precession rate and phase. The rate of precession is proportional to the magnetic field strength (Larmor equation). When a pulse gradient is applied, the protons may have different precession rates depend on the magnetic field (dephasing). However, if another gradient added in the same direction, same time duration but an opposite magnetic direction, the protons signal theoretically rephrase if there is no proton movement (diffusion restriction). Therefore, if the protons move during the two gradient pulses, the protons may remain diphased at the end of the dephasing- rephrasing and subsequently lead to signal loss. In summary, the diffusion imaging, usually gradient-echo planar imaging, image is acquired by sensitizing the motion of protons. The difference in diffusivity (figure 1.2)[85] can be used to differentiate the different types of oedema, cellularity, and even the degree of malignancy.[63]

The amount of the diffusion signal loss by gradient application follows the equation:

$$\frac{S}{S_0} = \mathrm{e}^{-\gamma^2 G^2 \delta^2 \left(\Delta - \frac{\delta}{3}\right) \mathrm{D}} = e^{-bD}$$

S is the signal with the gradient application and S_0 is without gradient. D is the diffusion constant. Therefore, higher water diffusion rate (Diffusion constant, D) leads to lower diffusion weighted imaging (DWI) signal. The b-value represents how much gradient is applied and is dependent on the nuclear gyromagnetic ratio (γ), magnetic field strength (G), duration (δ) and the time interval between gradient (Δ).[84] However, the DWI signal can be affected by both b-value and T2-weighted effect. Therefore, calculation of the diffusion constant (D) in each voxel can create the apparent diffusion coefficiency (ADC) which is used to represent the quantitative measurement of the speed of diffusion (mm^2/sec). It not only reflects the true diffusion, but also depends on spatial orientation, bulk tissue motion, and pulse sequence timing.

$$\text{ADC} = D$$

For example, within the ventricle the water molecule diffusion is assumed to be unrestricted, due to the Brownian law this is called isotropic diffusion, and this may cause a large signal loss in DWI and a high ADC (3200 x $10^{-6} mm^2/s$). ADC will also increase in the situation of vasogenic oedema, where extracellular fluid increase results in the increase of water diffusion. On the contrary, if in circumstance of extracellular water restricted due to local pathology, there will be high DWI and a reduction in ADC. A reduction in ADC had been shown to be related with increase cellularity in glioma[143], CNS lymphoma or medulloblastoma[117]. The value of ADC has also be shown to be associated with the grading of glioma, a lower ADC can be seen in higher grade glioma resulting in a worse prognosis.[49] Howver, when using ADC to assess the whole GBM lesion, the mean value can be confusing, due to the

intraturmoral heterogeneity which combines necrosis, oedema and hypercellularity.
In addition, ADC can also be used as a prognostic factor in treatment of GBM. Studies using pre-treatment ADC histogram analysis showed that patients with mean lower Gaussian curve have longer survival (both OS and PFS) when treated recurrent GBM with bevacizumab[30]. The changes of ADC after treatment can be correlate to clinical outcome. A study showed that any changes (increase or decrease) after treatment can correlate with poor outcome[96]. Another study showed that a detectable decrease in ADC can predict the development of contrast enhancing lesion[41].

In an actual brain, the diffusion is not always isotropic; instead there is a tendency of diffusion along the axon, which is anisotropic diffusion (figure 1.2). Therefore, diffusion tensor imaging (DTI) is based on calculating the tensor of the diffusion and provide more information about direction (eigenvector) and magnitude (eigenvalue, λ) of the anisotropic diffusion. Different calculations had been used in the DTI. The mean diffusivity (MD) is for the isotropic diffusion, whereas fractional anisotropic (FA) is often reported as a relative measurement of the anisotropic diffusion (figure 1.3)[106].

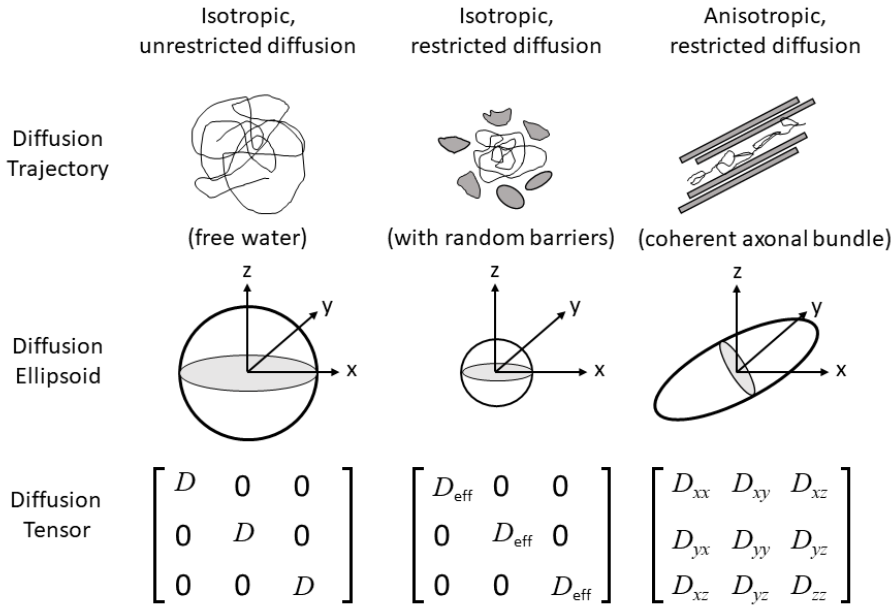

Figure 1.2

Illustration of difference diffusivity in unrestricted isotropic diffusion isotropic restricted diffusion and anisotropic restricted diffusion.

(adapted from Diffusion tensor MR imaging and fiber tractography: theoretic underpinnings. AJNR American journal of neuroradiology 2008;29:632-41)

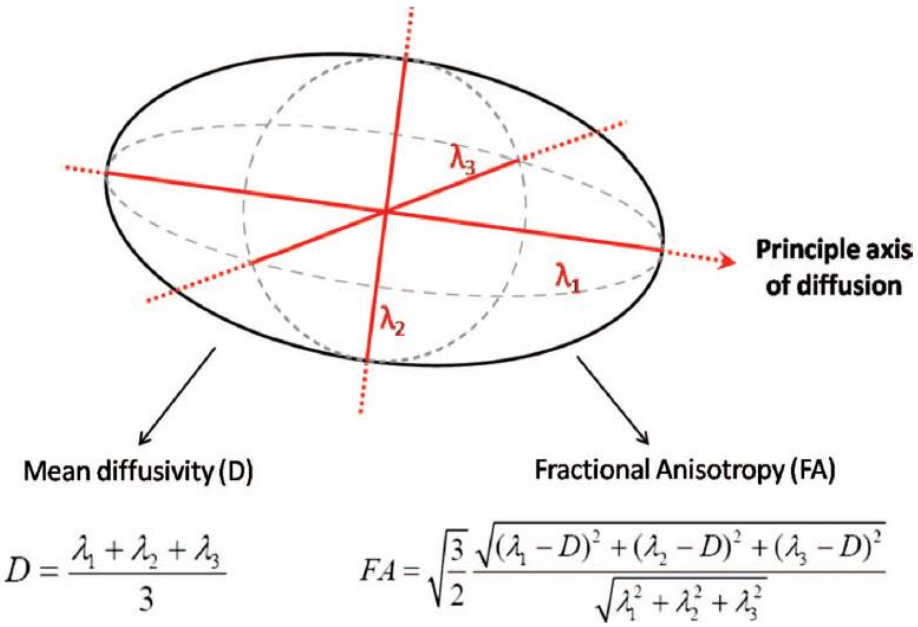

Figure 1.3

Tensor calculation of diffusivity into mean diffusivity and fractional anisotropy.

(The role of advanced MR imaging in understanding brain pathology. British journal of neurosurgery 2007;21:562-75)

A biopsy studied had shown that FA in the peritumoural area is negatively correlate with the degree of glioma infiltration.[24] And a lower FA, compared with normal appearing white matter (NAWM), can be seen in the peritumoural area of the glioma or metastatic tumour, but the FA value showed no difference between high grade glioma and metastatic brain tumour.[75,76] A decrease in relative anisotropic index (defined as below) can also be used to detect subtle white matter change caused by the malignant tumour infiltration.[108]

$$\mathrm{RAI} = \sqrt{\frac{1}{3}}\frac{\sqrt{(\lambda_1 - D)^2 + (\lambda_2 - D)^2 + (\lambda_3 - D)^2}}{D}$$

Pêna et al have conducted a series of studies of DTI imaging processing. Further dissecting of the diffusion tensor into isotropic component (p) and anisotropic component (q) gives us more information.

$p = MD \times 1.732$

$q = \sqrt{(\lambda_1 - D)^2 + (\lambda_2 - D)^2 + (\lambda_3 - D)^2}$

P is another representative form of the MD, and q can show the absolute directionality of tensor. Studies have shown that q, but not FA, is lower in the GBM peritumoural area than in the metastatic peritumoural area which may due to tumour infiltration.[156] By calculating the p q map, the DTI can differentiate when the white matter is displaced, infiltrated or disrupted by the glioma cell[111]. In addition to the change in white matter, the utility of the p q map can be an indicator of infiltration, even in the area shown to be normal by conventional MRI. A biopsy study showed that an 10% increase in p and 12% decrease in q can detect the possible tumour infiltration margin with a sensitivity of 98% and a specificity of 81%.[105] Moreover, by classifying the p q map into diffused (p > q), localized (p > q in a certain direction) and minimal (p = q) infiltrated patterns,

this can predict site of progression and show substantial differences in patient prognosis.[83] And among these three groups the diffused type carried the worst 18-month progress-free survival. In a more recent study showed that in all patients with *IDH*-mutant GBM had the minimal infiltrated DTI phenotype, while only 8% in the *IDH*-wild GBM patients.[107]

DTI can also be used for radiotherapy planning. Studies had shown that by using DTI defined margin, a 50% reduction in the clinical target volume (CTV)[7] and a 35% of reduction planning-target volume (PTV)[57] can be achieved to cover the site of tumour recurrence. This may minimize unnecessary radiation. Therefore, the GBM imaging shown by the DTI can provide more information than the conventional MRI.

The DWI and DTI are based on the hypothesis that water molecules diffuse equally in all direction and were calculated according to the Gaussian distribution. However, the complexity of the microstructure in real brain causes the diffusion of water molecule in a more variant distribution pattern. Therefore, diffusion kurtosis imaging (DKI) has been development to evaluate a more accurate diffusion of water molecule in a non-Gaussian way[133]. The kurtosis describes the deviation of the peak of probability distribution from the Gaussian pattern. Three parameters are widely used. The mean kurtosis refers to the average of the diffusion kurtosis along all directions; the axial kurtosis which is the diffusion kurtosis along axial direction; and the radial kurtosis. The applications of the diffusion kurtosis imaging have been used in various of clinical situations including stroke, degenerative disease, traumatic brain injury, fibre tracking and brain tumour. Van Cauter et al. showed a better discrimination of low and high grade glioma by using the diffusion kurtosis imaging than the conventional DWI[150].

1.4.3 Dynamic Susceptibility Contrast MRI (DSC-MRI)

Neovascularization is one of the features of GBM histology, this may cause change of regional cerebral perfusion and vascular permeability. Perfusion MR technique, including T2* weighted DSC-MRI, T1 weighted dynamic contrast-enhanced (DCE), and arterial spin label MR, were used for the GBM.

DCS-MRI, relies on the T2* signal drop caused by the passage of a gadolinium-containing contrast agent through the tissues. The drop in signal is proportional to the concentration of the contrast agent and the tissue vascularity. Therefore, we can further get the volume of blood in the voxel over the mass of tissue within the voxel by calculating the area under relaxavity curve, and this ratio is called relative cerebral blood volume (rCBV). However, due to the abnormal vascular permeability in GBM that cause contrast leakage, further computational correction[11], such as perfusion post-processing package in NordicICE (Nordic NeuroLabs, Bergan, Germany). By using this method, we can know the histologic grading before the operation. Hakyemez et al in a study of 33 glioma patients showed that higher rCBV in high grade glioma (6.50±4.29 versus1.16±0.38, $p < 0.001$) with the cut-off value of 1.98. Price, et al also showed that the rCBV is proportional to the mitotic rate (MIB-1 index) [110]. A higher MIB-1 index, which means a more malignant, may show higher rCBV. Besides, increase rCBV can be seen in the invasive margin, this can be seen in the study of DTI-defined invasive peritumoural area.[113] In addition, studies also show that the changes in rCBV can detect the malignant transformation of the low grade glioma into high grade glioma one year earlier than the conventional contrast MRI study.

Although DCE-MRI and arterial spin label MRI were not used in this thesis study, both are important emerging technique in the study of GBM. DCE-MRI can calculate K^{trans} which reflects the efflux rate of gadolinium contrast from blood plasma into the tissue.

It is affected by the microvascular permeability, vascular surface area, and blood flow. DCE-MRI can also be used to differentiate low grade and high grade glioma.[72] DCE-MRI can also help to show pseudoprogression of GBM after treatment. A retrospective study showed that in regions of pseudoprogression, there are significant lower plasma volume and K^{trans}.[146] Although this is less commonly used than DSC-MRI, DCE-MRI can provide a better spatial resolution and lower magnetic susceptibility artifact.[17] Arterial spin label MR is a non-contrast technique, that use endogenous magnetic labeled due to the blood flowing into brain. Although it is less frequently studied, arterial spin label MR can provide quantitative value of cerebral blood volume and the information of tumour angiogenesis which is also comparable to DSC-MRI.[158]

1.4.4 Magnetic Resonance Spectroscopy

MRS is a way to understand local metabolism from the information of chemical molecule/ metabolites. The detection of the metabolites is based on the chemical shift, which refer to the difference in resonance frequencies of two nuclei in different molecular environments. Therefore, for example, proton may have different resonance frequency in water and fat. In MRS the frequency change cannot be used for spatial encoding, it further transforms the signal into the frequency spectrum. Specific molecular compounds can be detected and quantified by measuring their resonance frequencies in a certain region in the tissue[63]. There are different types of MRS and the most common is proton MRS (^{1}H MRS). Because the proton is abundant in water and fat that may overwhelm the signal of other metabolite, therefore water suppression technique should be applied and also avoid voxel selection of the fat in bone marrow or scalp.

In the ^{1}H MRS, the most important indicator is the Choline (Cho)/ N-acetyl aspartate (NAA) index. The choline represents the turnover rate of the cell and the NAA is usually an indicator of the normal neuron. Therefore, in the region with active cancer cells there is always a high Cho/ NAA ratio. And this can be used to delineate tumour margin which is different from structure MRI. Pirzkall et. al in 2001 used the Cho/NAA defined target volume for radiation therapy and showed that the metabolically active tumour can extent outside of T2 hyperintensity up to 28 mm in 88% of cases[102].

The MRS also contributes to the assessment of treatment response in glioblastoma, such as the differential diagnosis of the pseudo- progression and true progression. In a systemic review compared the diagnostic accuracy for treatment response between different MR techniques showed that the MRS has the highest diagnostic accuracy (sensitivity: 91%, specificity: 95%)[152]. Besides, studies have shown that distinct differences exist in the peritumoural ^{1}H-MRS characteristics that can differentiate GBM from the non-invasive meningioma.[163]

Furthermore, MRS can also be used to detect 2-HG, which is a product from alpha-ketoglutarate in *IDH1*-mutant GBM[20]. However, the detection of the 2-HG is difficult by using the standard MRS, its spectrum occurs between 2.4-2.6 ppm that overlaps with glutamine and glutamate peaks[104]. Other types of MRS also provide valuable information, ^{13}C MRS is a good tool for enzyme kinetic study, and ^{31}P MRS for phsophorylated target detection.

1.4.5 Multimodal MRI and Radiomics

With the developing of different advanced MR techniques, both structural and the physiological information can be studied now (Table 1)[10,154]. Numerous studies had used the combination of different MR techniques to study the intra-tumoural

heterogeneity, tumour invasive margin, clinical prognosis, response to treatment, and diagnosis of pseudo-progression/ response.

Two examples of GBM cases were shown here to demonstrate the heterogeneous presentations in different MR techniques (Figure 1.4). In these two cases, we compared T1 weighted with contrast MR, DTI-q, DTI-q and MRS on the same level. It is clear that, by using different MR techniques, the regions of abnormality are different. The contrast enhanced lesions are usually smaller than other MR sequences, this indicates the inadequate accuracy of T1 post-contrast MR to outline the GBM. Besides, on the MRS figures, where the heat map indicated the Cho/NAA ratio, showed that the uneven tumoural activity around the peritumoural area, whereas no difference in the structural MR.

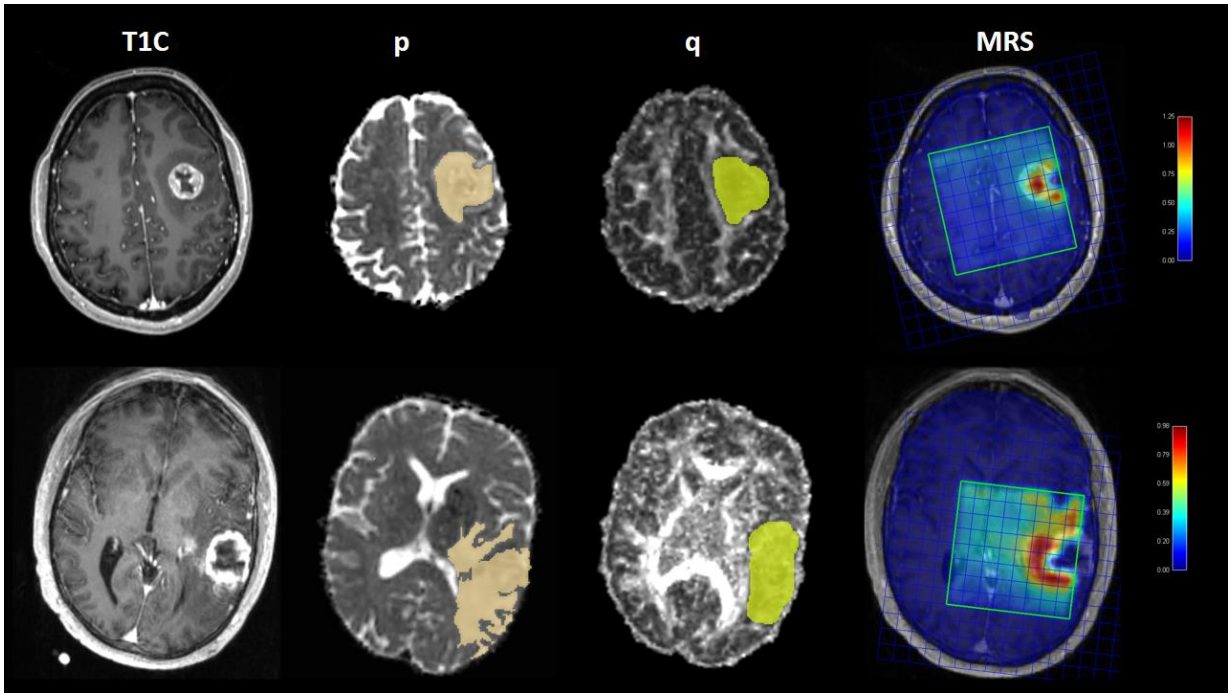

Figure 1.4

Two representative GBM cases shown in T1 post contrast MR, DTI-p, DTI-q and MRS. The creamed-color defined the abnormal DTI-q areas, the yellow color showed the abnormal DTI-q areas. The heat map on MRS showed the level of Cho/NAA ratio.

Table 1 Summary of Different MR Techniques

	Advantage and biomarkers	**Limitation**
Post contrast T1-weighted	Can provide good spatial resolution by using 3D volumetric technique.	The contrast enhancement is non-specific which represents disruption of BBB, rather than the tumour cell.
T2/ FLAIR	Able to detect tissue water content/ oedematous changes.	Lack biology specificity, which unable to distinguish tumour infiltration oedema and other types of oedema.
DWI (ADC)	Can quantify the diffusivity. An increase can be seen in cystic lesions, oedema, low cellularity, and necrosis. Decrease indicates cytotoxic oedema, and higher cellularity.	Unable to differentiate tumour cell from other inflammatory cells. Mixture of the oedema and increase cellularity may complicate the interpretation.
DTI	Can detect subtle white mater change, cause by tumour infiltration, displacement or disruption. Can be used as a surrogate for the GBM invasive margin.	Lack detail information for the local biology microenvironment.
DSC-MRI	Provide regional rCBV, relative cerebral blood volume which represent vascularity.	Analysis is operator dependent and calculation need to be corrected due to the damaged BBB in GBM.
DCE-MRI	Show vascular permeability (contrast transfer coefficient, K^{trans}), rCBV, rCBF Good spatial resolution.	Analysis is model dependent, and based on either flow-limited or permeability-limited conditions.
ALS	Quantify cerebral blood volume without contrast.	Less applicable
MRS	Can provide metabolic changes in microenvironment. Ex. Cho (membrane turnover), NAA (normal neuron marker), lactate (anaerobic metabolite)	The spectra resolution is time dependent, thus provide limited spatial accuracy. Susceptibility artefact due to blood or metallic implants

Since each MR techniques had its advantages and limitations. Radiomics can provide a more detailed quantification multi-modal MR study. The suffix –*omic*, originally refers to detailed characteristics of biology molecule. Radiomics is defined as the conversion of images to higher dimensional data and the subsequent mining of these data.[37] This can be performed in computed tomography (CT), MRI or positron emission tomography (PET). The regions of interest (ROIs) can be a whole tumour or a subdivision of the tumour (habitat). The main difference the radiomics is the extraction of numerous quantitative images features. In the conventional imaging analysis, few quantified features (semantics features) can be extracted, such as location, vascularity, and size. And most semantics features, such as shape, can only undergoes qualitative analysis. By using high-throughput computing, radiomics can quantify more detailed agnostic features including first order, second order or higher order. First order features are the histogram analysis of the value in each voxel. This include mean, median, standard deviation, minimum, maximum, variance, kurtosis, skewness, entropy, energy, uniformity and root mean square. Second order features are the texture analysis that take the neighbour voxel into consideration. The second order texture analysis was firstly introduced by Haralick in 1973 by using the grey-tone spatial-dependence probability-distribution matrices to generate 14 different texture features[44]. Such features can provide information about images homogeneity, contrast, linear structure, and complexity. Grey-level co-occurrence matrix (GLCM) is a statistics based texture analysis, based on how often a pixel of intensity i finds itself within a certain relationship to another pixel of intensity j[22]. The GLCM texture analysis mainly provides energy, homogeneity, dissimilarity, and correlation. Another commonly used texture analysis is the run-length matrix (RLM) which calculates the run-length of the matrix from different directions. In an image with fine texture, more short runs with similar gray-level intensity can be found, whereas a course image has more long runs.

(more detailed explanations are shown in Chapter 7 section 7.2.3).

Higher order analysis includes filter grid or wavelet analysis for the images. The application of the filters (such as Laplacian of Gaussian bandpass) can extract specific imaging strutures depending on the width of the filter. Other higher order texture analysis, such as model-based and transform-based methods were also used to maximise the imaging features[131].

The methodology of the radiomics is still under development, and there has not been a standard protocol for these radiomics process. Still, numerous studies have recently been published to investigate different kind of tumours. In 2014, Aerts used 440 radiomics features of lung cancer from CT scan and showed different tumour phenotype with clinical prognosis correlation.[1] Gevaert et at, in 2014 published a work in GBM.[34] They showed the radiomics features can correlate with manual radiologist's Visually Accessible Rembrandt Images features, and patient clinical survival. Moreover, 7 of these features can also correlate with gene expression. Another study used quantified radiomics data from 121 GBM patients to cluster 3 distinct MR phenotypes, the peri-mulifocal, spherical and rim-enhanced.[54] They found each cluster had its different pathway which possibly explain the distinct prognosis. Radiomics can also be used to help clinical decision making. Hu et al, in 2015 used multi-parametric MRI and texture analysis to predict tumour density in both enhanced and non-enhanced part based on a biopsy study and showed 85% accuracy in training set and 81.8% accuracy in the validation.[52] Therefore, by using multimodal MRI with radiomics can provide a non-invasive way to understand GBM more and provide further support in clinical decision.

1.5 The Peritumoural Zone and Its Clinical Manifestation

The peritumoural zone is an extension area from the primary tumour site which is usually identified by T1 post contrast MRI. There is no clear definition of this zone, however, it is important. As most surgical resection or biopsy is based on the T1 contrast enhanced MRI, the peritumoural zone harbors the tumour invasive margin that is left after surgery. Although standard post-operation radiotherapy covers an additional 2-3 cm of the margin, there is still high local recurrent rate, this may due to these peritumoural GBM cells frequently have an invasive phenotype that are not in the cell cycle, and can be spared from the DNA damaging treatment. However, there is still limited understanding of the nature of GBM infiltration outside of contrast enhanced lesion.

From the biology point of view, it is without doubt that the GBM cancer cell can extend beyond contrast enhancing area into these peritumoural zone. In one of the studies, researchers showed that cancer cell can be detected in 1/3 of the peritumoural zone where are contrast nonenhancing and visually normal under operative microscope.[70] They also showed a difference of the peritumoural zone from both contrast enhancing lesion and normal brain tissue in the proteomics and transcriptomics study. Similar result from Aubrey et al, showed at least 10% infiltrative cancer cell in 5 out of 10 peritumoural zone biopsy.[5] Another MR-guided biopsy study comparing the contrast enhancing and nonenhancing regions of the GBM showed that there are different molecular and cell types by using RNA-sequencing and histology analysis.[36] In their study, the nonenhancing parts showed more neural type, and the contrast enhancing part predominant with proneural, mesenchymal and classic type of GBM. However, the biology characteristics of this peritumoural zone still not fully understood due to GBM spatial and temporal heterogeneity. The other possible reason is the sites of biopsy were roughly decided on structure MRI.

The common radiology definition of the peritumoural zone is hyper-intensity in FLAIR without contrast enhancement. An imaging study focus on this FLAIR defined non-enhancing regions of GBM showed that, the increase of rCBV in these areas marked correlates with worse clinical outcome, both OS and progression free survival (PFS) (p = 0.0103, p = 0.0233).[56] And they also found that worse prognosis in those patients with non-enhancing regions crossing the midline of the brain. However, the abnormal FLAIR signal in GBM is largely affected by the vasogenic oedema. Many of the emerging advanced MR techniques and imaging processing methods are now accessible. Therefore, many studies had used different MR techniques to identify the imaging biomarkers in this peritumoural zone. As previous mentioned, DTI can showed distinct characteristics in GBM peritumoural zone from metastatic tumours or meningioma.[76,156] MRS studies also showed a higher Cho/NAA ratio in the peritumoural zone of the GBM than metastatic tumours/ meningioma or normal brain tissue.[163] Still, a concise imaging definition of the invasive margin in the peritumoural zone is not identified.

Furthermore, these peritumoural zones usually left behind surgical resection not only be the potential site of tumour progression/ recurrence, but also correlate with patients' prognosis. As previously mentioned in section 1.3, the extent of resection may largely affect the clinical outcome. Surgical resection guided with fluorescence 5-ALA, can maximize the extent of resection that provides longer time to progression in GBM patient.[27,135] Besides, studies had shown that the residual contrast enhancing lesion can largely affect both OS and PFS.[65] Grabowski et al further showed not only residual contrast enhanced lesion but also the residual FLAIR were significant predictors of survival after controlling for age and performance score[39].

In summary, the peritumoural zone has cancer activity, although is complexity of its biology is not fully understood, the clinical benefit can be achieved after the extended resection. However, the imaging biomarkers to identify a more defined invasive area in the peritumoural zone need to be further studied.

1.6 Summary and Conclusion of Literature Review

GBM is the most common and malignant primary brain tumour arise from astrocyte/ neural progenitor cell. It can be classified into IDH-mutant and IDH-wild type which represents different pathogenesis and also different clinical presentation. However, the prognosis is still dismal even after multi-disciplinary treatment.

Current imaging diagnosis and treatment planning rely on the T1 contrast MRI. The lack of biology specificity of this conventional structure MRI compromises the treatment effect. The peritumoural zone where tumour cells can infiltrate are left in situ after surgery due to lack of the contrast enhancement. This results in the high local recurrence/ progression rate even after radiotherapy and chemotherapy. Besides, oncology researchers may focus on the resected specimen which is thought to be the majority of the tumour mass, and study of the tumour activity in the peritumoural zone is previously underestimated. Currently, our understanding of the GBM heterogeneity is not only intra-tumoural but also peritumoural. Molecular biology study showed different genetic expressions in the core, the margin and the peripheral area of the tumour. This can be explained by its complex spatial and temporal evolution.

Although more and more studies had shown the important in this peritumoural zone, not all the peritumoural zone (usually defined by FLAIR) is the tumour invasion margin, and the identification of this invasive margin remained unsolved. The development of different MRI techniques (DWI, DTI, perfusion MRI, MRS…) provide more information in cancer physiology behavior rather than simply anatomical location. This attempts give us a hint to find the invasive margin outside of contrast enhancement. In addition to different MR techniques, data processing including the utilization of radiomics and machine learning provide us a new direction to search.

Therefore, in order to identify the GBM invasive margin and to better understand its invasiveness, multimodal MRI with advanced data management is needed.

CHAPTER 2

Hypothesis

The aims of this thesis are to understand the imaging characteristics of the peritumoural zone where GBM recurs or progresses after surgical resection by using current multimodal MR techniques and further generates a model to identify/ predict the tumour invasive margin prior to surgery.

Hypothesis Tested

1. A more accurate image co-registration in brain tumour MRI between different time points can be achieved by using a two stage semi-automatic non-linear co-registration method to overcome the massive regional distortion caused by surgery or tumour progression. The first stage is to calculate the transformation between resected lesion and resected cavity, then secondly apply to the brain parenchyma. (Chapter 4)

2. A larger extent of resection, based on the DTI-defined invasive regions, can result in a better prognosis. Use the above method to coregister the post-operative MRI to the pre-operative MRI can conduct an accurate volumetric study to test the clinical effect of the extent of resection based on different MRI sequences. (Chapter 5)

3. The peritumoural abnormal DTI-q defined invasive area using MRS and perfusion MRI can have imaging characteristics similar to the main tumour bulk, such as higher Cho/NAA ratio and increase regional perfusion. (Chapter 6)

4. Different phenotypes of the peritumoural DTI-q defined invasive margin can be an independent factor correlates with patient prognosis. (Chapter 6)

5. The two stages non-linear semi-automatic coregistration method to coregister MRI at tumour recurrence/ progression to the pre-operative MRI can identify the regions where eventually recur/ progress. And these peritumoural area that potentially recur/ progress can have distinct imaging characteristics comparing to other normal peritumoural area by using multimodal MRI and radiomics approach. (Chapter 7)

6. The imaging characteristics obtained from the abovementioned can be used to establish a prediction model to identify the possibility of tumour progression in the peritumoural zone of the pre-operative MRI by using the machine learning model (convolutional neural network). (Chapter 7)

CHAPTER 3

GENERAL METHODS

3.1 Patient Population

3.1.1 Inclusion and Exclusion Criteria

Patients diagnosed with supratentorial GBM since 2010 were collected prospectively from a NIHR funded “Magnetic Resonance Imaging to Characterise Invasive Phenotypes in Cerebral Gliomas” study (ISRCTN62033854). All patients were identified and discussed at the neuro-oncology multidisciplinary team meeting. An informed written consent was obtained from every patient and this project was approved by the local Institutional Review Board (ethics reference no. 10/H0308/23). Eligible patients include those aged over 18 years old, with a Karnofsky performance score (KPS) of more than 70, and final pathology reported as GBM with or without mixed type. Standard treatment protocol of the GBM patient was described as below for all inclusion participants. Besides, all patients included in this study were suitable for maximal resection (>90%) which is evaluated by the operating surgeon before operation. Exclusion criteria were previous cranial surgery, previous cerebral radiotherapy or a known other primary tumour. In addition, patients not able to receive MRI examination, such as claustrophobia or non-MRI compatible implants, were also excluded from the study.

3.1.2 Patient Treatment

All patients received a standard neurosurgical operation including resection followed by focal concomitant chemoradiotherapy (CCRT) and adjuvant chemotherapy treatment regimen[138]. Surgical resection was performed with the principle of maximal safe resection with fluorescence 5-ALA guidance under the assistance of neuronavigation. Standard CCRT was started as soon as possible after stabilization of the patient's post-surgical condition, usually one month after the operation. Concomitant Temozolomide treatment was prescribed during radiotherapy, and was adjusted by patient body weight with 75mg per body surface area per day (75mg/m^2/day). After 28 days' break, patients received six cycles of adjuvant Temozolomide (150–200 mg/m^2) treatment for 5 days monthly.

3.1.3 Patient Characteristics and Outcome Measurement

Relevant patients' characteristics were listed in the APPENDIX A.

Extent of resection (EOR) is categorized into gross total resection (GTR) or complete resection of the enhancing lesion and subtotal resection (STR). Pre-operative tumour volume was defined by T1-weighted contrast MRI with manually segmentation (please refer to section 3.2.8). Tumour location was categorized into non-eloquent, near eloquent and eloquent area according to Sawaya classification.[120] *IDH-1* mutation status was conducted through immunochemistry test for the R132H mutation.

Progression free survival was defined from the operation date to time of progression based on the modified RANO criteria[31]. In brief, a progression disease is defined as a ≥25% increase in sum of products of perpendicular diameters or ≥40% increase in total volume of enhancing lesions in at least two sequential scans separated by at ≥4 weeks. Overall survival was defined from the operation date to time of death or last follow up for non-censored patients.

3.2 MRI Acquisition and Image Processing

3.2.1 MRI Study Time Point

All patients received a standard diagnostic MRI study including 3 dimensional volumetric T1 weight with contrast enhancement (magnetization-prepared rapid gradient-echo, MPRAGE), T1 weighted without contrast, T2 weighted, FLAIR, DTI, DWI, MRS and DSC-MRI within one week before surgical intervention. All other following MRI studies include non-volumetric T1 weight with contrast enhancement, T2 weighted, FLAIR and DWI.

After the surgical resection, an immediate post-surgical MRI was done within 72 hours after operation. The time point of series MRI studies were done as in figure 3.1. Approximately one month after the operation, for those patients suitable to receive CCRT, an additional MRI was done for radiotherapy planning. After the CCRT, a post-RT MRI was obtained for treatment response evaluation. Follow up MRI studies were then planned every three months after treatment, with some modification according to patients' condition or clinical needs.

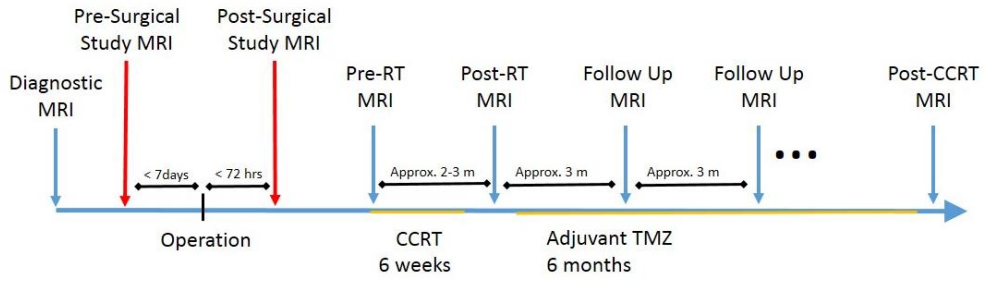

Figure 3.1

Scheme of patient treatment and MRI studies time points. Note that the pre-surgical and post-surgical MRI studies were obtained strictly within 7 days before operation and 72 hours after operation. Time points for pre-Radiotherapy (RT), post-RT, post-CCRT and follow up MRI studies may be varied according to patients' condition and clinical needs.

3.2.2 MRI Acquisition and Parameters

All pre-surgical MRI studies were performed with a 3.0 Tesla Siemens Magnetron MRI system (Siemens Healthcare, Munich, Germany) with a standard 12-channel head coil. Detailed parameters for each MRI sequence are listed in table 2.

Table 3.1

SIEMENS 3.0 Tesla MRI 12-channel standard coil							
	T1C	PWI	T1	T2	T2F	DTI	MRS
Sequence	GR\IR	EP	SE	SE	SE\IR	EP	csi_se
TR(ms)	2300	1500	50	4840	7840	8300	2000
TE(ms)	2.98	30	8.6	114	95	98	30
Thickness (mm)	1	5	4	5	4	2	20
FOV	256x240	192x192	240x192	220x165	250x200	192x192	160x160
Voxel size (mm)	1	2x2x2	0.75x0.75x4	0.6875x0.6875x5	0.78125x0.78125x4	2x2x2	10x10x20
Number of Slices	192	19	27	23	27	63	
Flip angle	9	90	90	150	150	90	90
Contrast	GADOVIST*						
FOV= field of view; GR= Gradient echo; IR = Inverse recovery; SE= spin echo; EP= echo planner; CSI=chemical shift image; MRS acquired matrix size (mm) = 16 x 16; *GADOVIST 9ml given during the DSCI at rate of 5ml/sec via a power injector.							

Post-surgical, pre-RT, post-RT, post CCRT and other follow-up MRI studies were acquired on a 1.5 Tesla GE Optima, 1.5 or 3.0 Tesla GE Signa (General Electric Company, Little Chalfont, United Kingdom) or 1.5 Tesla Siemens Avanto (Siemens Healthcare, Munich, Germany) with standard head coil. Parameters and settings were varied in these MRI studies. Sequences include a 2D T1-weighted sequence (TR/TE 440-771/8-21 ms, flip angle 58-90°, FOV 220-240 x 207-240 mm; 20-85 slices; 0-1 mm slice gap; voxel size 0.429-0.7188 x 0.429-0.7188 x 3-6 mm), a 2D T1 inversion recovery sequence (TR/TE 2508-2600/12-42 ms, inversion time 780-920 ms; flip angle

90-110°, FOV 220 × 220 mm; 20-22 slices; 1-3.5 mm slice gap; voxel size of 0.4297 x 0.4297 x 6 mm) or a 3D T1 fat suppressed sequence (TR/TE 7/2.948 ms, inversion time 900 ms; flip angle 190°, FOV 256 × 256 mm; 190 slices; no slice gap; voxel size 1 x 1 x 1 mm). T2, T2F and diffusion weighted images were also performed in most of the cases.

3.2.3 Pre-processing and Imaging Management

General diagnostic MRI data retrieve and general imaging processing pipelines are shown in figure 3.2.

Data retrieve (Figure 3.2 blue section)

After the scanning of the diagnostic MRI, raw images data in the format of Digital Imaging and Communications in Medicine (DICOM) were stored in the WBIC server. These DICOM files were downloaded anonymous and transformed into Neuroimaging Informatics Technology Initiative (nifti) files. The use of nifti file not only compatible in most of the imaging processing software, but also facilitate the data transferring, sorting and processing. The download and sorting were proceeded by using an in-house built function created by a senior member of the lab, Dr. Timothy J Larkin.

Pre-Processing (Figure 3.2 grey section)

Position and orientation of the images

Because MRI studies setting may be slightly modified from time to time during the cohort, it is important to correct all MRI studies into the same orientation and use the same anatomy target (anterior commissure) as the central point of image volume. This

step is mandatory before not only DTI processing but all other imaging processing. Therefore, all images were put into radiologic space with a Wolfson Brain Imaging Center (WBIC) inbuilt function "nii_to_radio". And the setting of anterior commissure as central point (0 0 0 in x y z coordinates) of all images volume by using the Statistical Parametric Mapping (SPM) software package in Matlab (The MathWorks, Inc.).

Brain Extraction

Before individual imaging analysis or imaging coregistration, brain extraction by using FMRIB Software Library (FSL) function ("bet") was automatically followed by manual correction.[128]

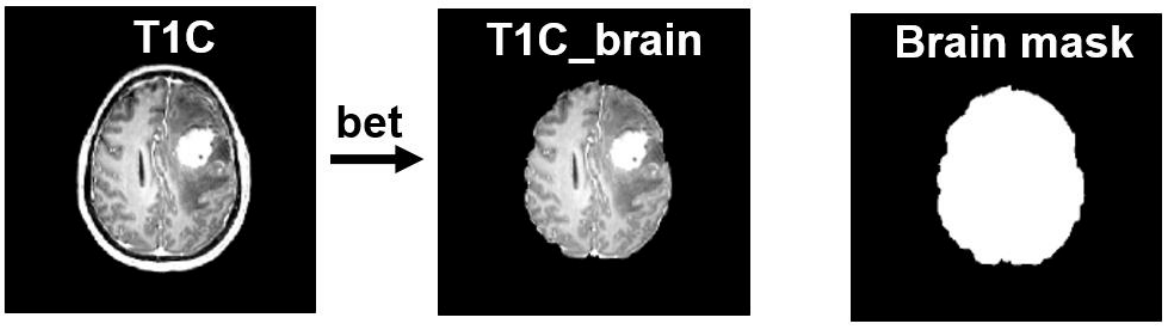

Imaging Processing (Figure 3.2 green section)

Individual imaging processing will be addressed in the following sections (section **3.2.4**, **3.2.5**, and **3.2.6**).

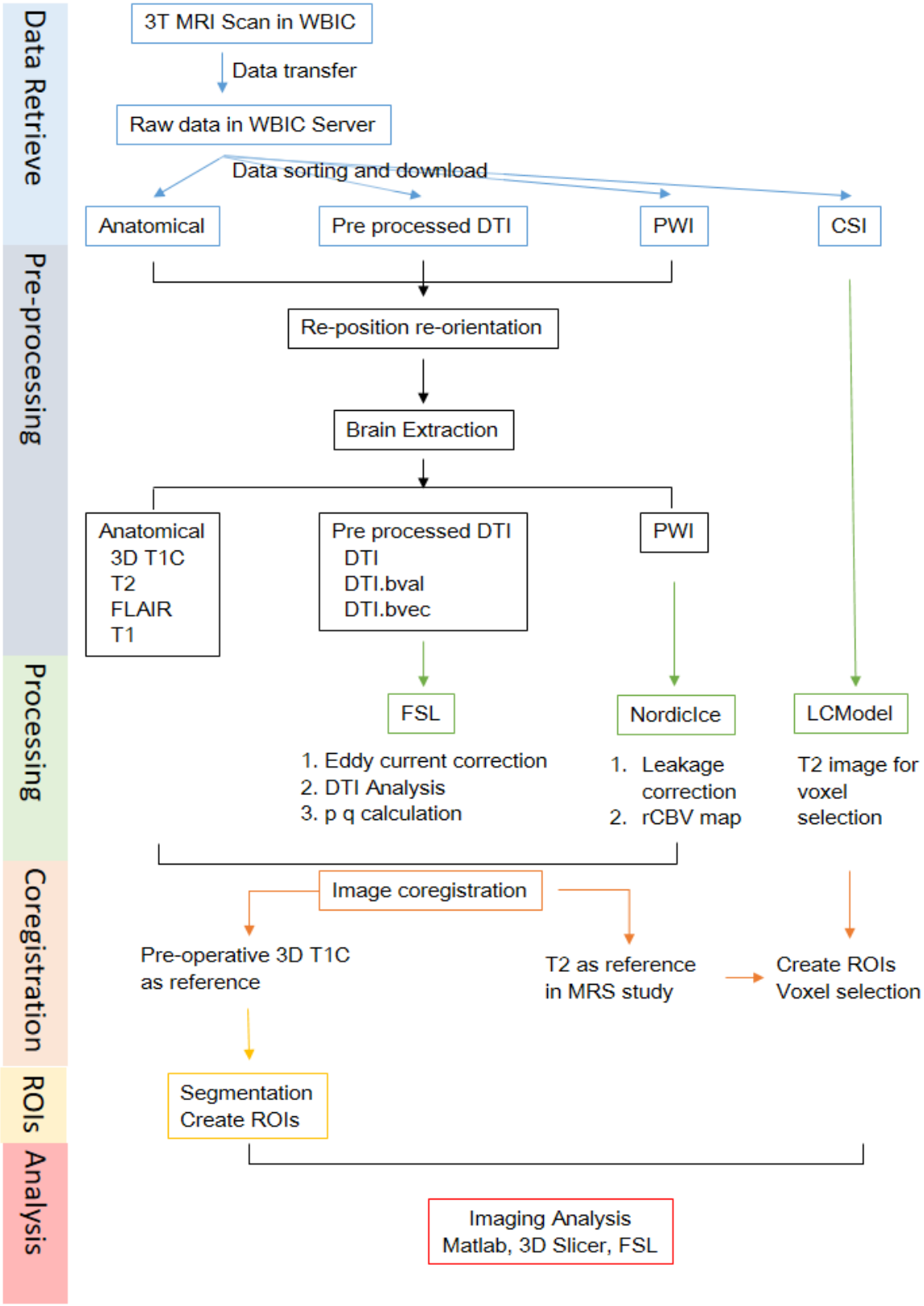

Figure 3.2

Pipeline of Diagnostic MRI acquisition and general imaging processing.

3.2.4 DTI Imaging Procession

DTI images were processed using FSL version 5.0.0 (www.fmrib.ox.ac.uk/fsl)[59]; detailed scripts were listed as appendix B. Reposition and reorientation of the images were done prior to the processing as described above.

Eddy current correction

Eddy current can occurs nearby the conductor whenever magnetic field changes. This effect can cause unwilling stretch or shearing of the images due to the changing of the magnetic field. The effect of eddy current depends on the rate of changes of the magnetic field, therefore in DTI which uses the fast echo-planner imaging can commonly have this artifact. Therefore, eddy current correction is needed before processing by using "eddy_correct" function in FSL FMRIB's diffusion toolbox (FDT).

(Note: a later version of eddy current correction function "eddy" has been recently released in FSL)

Diffusion tensor analysis

Further DTI parameters were then calculated by using FSL "dtifit" function. Outputs of the DTI processing include:

Table 3.2 Outputs from FDT	
FA	Fractional anisotropy
L1, L2, L3	the tensor eigenvalue (magnitude)
MD	Mean diffusivity
MO	Mode of the anisotropy
SO	raw T2 signal with no diffusion weighting (b0)
V1, V2, V3	the tensor eigenvector

ADC was generated directly from scanner with an inline calculation, utilizing b-values 0-1000. Further calculation of the p and q were proceeded by using "fslmaths" function under FSL terminal[100] with the below equation as described previously.

$p = MD \times 1.732$

$q = \sqrt{(\lambda_1 - D)^2 + (\lambda_2 - D)^2 + (\lambda_3 - D)^2}$

Examples of the scanner generated ADC, FDT DTI analysis outputs (MD, FA) and p, q map were shown in figure 3.3.

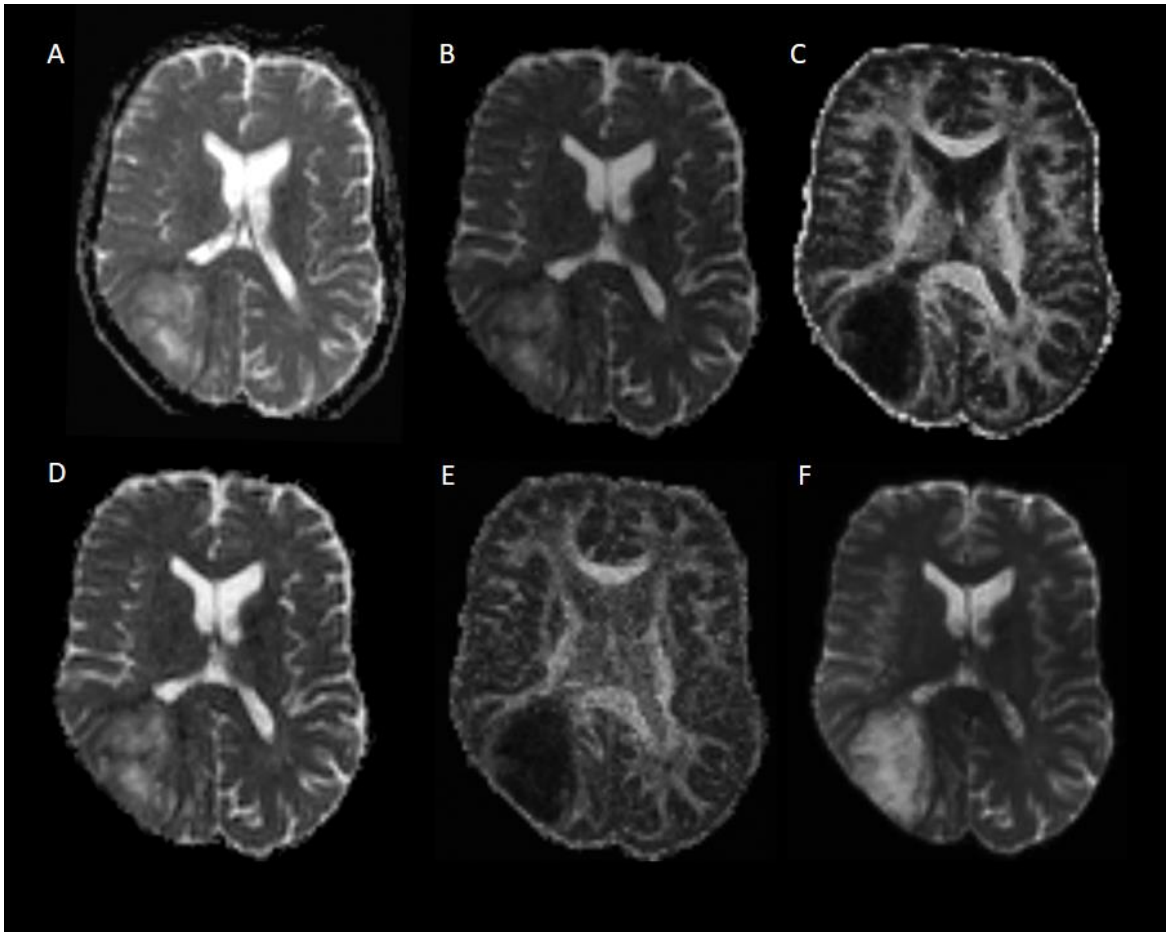

Figure 3.3

Examples from data P100 shown different outputs of DTI analysis. ADC directly from scanner (A), outputs of FDT: MD (B), FA (C), S0 (F) and the calculated DTI p (D), DTI q (E).

3.2.5 Perfusion MRI Processing

Reoriented, unify central point and brain extracted images were prepared before processing perfusion MRI as described above.

NordicICE (NordicNeuroLab, Bergen, Norway, http://www.nordicneurolab.com) was used for the DSC-MRI analysis. Images was then processed with leakage correction and pre-bolus range was set approximately 5-10 ms before contrast. The arterial input function is generated automatically by software. Gamma variate function was used for great vessels and outliers. Relative cerebral blood volume (rCBV), relative cerebral blood flow (rCBF), time to peak (TTP) and mean transit time (MTT) were calculated. An example was shown in figure 3.4.

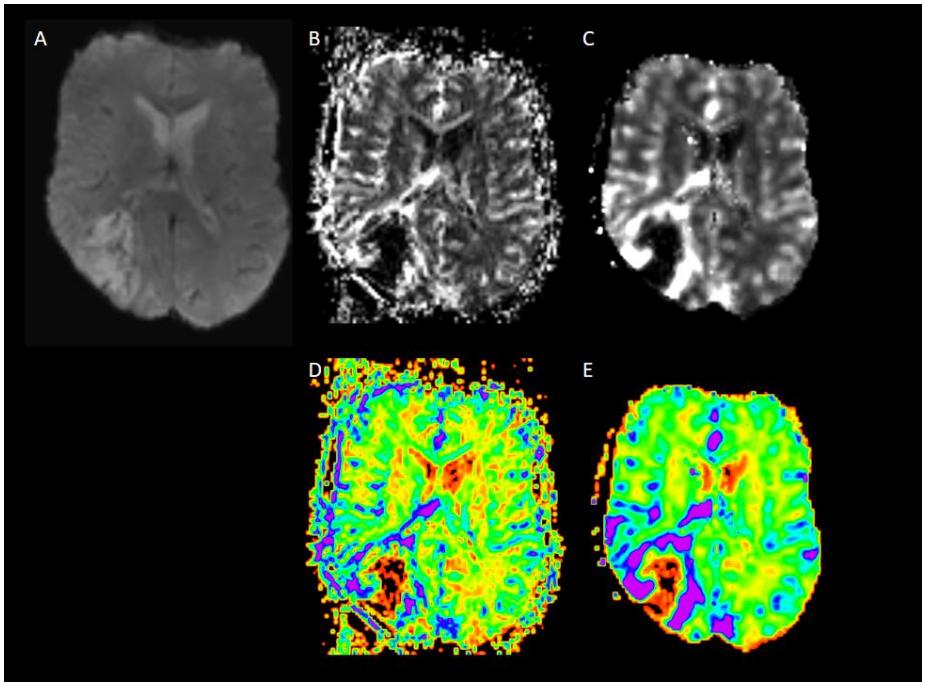

Figure 3.4

An example of DSC-MRI generated from the original PWI (A); rCBV directly from scanner (B) in color map (D), and from NordicICE after leakage correction (C) in color map (E).

3.2.6 MRS Processing

Spectroscopy data were processed by the LC Model. In order to remove the residual water signal, the start of the parts-per-million (ppm) was set at 3.85, and the end of the ppm was set at 1.8 to remove the lipid peak. A grid size 8 x 8 (rows and columns) was selected visually for analysis by radiologists. Normalized metabolites concentration was calculated with absolute concentration divided by Creatine concentration in every voxel in order to avoid the dilution effects associated with the peritumoural oedema[67]. Any normalized voxel data with standard deviation greater than 20% was excluded. For MRS study, all images and ROIs were coregistered to T2 space in order to overlay with the voxel grid which was selected in T2 MRI. (Figure 3.5)

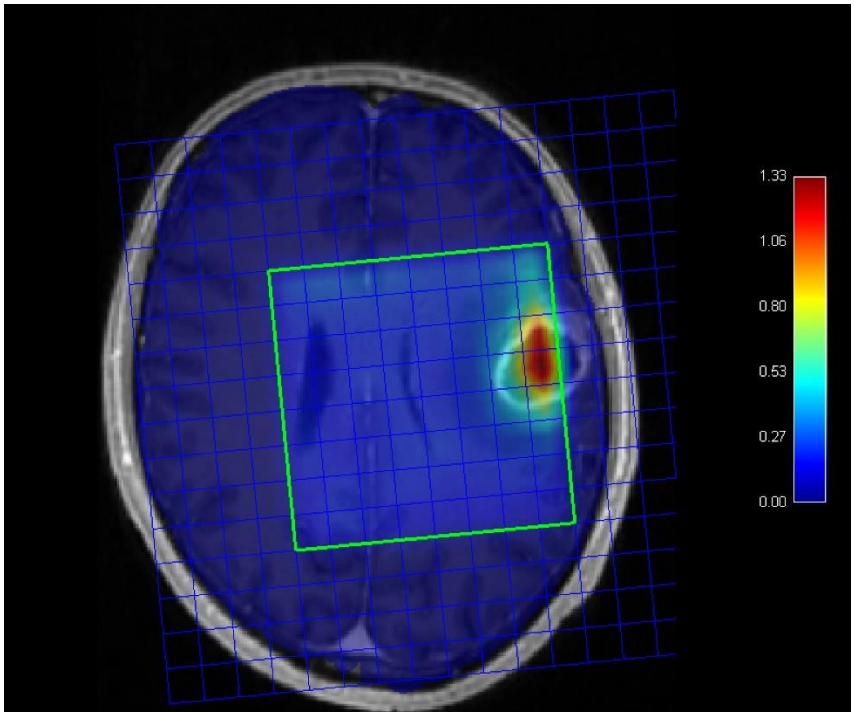

Figure 3.5

An example of combining coregistered T1 with contrast enhancement and the MRS voxel grid. The color map represents the Cho/NAA ratio.

3.2.7 Images coregistration (Figure 3.2 orange section)

All MRI data were coregistered to pre-operative 3D T1 with contrast MRI , except for the MRS study, due to the MRS voxel selection were initially done by using T2 weighted MRI (Figure 3.6).

Images coregistrations were done in two different ways depends on the purposes. For images coregistration within the same scan time point between different sequences, a linear coregistration using “FLIRT” function in FSL with the following script.[58,60]

flirt -ref <reference image> -in <input images> -out <output of FLIRT> -omat <reference transformation> -cost normmi -searchrx -90 90 -searchry -90 90 -searchrz -90 90 -dof 12 -interp trilinear

Such linear coregistration, transformation, translation, scaling and shearing between images can be corrected. However, due to deformation of brain tissue and pathology lesion, this requires a greater degree of freedom to fit these changes. The deformation before and after surgical operation and further due to the nature disease course, FLIRT may fail to achieve optimal co-registration for images between different time points. An example comparing linear and non-linear co-registration between pre- and post-surgical MRI studies by using 3D slicer (http://www.slicer.org/)[33] check border filter (figure 3.7) shows significant torsion in the peripheral area.

Non-linear co-registration, such as FSL FNIRT provides approximately 31,000 degrees of freedom to fit the requirement. An example of registration between pre- and post-surgical T1 weighted with contrast MR is shown in figure 3.8. A grid is added to show the transformation of the images before and after registration and this grid is transformed in a non-linear pattern. By using FSL FNIRT some deformations images

can be well co-registered. A preliminary result to test the torsion of the central area by using septum pallucidum, and cerebral aqueduct also shows substantial deviation on the x coordinate by using the linear FLIRT (Figure 3.9, $p = 0.0038$), and only minimal difference between reference and the non-linear FNIRT coregistered images ($p = 0.2053$).

Although promising results can be achieved in some cases by FNIRT, this is not always the case, particularly in large deformation cases. FNIRT tends to pull two different voxel spaces close in order to minimize the difference. In other words, lesion in the co-registered new image may be significantly torn, due largely to a gap in size between reference and input images, especially while coregistration images from different time points. Thus, a two stage non-linear semi-automatic coregistration was proposed to overcome the problem.[151] Further details will be discussed in Chapter 4.

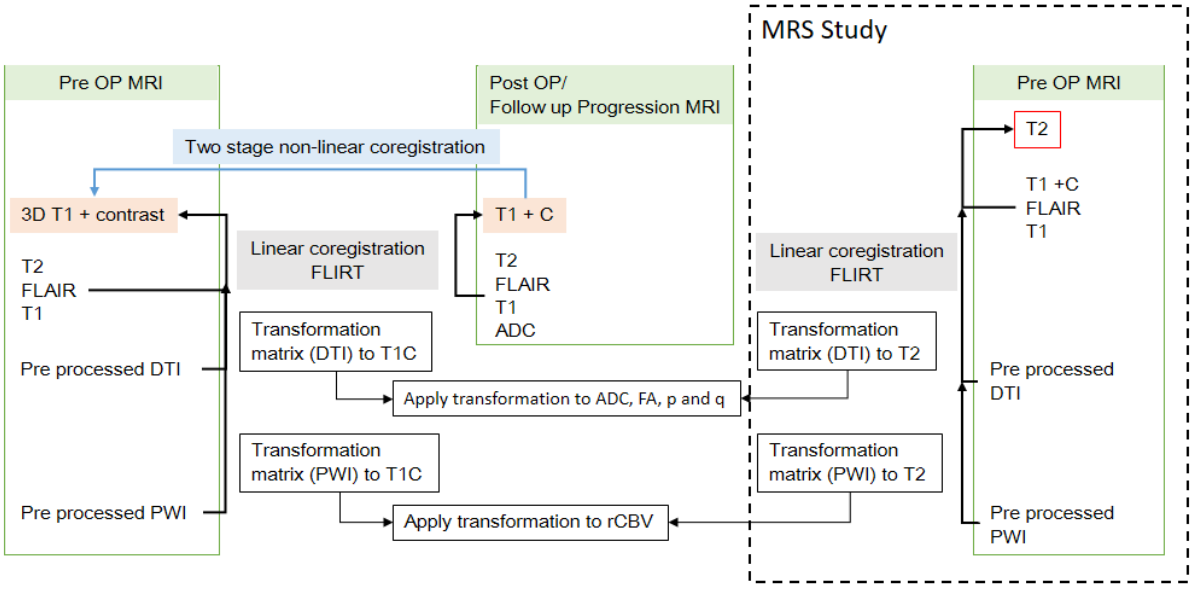

Figure 3.6

Scheme of the coregistration flow. The pre-operative 3D T1 with contrast enhance MRI was used as reference images in most of the study except for the MRS (dotted square). Images within the same time point were coregistered by using linear FLIRT function. The processed DTI (FA, ADC, p, and q) and CBV were coregistered to the reference y applying the transformation matrix generated from the coregistration of the unprocessed DTI and PWI to the reference.

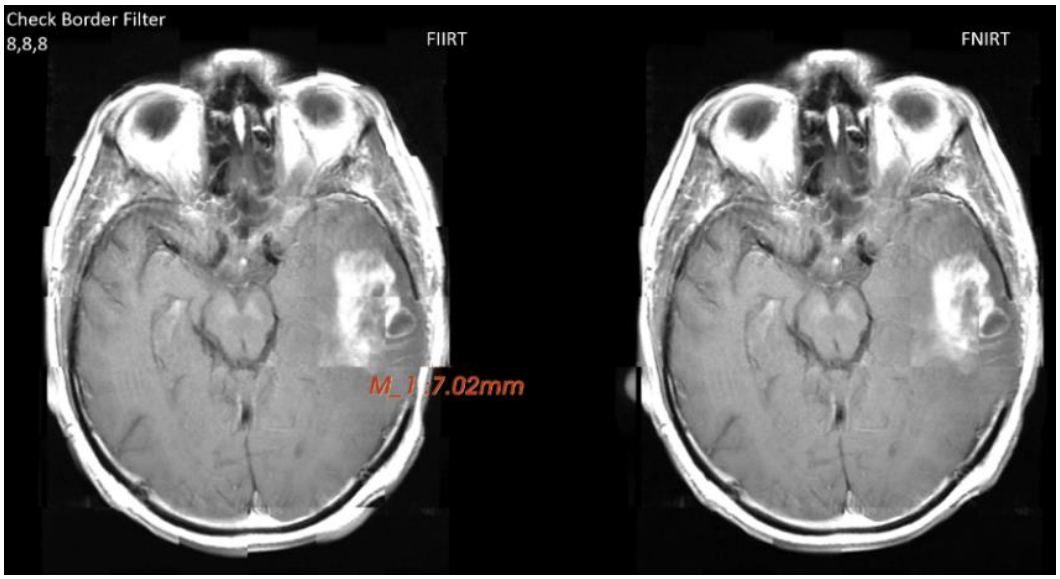

Figure 3.7

Obvious discrimination (7.02mm) by FLIRT (left) can be seen compared to FNIRT (right) by using the check border filter.

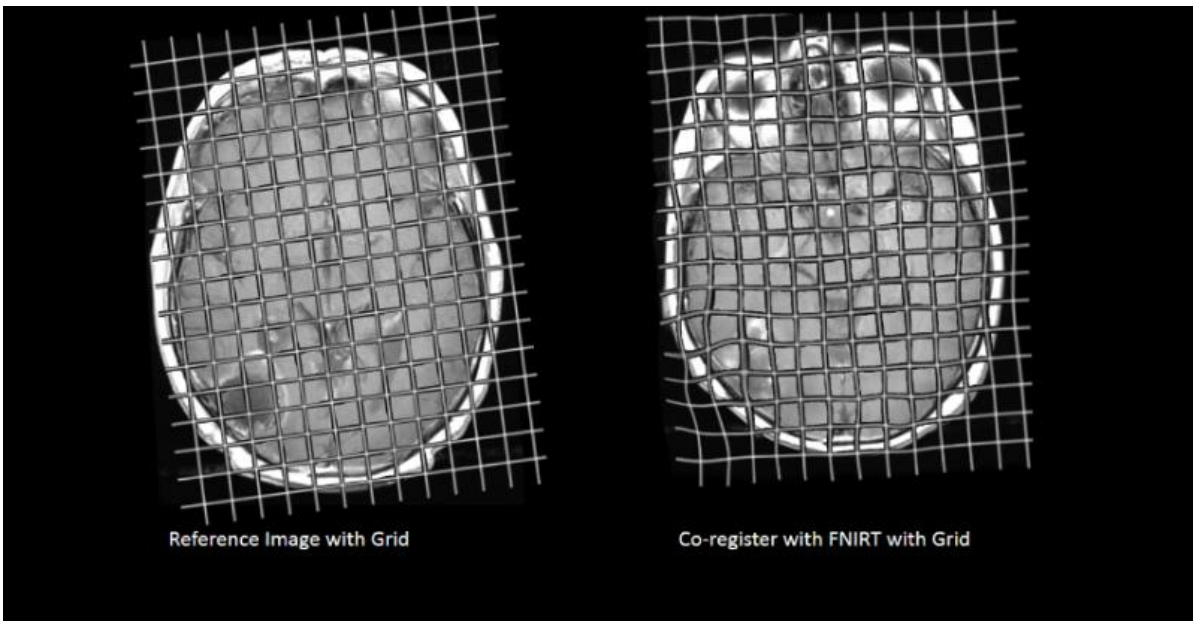

Figure 3.8

The non-linear transformation of the grid represents the deformation of the brain before and after treatment.

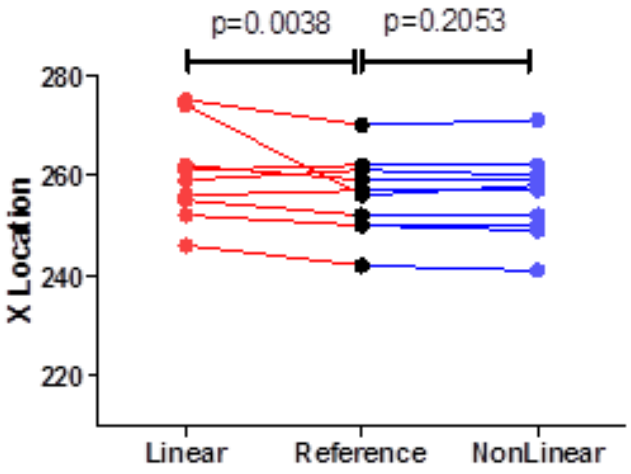

Figure 3.9

Significant deviation on x coordinate using FLIRT with reference of septum pallucidum and cerebral aqueduct in 6 patients. (*paired t-test, p*=0.0038)

3.2.8 Regions of Interest (ROIs) and Image Analysis

Regions of Interest (ROIs) (Figure 3.2 yellow section)

ROIs creation were done by using FSL and 3D slicer (http://www.slicer.org)[33]. 3D slicer is used mainly for manual segmentation. And FSL function "FAST" for automatic segmentation of grey mater, white mater, CSF and contrast enhanced component.

T1 weighted with contrast enhanced ROIs

T1 weighted with contrast enhanced lesion (CE) of the pre-operative study MRI was created semi-automatically. The CE ROIs in this study contains all the volume within the abnormal contrast enhanced area. The 3D volumetric T1 with contrast enhancement MRI firstly underwent automatic segmentation by using FSL function "FAST" (Figure 3.10):

fast –t 1 –n 4 –o <segmentation output> < corrected BET volume >

This would give us segmented mask files including gray mater, white mater, CSF and CE. However, the output mask files usually not binary, therefore "flsmath" function of the FSL is used for binarise.

fslmaths <mask> -div <mask> <binary mask>

Furthermore, due to the interference of the true CE lesion and the normal vascular enhancement, further manual correction was needed to optimize the CE ROIs. The CE ROIs of the post-operative and follow up MRI were drawn manually by using 3D slicer with the assistance of the "level tracing effect".

The CE ROIs were used for the two stage semi-automatic non-linear coregistration method (Chapter 4), extent of GBM resection volumetric study (Chapter 5), the MRS study of the peritumoural abnormal DTI (Chapter 6), and the study of characteristics of the peritumoural progression zone (Chapter 7).

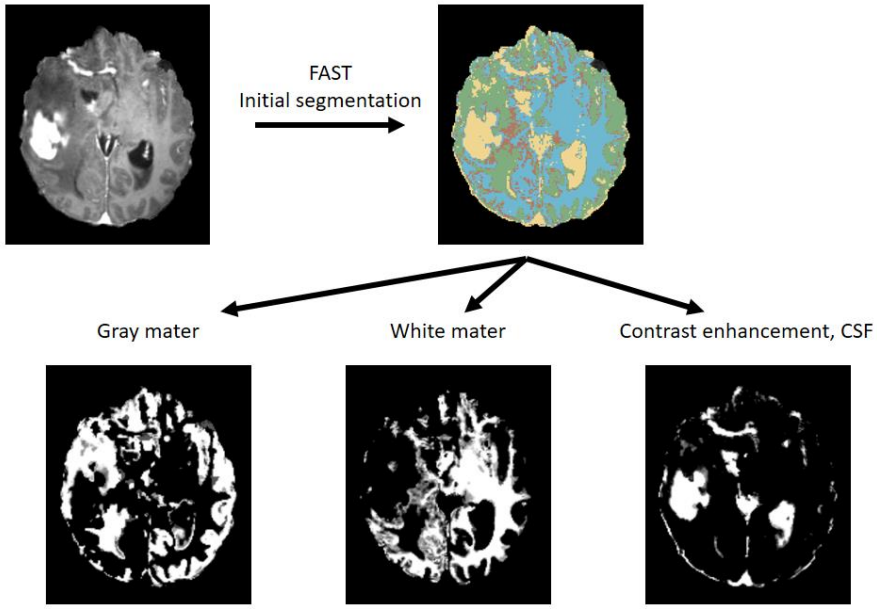

Figure 3.10

Example of “FAST” segmentation from the brain extracted 3D volumetric T1 weighted with contrast MRI to three different mask files, including gray mater, white mater and contrast enhancement (CE) / CSF. Note that the resulting mask files are not binary and the mixture of CE and CSF need further correction.

FLAIR ROIs

The abnormal FLAIR signal represents the oedematous area of the lesion. These ROIs of abnormal FLAIR were created by using 3D slicer with the assistance of the “level tracing effect”. The resulted FLAIR ROIs were used in the extent of GBM resection volumetric study (Chapter 5).

DTI p and q ROIs

The abnormal increase in p and abnormal decrease in q map of the DTI represent the disruption or displacement of the white mater caused by GBM invasion. The ROIs of abnormal p and q were created manually by using 3D slicer with the assistance of the

“level tracing effect”. Inter-rater validation was done with the senior supervisor of the lab, Dr. Stephen J Price. The resulting DICE scores showed an agreement of 0.73 ± 0.11 in the p ROIs and 0.68 ± 0.08 in the q ROIs. These ROIs were used in the extent of GBM resection volumetric study (Chapter 5) and the MRS study of the peritumoural abnormal DTI (Chapter 6).

Normal Appearing White Mater (NAWM) ROIs

The normal appearing white mater (NAWM) ROI was defined as visually normal on MRI study, and was used as control or comparison in studies. This was manually selected on the diagonal quadrant to the tumour, and drawn with a 10 mm diameter square mask by using 3D slicer. The selection of the NAWM ROIs was also inspected by Dr. Anouk van der Hoorn (University Medical Centre Groningen, The Netherlands). These were used in the study of characteristics of the peritumoural progression zone (Chapter 7).

The NAWM ROIs in the MRS study of the peritumoural abnormal DTI were selected visually from the selected MRS voxel grid which located in the diagonal quadrant of the tumour.

Imaging Analysis (Figure 3.2 red section)

Images analysis were done by using different platforms depends on the purposes. General analysis including extraction of the pixel value, images combination, image extraction, and volume calculation were done by using Matlab (The MathWorks, Inc., USA) (APPENDIX C). The analysis of nifty file in the Matlab is proceeded by using the “Tools for NifTi and ANALYZE image” (Copyright (c) 2014, Jimmy Shen).

FSL was used for brain extraction, automatic segmentation, and to binarize images as previous mentioned. The dilatation of the ROIs was also proceeded in FSL.

Specific and detailed imaging analysis procedures would be discussed in individual studies (Chapter 5, 6 and 7).

CHAPTER 4

Validation of a Semi-automatic Co-registration of MRI Scans in Patients with Brain Tumours during Treatment Follow-up[151]

4.1 Introduction

As previously mentioned in Chapter 1, GBM carry a high mortality rate and poor prognosis. One of the unmet needs in treatment development research is the ability to easily identify differences in tumour characteristics and treatment response with MRI imaging biomarkers before, during and after therapy. This would facilitate research on treatment response in large sets of patients and discovery of new imaging biomarkers, further enabling personalization of therapy. In order to meet this demand, an easily applicable coregistration method is needed to coregister postoperative MRI with preoperative images during assessment of high grade gliomas.

The goal of image registration is to find the best transformation to align the structure of the moving images to the reference images. Various imaging registration methods were developed for multi-modality fusion, longitudinal study and population modelling. These methods can be categorised into rigid and non-rigid which includes affine, projective, and the different deformation imaging registration (DIR) methods[91]. In the rigid image registration, the pixel-to-pixel relationship is fixed after the transformation (translation, rotation, scaling and shearing), on the other hand, the pixel-to-pixel relationship changes in the DIR. Before the starting of a typical DIR, a rigid or affine coregistration is needed as a baseline initiation. Then the moving image is coregistered to the reference image according to different DIR algorithms.

The DIR algorithm typically involve three component: an object function, a deformation model, and an optimisation method[130]. The object function is used to define the similarity between image sets and it can be intensity-based, feature-based or both. During this process, the deformation vector field (a defined grid of control points to determine the involved deformation) is generated according to the transformation model, and further applied to the moving image through the Jacobian regularisation to obtain the coregistered image[90].

The transformation models can be classified into parametric and non-parametric. A typical parametric transformation model consists a group of spline models, for example, the B-spline model. Other commonly used parametric model such as statistical parametric mapping which is widely used between different functional neuroimages. Diffeomorphic Demons is one of the commonly used non-parametric transformation model. In contrast to the parametric model which interpolates the deformation vector of many points, it generates the deformation vector field at each voxel. Different coregistration methods have been used in clinical practice or research, and Klein et al. in a comparison of 14 non-linear registration methods concluded that the ART and SyN have the highest accuracy in human brain MRI reistration[66].

As discussed in Section 3.2.7, a nonlinear registration is effective to coregister images in the same time point. However, there are significant challenges when comparing brain MR images at different time points. These changes do not only occur after the initial surgical procedure, but are rather a dynamic continuous process[86]. In addition to the structural changes caused by surgery, tumour response to treatment and chronic radiotherapy effects induce further changes. These changes, for example, in tumour volume and brain volume[126], make the coregistration process even more difficult.

Though previous research has aimed to address these obstacles, an easily accessible and applicable coregistration method is not yet available for preoperative and postoperative MRI scans of patients with brain tumours. Most methods focus on coregistration of different sequences of the same scan time point with linear and nonlinear registration methods in healthy subjects and brain tumour patients. These existing methods demonstrate good performances for this intra-subject coregistration of data from the same time[58,66] or to a standardized brain atlas[82,169]. Research has also demonstrated the value of a nonlinear coregistration for treatment response evaluation in patients without surgery[28]. However, surgery is mandatory to the treatment of the high grade gliomas. Therefore, the ability to deal with these deformation from time to time should be part of the coregistration method.

Methods of MRI coregistration taking resection into account are scarce and have several limitations making them unsuitable as a widely and easily usable coregistration method. The few available clinical studies that have used an intra-subject coregistration method after surgery are difficult to replicate and evaluate as they use in-house software, and provide only limited details of methodology[50,81,148]. Technical studies suffer from other issues, such as small sample size[19]. Furthermore, these and other technical papers do not provide comprehensible coregistration guideline and thereby hinder wide applicability, especially for clinical researchers.

There are a few methods available that coregister intraoperative images with preoperative imaging. However, these are limited by using other modalities, like CT[89], tracked laser range scanning[25] or ultrasound[116]. CT is inferior to MRI in detecting tumour recurrence and thus not routinely used for the treatment evaluation or in

research of brain tumour patients. Ultrasound and laser imaging are only possible during surgery when the skull is temporarily removed. The method from Nithiananthan and colleagues[89] uses an approach that defines resected voxels based on an air density. This is not applicable to research with interest in tumour response assessment using postoperative MRI imaging as the resection cavity being filled with fluid and/or adjacent brain tissue. Other preoperative with intraoperative coregistration methods have only tested the complex algorithm on 2D data[115].

Therefore, a need for an easily applicable and usable coregistration method before, during and after treatment including surgical resection is clearly required. To address this, we developed a semi-automatic coregistration technique using widely used and freely available software. This may allow accurate evaluation of treatment response in future studies, which is essential for brain tumour imaging research and treatment response assessment in large sets of patients. We also provide detailed information about the steps and the code used.

4.2 Methods

Patient inclusion and exclusion criteria were described in Section 3.1. All patient received standard treatment as previous described. In the beginning of this study, 32 patients who had complete follow-up images in Cambridge University Hospital were included (Appendix A-2, unit: C). MRI data acquisition and processing were as described in section 3.2 described.

4.2.1 Semi-automatic co-registration method

Coregistration was performed using a two-staged semi-automatic method (Figure 4.1) using FSL. Before the coregistration stages commence, all images were realigned with the anterior commissure as the center point (coordinate 0, 0, 0) to minimize the influence of brain position (as described in section 3.2.3).

The first stage was the coregistration of the binary masks, which consisted of the outer contour of the brain, the ventricles, and contrast enhancing area (presurgical MRI images, Figure 4.2, [X]) or resection area (follow up MRI images, Figure 4.2, [Y]). This was performed for each subject at the different time points to create a transformation matrix (Figure 4.1, step 4, Figure 4.2, A) using the FLIRT, FMRIB's linear image registration tool function. The brain contours were created from the inversion of the brain masks which were semi-automatically extracted[128] followed by manual correction (Figure 4.1, step 1 and 2) and further binaries the resulted mask. The ventricles were identified with an automatic segmentation using the FSL FAST (Figure 4.1, step 3, FMRIB's automated segmentation tool) function[170]. The FAST function also allowed a semi-automatic identification of the contrast enhancing area or resection cavity. The contrast enhancing area is targeted for resection and is replaced by the resection cavity on the direct postoperative and later follow-up MRI scans. Besides, in cases without postoperative resection cavity, the algorithm can still work by including

also the non-tumour part which is ventricle and outer contour of brain. Therefore, this stage of coregistration allowed for optimal correction of variable brain shift and surgery-induced changes at different time points.

The second stage applied the transformation matrix, acquired from the first stage, as input for a nonlinear transformation matrix of the brain images (Figure 4.1, step 5 and 6, using the FNIRT, FMRIB's non-linear image registration tool, functions). The nonlinear transformation of the brain images used additional subsampling levels for regularization. This also included the binary masks of the brain contour and ventricles from both the preoperative reference image and the follow-up image. This resulted in a coregistration of the follow-up brain extracted MRI scans with the preoperative brain extracted MRI scans. Detailed script of this algorithm is provided in Appendix D. Standard linear coregistration (FLIRT function) and standard FNIRT with default setting were done separately for comparison using the FLIRT and FNIRT option in FSL.

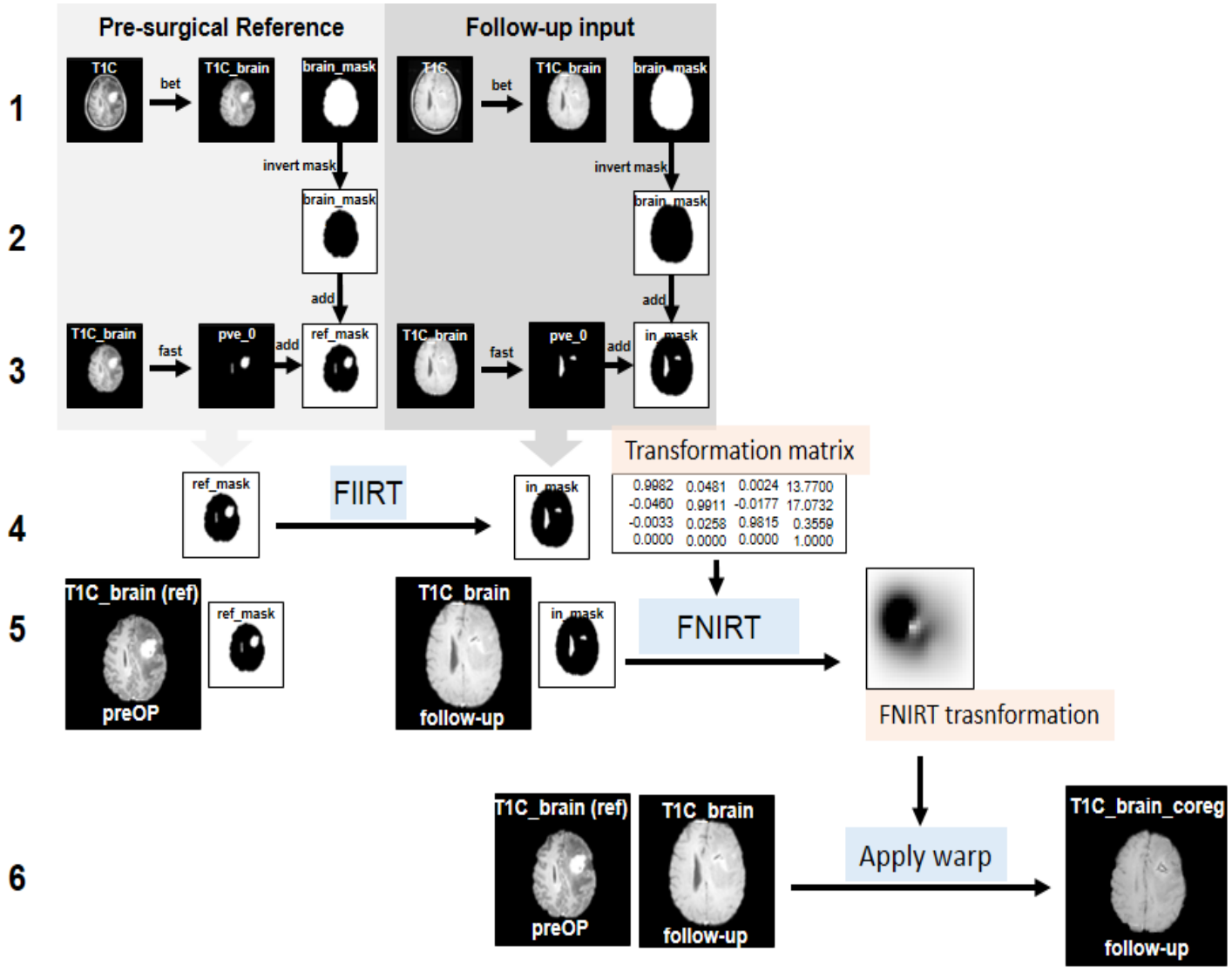

Figure 4.1 Coregistration steps

The steps for the semi-automatic coregistration of the follow-up image with the preoperative reference image are illustrated. Number of the steps and filenames correspond to the text in the supporting material. The corresponding code can also be found in the text of the supporting material.

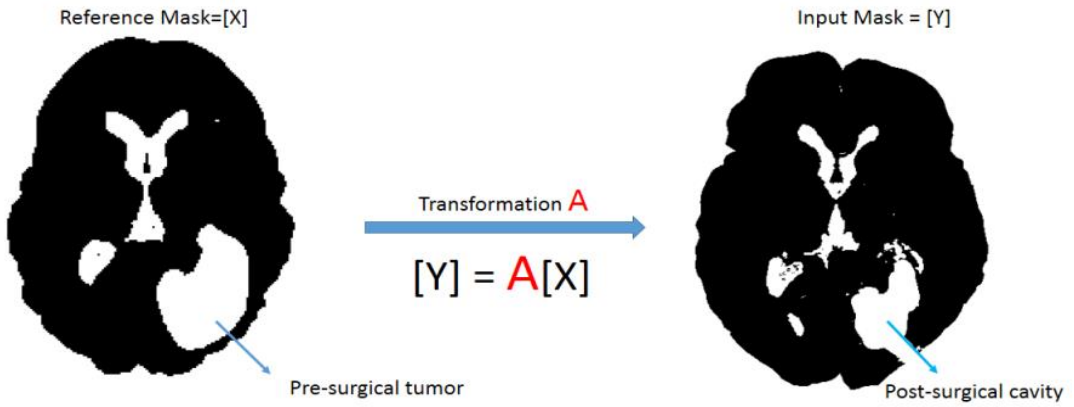

Figure 4.2 Calculating for reference transformation

First stage of the coregistration aim to calculate the transformation matrix A of the contrast enhancing lesion to the post-surgical cavity. [X] = reference mask, including the presurgical contrast enhancing lesion, ventricle and external brain area; [Y] = input mask, referred to post-surgical cavity, ventricle and the external brain area; A = transformation between [X] and [Y]

4.2.2 Validation methods

Validation was performed using a targeted registration error method for calculating the error in different directions. Validation in the x and y directions was performed utilizing the cerebral aqueduct and septum pellucidum on the same axial slice (Figure 4.3A). Validating in the y and z directions (Figure 4.3B) was performed utilizing the upper anterior boundary of the third ventricle, at the level of the foramen of Monro (Figure 4.3C), on the same coronal slice. The central point of the tumour or cavity was targeted automatically for the calculation of the registration error at the location were most errors could be expected. Vectors were also calculated for all targets. All targeted registration errors were calculated for the semi-automatic non-linear coregistration method and compared to the linear coregistered and standard non-linear coregistered images. Differences were tested with a Wilcoxon signed rank test or paired t-test depending on the normality. Two-sided p-values were used.

A

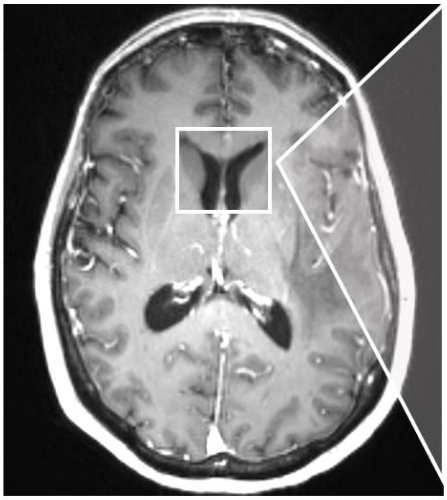

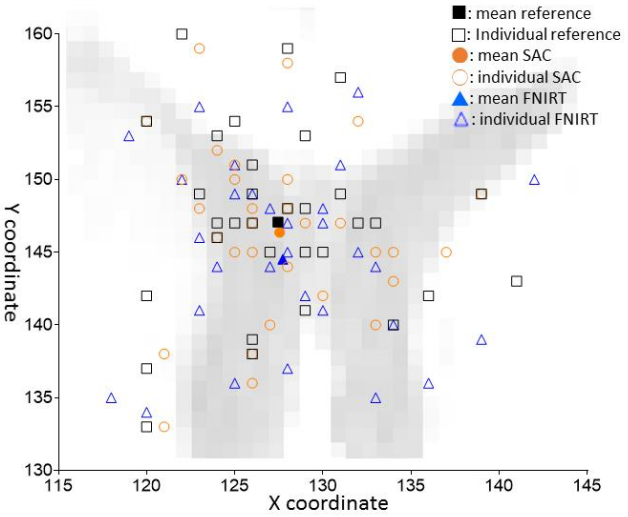
■: mean reference
□: Individual reference
●: mean SAC
○: individual SAC
▲: mean FNIRT
△: individual FNIRT
Y coordinate
X coordinate
160
155
150
145
140
135
130
115
120
125
130
135
140
145

B

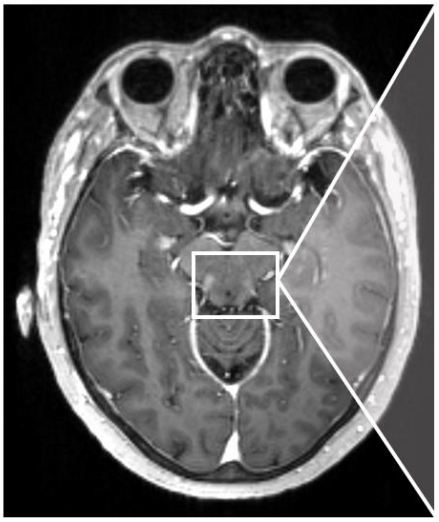

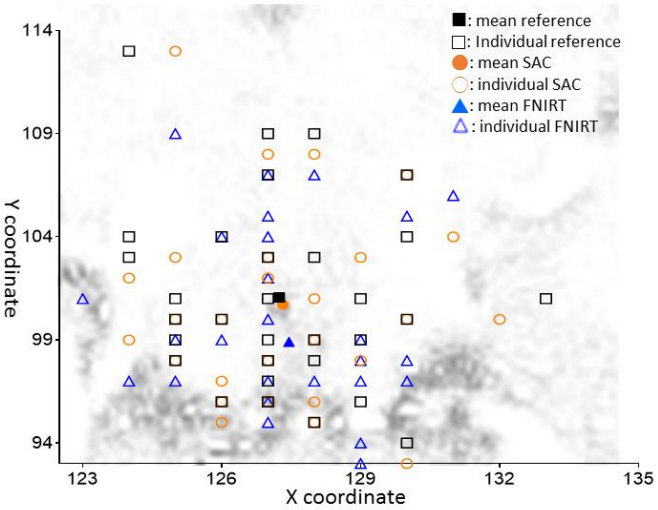
■: mean reference
□: Individual reference
●: mean SAC
○: individual SAC
▲: mean FNIRT
△: individual FNIRT
Y coordinate
X coordinate
114
109
104
99
94
123
126
129
132
135

C

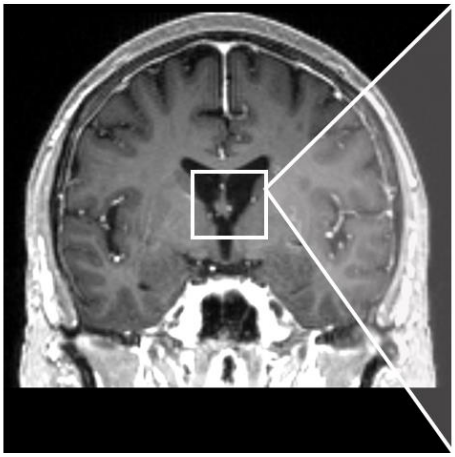

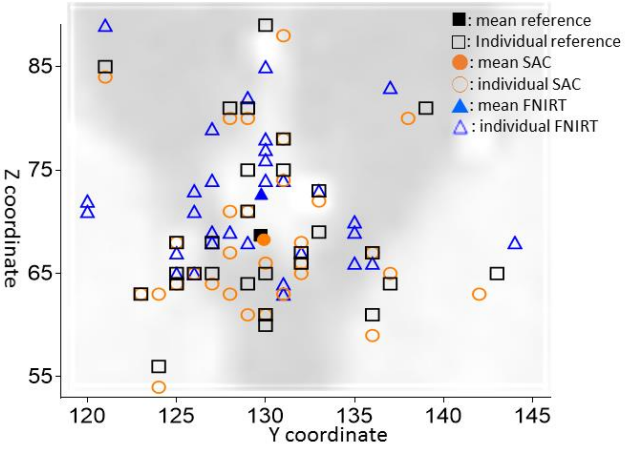
■: mean reference
□: Individual reference
●: mean SAC
○: individual SAC
▲: mean FNIRT
△: individual FNIRT
Z coordinate
Y coordinate
85
75
65
55
120
125
130
135
140
145

Figure 4.3 Targeted registration errors

Targeted registration errors are shown for the septum pellucidum in axial view (A), cerebral aqueduct in axial view (B) and the uppermost of the third ventricle (C). Images on the left show individual cases to illustrate the locations of the targets and the graphs on the right correspond to the whole patient set. Squares indicate coordinates for the presurgical MRI. The group mean is indicated by a filled square (■) and individual patients by open squares (□). Circles indicate the co-registered image differences after semi-automatic non-linear co-registration (SAC) of postoperative and preoperative images. The group mean is indicated by a filled circle (●) and individual patients are indicated by open circles (○). Triangles indicate the co-registered image difference after FNIRT (FMRIB's Non-Linear Image Registration Tool) non-linear co-registration of postoperative and preoperative images. The group mean is indicated by a filled triangle (▲) and individual patients are indicated by open triangles (Δ).

In addition, a 3D structural similarity map (SSIM) was created[157] using Matlab. Structural similarity map decomposes image quality into structure, contrast and lamination and compares each voxel by other voxels. It is created for each subject comparing the preoperative reference scan with the coregistered follow-up scan. The function is described as below:

$$\mathrm{SSIM}(\mathbf{x},\mathbf{y}) = [l(\mathbf{x},\mathbf{y})]^{\alpha}[c(\mathbf{x},\mathbf{y})]^{\beta}[s(\mathbf{x},\mathbf{y})]^{\gamma}$$

l = lamination; c = contrast; s = structure

If two images (x, y) are equally similar to each other, SSIM(x, y) = 1

$$\mathrm{SSIM}(\mathbf{x},\mathbf{x}) = \frac{2\mu_x^2 + C_1}{\mu_x^2 + \mu_x^2 + C_1} \times \frac{2\sigma_x^2 + C_2}{\sigma_x^2 + \sigma_x^2 + C_2} \times \frac{\sigma_{xx} + C_3}{\sigma_x\sigma_x + C_3} = 1$$

μ = mean; σ = standard deviation; C = constant

On the other hand, if two images or volume are completely different, SSIM will be -1.

This was done for scans obtained postoperatively and at tumour recurrence separately. To display group results, the preoperative images were coregistered to standard MNI (Montreal Neurological Institute) space with a nonlinear transformation of the brain images including a lesion mask. This was preceded by a linear transformation of a binary mask of the brain exterior and ventricles. A mean structural similarity mask was then created by transforming the structural similarity mask of each patient to standard MNI space. The resection cavity or contrast enhancing areas were excluded for the mean structural similarity image, as these values are inherently different.

4.3 Results

4.3.1 Targeted registration error

The targeted registration error showed good performance of the co-registration method for the direct postoperative and recurrence images with a clear benefit over the linear coregistration method and standard FNIRT non-linear co-registration method (Table 4.1). In the co-registration of postoperative to preoperative images, in comparison with FLIRT, the SAC method showed a smaller vector deviation of the cerebral aqueduct (1.1 versus 1.6, $p = 0.015$). A smaller deviation was also detected for the septum pallucidum y coordinate and vector (1.3 versus 2.0, $p = 0.029$; 1.8 versus 2.6, $p = 0.021$), as well as the uppermost of the third ventricle y, z coordinate and vector (0.4 versus 2.2, $p < 0.001$; 1.2 versus 1.9, $p = 0.043$; 1.3 versus 3.3, $p < 0.001$). The SAC method also outperformed the default FNIRT co-registration, where there was small deviation between preoperative and postoperative images for most of the coordinates and vectors in the central tumour/cavity point, cerebral aqueduct, septum pellucidum and the third ventricle at the level of the foramen of Monro.

The benefit of this co-registration method can also be seen in the co-registration of recurrence images to preoperative images (Table 4.2). The target error at the cerebral aqueduct and the roof of the third ventricle at the level of the foramen of Monro was smaller using the SAC method than the linear co-registration and FNIRT co-registration. When using default FNIRT, there was a larger z coordinate deviation at the tumour centroid point. In addition, the linear co-registration failed in three patients, and default FNIRT co-registration failed in two patients, for both the postoperative and recurrence scan, whereas the semi-automatic method was used without problems.

TABLE 4.1 – Targeted coregistration errors between pre- and post-operation

		Postoperative with preoperative				
		SAC	**FLIRT**	**FNIRT**	***SAC versus FLIRT***	***SAC versus FNIRT***
		mean (range)	**mean (range)**	**mean (range)**	***P*-value**	***P*-value**
Central	**x**	3.0 (0.3-10.6)	3.3 (0.3-10.6)	7.0 (0.1-46.6)	0.242	0.023*
tumour/	**y**	2.5 (0.1-7.4)	2.8 (0.1-8.3)	4.8 (0.2-28.2)	0.256	0.031*
cavity	**z**	2.6 (0.0-8.1)	2.7 (0.1-10.3)	5.2 (0.4-57.0)	0.758	0.003*
	vector	5.3 (1.5-11.1)	5.7 (1.3-15.2)	11.6 (0.3-16.9)	0.099	0.002*
Cerebral	**x**	0.5 (0.0-1.0)	0.7 (0.0-5.0)	0.6 (0.0-4.0)	0.166	0.305
aqueduct	**y**	0.8 (0.0-3.0)	1.2 (0.0-5.0)	2.7 (0.0-6.0)	0.051	<0.001*
	vector	1.1 (0.0-3.2)	1.6 (0.0-5.4)	2.9 (0.0-6.1)	0.015*	<0.001*
Septum	**x**	0.8 (0.0-4.0)	1.3 (0.0-9.0)	1.2 (0.0-9.0)	0.132	0.280
pellucidum	**y**	1.3 (0.0-4.0)	2.0 (1.0-8.0)	3.6 (1.0-7.0)	0.029*	<0.001*
	vector	1.8 (0.0-4.5)	2.6 (0.0-9.1)	4.0 (2.7-108.5)	0.021*	<0.001*
Third	**y**	0.4 (0.0-1.0)	2.2 (0.0-18.0)	1.7 (0.0-6.0)	<0.001*	<0.001*
ventricle	**z**	1.2 (0.0-4.0)	1.9 (0.0-14.0)	3.9 (0.0-12.0)	0.043*	<0.001*
	vector	1.3 (0.0-4.1)	3.3 (0.0-18.0)	4.5 (1.0-12.4)	<0.001*	<0.001*

Targeted registration errors are provided with the deviations (mm) of the anatomical landmark coordinates from the reference images after co-registration of the postoperative with the preoperative scan. The semi-automatic non-linear co-registration (SAC), linear (FLIRT, FSL) and default non-linear (FNIRT, FSL) co-registration are compared. An asterisk indicates statistical significance.

TABLE 4.2 – Targeted coregistration errors between pre-operation and recurrence

		Recurrence with preoperative				
		SAC	**FLIRT**	**FNIRT**	***SAC versus FLIRT***	***SAC versus FNIRT***
		mean (range)	**mean (range)**	**mean (range)**	***P*-value**	***P*-value**
Central	**x**	5.0 (0.2-15.9)	5.6 (0.3-16.3)	9.9 (0.4-73.7)	0.204	0.131
tumour/	**y**	4.0 (0.3-16.4)	3.0 (0.3-8.6)	13.6 (0.5-13.1)	0.247	0.226
cavity	**z**	5.0 (0.5-15.1)	4.2 (0.1-13.2)	11.5 (0.3-29.5)	0.297	0.008*
	vector	9.1 (0.9-20.2)	10.0 (0.9-24.4)	23.3 (2.7-108.5)	0.875	0.102
Cerebral	**x**	1.2 (0.0-5.0)	1.3 (0.0-4.0)	0.8 (0.0-6.0)	0.822	0.280
aqueduct	**y**	1.3 (0.0-3.0)	2.1 (0.0-5.0)	2.3 (0.0-8.0)	0.004*	0.032*
	vector	2.0 (0.0-5.8)	2.8 (0.0-5.0)	2.7 (0.0-8.2)	0.016*	0.124
Septum	**x**	2.8 (0.0-12.0)	3.3 (0.0-14.0)	2.0 (0.0-19.0)	0.2132	0.188
pellucidum	**y**	2.8 (0.0-15.0)	2.8 (0.0-16.0)	3.0 (0.0-17.0)	1.0000	0.779
	vector	4.3 (1.0-19.0)	4.6 (0.0-20.6)	4.1 (0.0-10.2)	0.7280	0.782
Third	**y**	0.6 (0.0-3.0)	3.0 (0.0-16.0)	3.1 (0.0-11.0)	0.0010*	0.001*
ventricle	**z**	2.6 (0.0-9.0)	2.5 (0.0-13.0)	3.1 (0.0-16.0)	0.8898	0.466
	vector	2.7 (0.0-9.1)	4.6 (1.0-16.0)	5.1 (0.0-16.5)	0.0112*	0.006*

Targeted registration errors are provided with the deviations (mm) of the anatomical landmark coordinates from the reference images after co-registration of the recurrence with the preoperative scan. The semi-automatic non-linear co-registration (SAC), linear (FLIRT, FSL) and default non-linear (FNIRT, FSL) co-registration are compared. An asterisk indicates statistical significance.

4.3.2 3D structure similarity

The mean 3D structural similarity of all 32 patients showed the relative performance of the co-registration method (Figure 4.4). The peripheral areas, including the frontal and parietal areas, demonstrated the best performance. A good performance was also seen at the periventricular regions. A relatively smaller overlap between the co-registered and reference preoperative scans was seen in the mid-sagittal and central areas, the centrum semiovale and central cerebellum. Mean SSIM value between semi-automatic co-registration, direct FNIRT and FLIRT is shown in Figure 4.5.

An example of this co-registration is shown in Figure 4.6. Without appropriate co-registration, one cannot confidently compare the initial postoperative or tumour recurrence images with the pre-operative reference images (Figure 4.6 A). Although the standard FNIRT co-registration of postoperative MR and recurrence MR images (Figure 4.6 B) realigned the images in the same space as the reference images, regional torsions (white arrows) were detected at the resection edges. Using the semi-automatic co-registration methods, the co-registered postoperative MR (Fig. 4.6 C, left) and recurrence MR (Fig. 4.6 C, middle) images were able to show the residual contrast-enhanced lesion (yellow contour) and the recurrent area (red contour) in the reference MR image (Fig. 4.6 C).

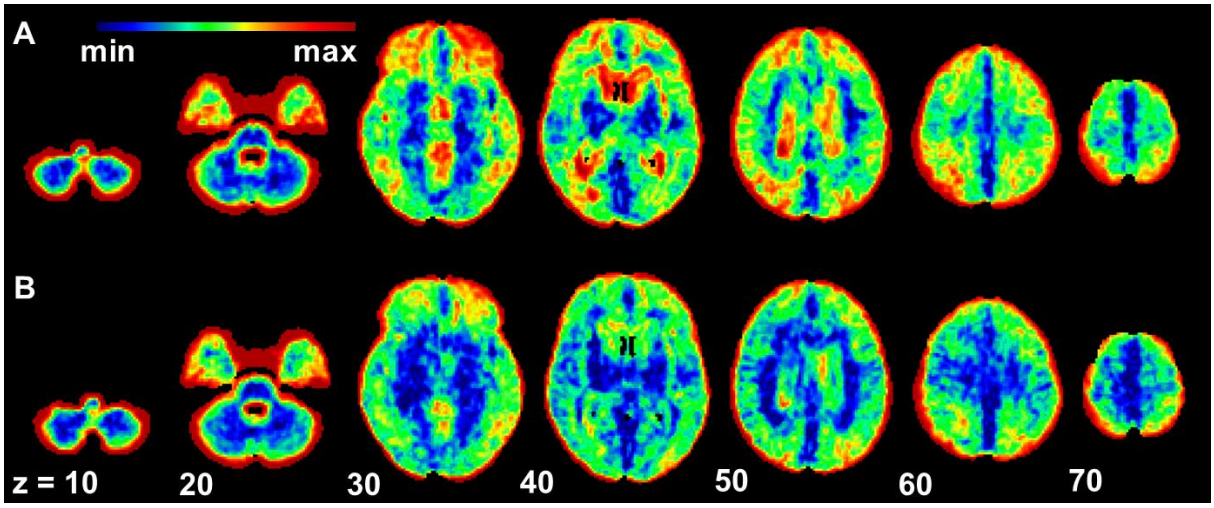

Figure 4.4 Mean 3D group structural similarity for co-registration

The group mean 3D structural similarity of all 32 cases is shown for the direct postoperative MRI (A) and later follow-up MRI at the time point of tumour recurrence (B), both co-registered to the preoperative MRI. Values indicate the relative structural similarity between the co-registered and original preoperative scans for the group mean, with higher values indicating a greater similarity between the images being compared. The color bar shows the degree of similarity from totally identical (max, red) to 0% similar (min, black).

Figure 4.5 Mean of the SSIM between different coregistration methods

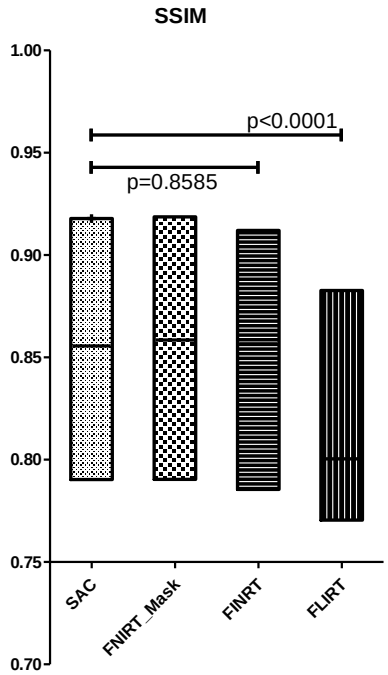

A significant higher SSIM mean value was noted between SAC and FLIRT (p<0.0001). SAC showed slightly higher SSIM mean value than direct FNIRT, but without significance.

SAC = semi-automatic co-registration

FNIRT_Mask = FNIRT with SAN reference mask

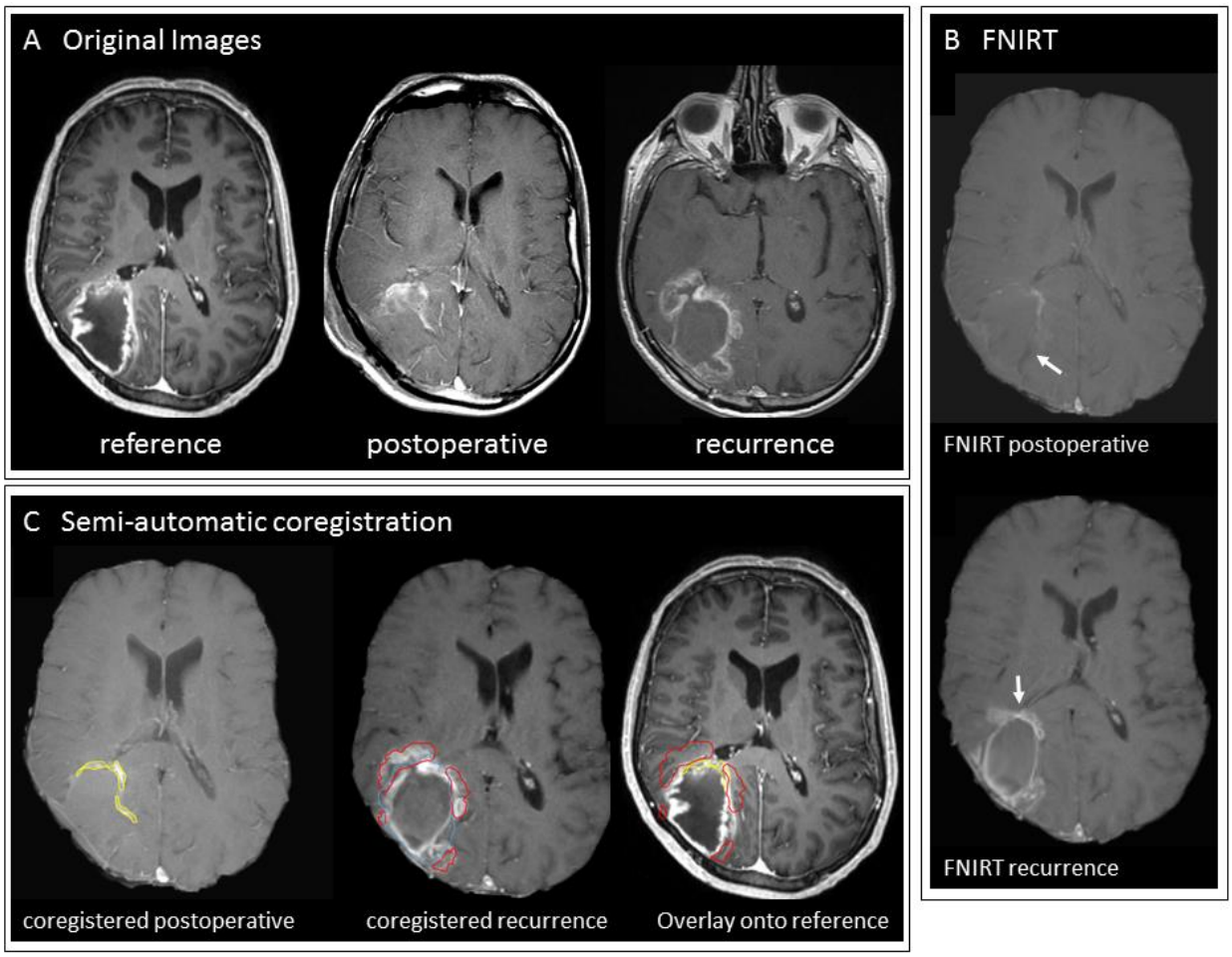

Figure 4.6 Examples of the two-stage semi-automatic non-linear co-registration

Without co-registration, the postoperative and recurrence images are difficult to compare with the preoperative reference image (A). With standard FNIRT (FMRIB's Non-Linear Image Registration Tool) co-registration (B), although the gross brain positions are realigned in both postoperative and recurrence images, regional torsion, especially around the lesion (white arrow), may occur. After semi-automatic co-registration (C), postoperative residual regions (C, left, yellow outline) and recurrence regions (C, middle, red outline) can be fitted with the preoperative reference image (C, right).

4.4 Discussion and Conclusion

Discussion

We developed and validated a two staged semi-automatic method for the coregistration of preoperative and follow-up MRI scans for both the direct postoperative and tumour recurrence time point (Table 4.1, Table 4.2, and Figure 4.5). The semi-automatic derived mask of the outer brain contour, ventricles and lesion allowed an accurate coregistration despite the changes in brain shift and postoperative changes. Therefore, this method is highly applicable to analyze large imaging datasets to evaluate treatment response, a growing and clinically important research area. Furthermore, it can be easily reproduced, allowing a wide applicability of the method.

In the standard FNIRT function, an affine transformation is required as a starting guess of the coregistration. This affine transformation is typically the result of linear FLIRT coregistration between different MR series. However, the deformation in different time points happens mainly over the peritumoural regions, resection cavities, and ventricles. Our approach was to use the transformation affine of these areas with the greatest changes rather than the whole brain images (Figure 4.1 step 4). Furthermore, we added an inverted brain mask as an outer frame to our first stage coregistration for the gross spatial position (Figure 4.1 step 2 and 3). This resulting affine was further applied to the normal brain parenchyma with the mask of ventricle and lesion (Figure 4.1 step 5) to achieve the optimal coregistration. Previous studies utilizing intraoperative coregistration have shown a clear advantage of nonlinear coregistration with high diagnostic and stereotactic accuracy[28]. This supports the results of the postoperative coregistrations from our study.

To the best of our knowledge, there is a shortage of easily applicable methods that allow coregistration of preoperative and postoperative imaging in patients with brain tumours. Clinical papers often use in-house software solutions and provide only partial description of the methodology. This two-staged semi-automatic coregistration method can be replicated by using the FMRIB Software Library which is a freely available and widely used software package in the neuroimaging research community. We have provided a detailed description of the steps required to recapitulate this approach (see Figure 4.1 and Appendix D). This makes this method easily reproducible by others, including clinical researchers, which further supported the rationale of using FSL for our coregistration method. Given this purpose of this study, we have not tried to validate the coregistration of patients with brain tumours using other software packages. Interpolation of our semi-automatic method to other software packages might be possible, but would require separate validation.

The MR image acquisition parameters in our dataset varied across subjects and time points. In particular, a 3D T1-weighted with contrast enhancement dataset was available for the preoperative scan, but the follow-up images were almost always 2D and obtained with different MRI parameters and scanners from different manufacturers. Another limitation is that this method assumes that the resection cavity is a result of surgical resection of contrast-enhancing tumour only, and that the recurrent tumour arises from the non-contrast- enhancing surrounding area. However, the resection volume may extend beyond the area of contrast enhancement to include the 'peritumoural region', particularly if the resection is conducted under the fluorescence guidance of 5-aminoleuvulinic acid[122]. Despite these differences, our validation showed that the method worked in all subjects, making it easily applicable in clinical practice.

At a time when adequate imaging biomarkers are being sought to evaluate treatment response, method applicability is of essence for the development of brain tumour research. Overcoming these treatment induced problems in the coregistration makes our semi-automatic coregistration a valuable method to facilitate research in the expanding area of personalized medicine in brain tumour patients.

Conclusion

We developed a semi-automatic coregistration method for MRI images of brain tumours to allow the accurate evaluation of treatment response in further research. We have demonstrated show good performance of this approach using 3D structural similarity and targeted registration error methods. We have also provided a detailed description of methodology using freely available software, making it reproducible by the neuroimaging community. This is an essential tool for the growing research area of brain tumour imaging and treatment response evaluation in large sets of patients.

CHAPTER 5

Extent of Resection of Peritumoural Diffusion Tensor Imaging–detected Abnormality as a Predictor of Survival in Adult Glioblastoma Patients[166]

5.1 Introduction

As described in Chapter 1, GBM is a malignant cancer with high local failure rate. The main factors influencing prognosis are age, performance status, tumour molecular type, and extent of resection (EOR), of which the former three are fixed and the latter can be changed. Therefore, many efforts have made to improve the extent of maximal tumour resection while preserving normal brain tissue and function[45,48,68]. To achieve maximal tumour resection, intraoperative neuronavigation, 5-aminolevulinic acid (5-ALA) and other imaging techniques (e.g., intraoperative MRI or ultrasound) have been introduced. Use of 5-ALA increased the EOR to 60-65% of the total contrast-enhanced area and prolong the progression-free survival[135,137].

A contrast-enhanced T1-weighted signal has many limitations in accuracy of the delineation of tumour margin (Chapter 1.3.1). Consequently, the clinical benefit of resection outside the contrast-enhanced area has been investigated[73]. Recently, it has been shown that extending the resection to the peritumoural high T2 signal areas beyond the enhanced lesion on postcontrast T1-weighted images can provide longer survival than less extensive resections[73]. This is thought to be due to tumour infiltration beyond the contrast-enhanced area[118]. However, a high signal on T2-weighted imaging is not specific for tumour infiltration, because it is also caused by oedema.

Application of the DTI, especially by decomposing the diffusion tensor into an isotropic component (p) and an anisotropic component (q) can detect tumour extent beyond the contrast-enhanced area because of subtle white matter changes. Detailed rationale of the DTI and its application has been discussed in Chapter 1.3.2.

Therefore, this prompted our study analyzing the influences of the EOR of abnormal peritumoural DTI areas on patients' outcome.

5.2 Method

Patient Population and Treatment

The inclusion, exclusion criteria and the treatment were shown on Chapter 3.2.

We included 31 glioblastoma patients (mean age 56 years, range 31-68 years; 19 men and 12 women) who received complete follow up more than one year in Cambridge University Hospital from our consecutive cohort (Appendix A, Lab code: up to 113, Unit: C, P). At the time of the study, cases with lab code more than 113 haven't received follow-up more than one year.

Imaging Processing

MRI data acquisition and imaging processing were described in Chapter 3.2. The coregistration method between post-operative MRI and baseline MRI were done by using the two-stage non-linear semi-automatic coregistration methods (Chapter 4). General Imaging work scheme was shown in Figure 5.1 by using the contrast enhanced T1 weighted MRI as example. After the co-registration of the post-operative to the pre-operative MRI, we further apply the generated transformation to the resection cavity (Figure 5.2, green mask) to achieve the coregistered resection cavity (Figure 5.2 blue mask) which can be further calculated for the extent of resection. Detailed description is shown in appendix E.

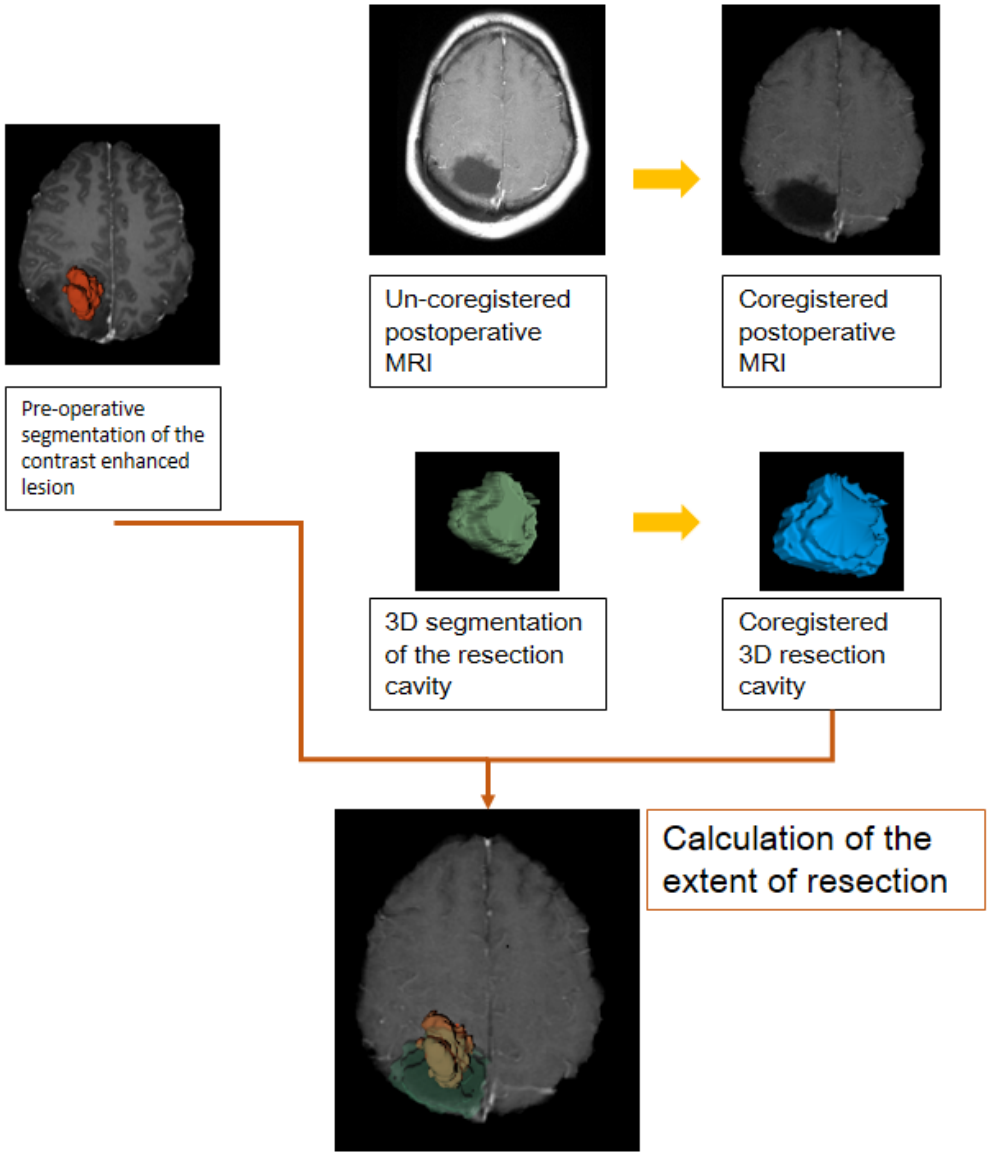

Figure 5.1 Workflow of the Imaging Processing

The segmentation of the pre-operative images was done separately based on different MR techniques. After creation of the individual masks of the lesion, the post-operative MRI was coregistered to the pre-operative MRI by using the two stage non-linear semi-automatic coregistration method. The resulted transformation was further applied to the post-operative 3D mask (green) to calculate the coregistered resection mask (blue). This can further overlap with the pre-operative lesion mask (red) to calculate the extent of resection.

Tumour Volume and Extent of Resection Data Analysis

Extent of resection was determined from the resection cavity in the coregistered, postsurgical, postcontrast T1-weighted image (Fig. 5.2, blue outline) by one of the authors (Jiun-Lin Yan) blinded to the outcome, with the agreement of a second author (Anouk van der Hoorn, radiologist, Department of Radiology, University Medical Centre Groningen, University of Groningen, The Netherlands). The 3D, peritumoural, abnormal

FLAIR, p, and q regions of interest were manually selected on the coregistered presurgical MR images (Fig. 5.2 B-D). The inter-observer correlation was done by the first author (J.L.Y.) and senior author (S.J.P.) with fair agreement (Chapter 3.2.8). The coregistered resected region was extracted from the total abnormal presurgical region for each sequence, using Matlab (MathWorks Inc.). Detailed function was described as below. The resected volumes were calculated for the p, q, and FLAIR regions by multiplying all voxels of interests with the slice thickness in Matlab.

Matlab function for the volume calculation

1. Calculate lesion volume (based on contrast enhancement, p, q and FLAIR)

```
mask_lesion=load_untouch_nii('lesion_mask.nii.gz'); %load lesion mask
roi_lesion=logical(mask_lesion.img); % make it logical
% volume calculation
vv=mask_lesion.hdr.dime.pixdim(2)*mask_lesion.hdr.dime.pixdim(3)*mask_le
sion.hdr.dime.pixdim(4);
vol_lesion=sum(mask_lesion.img(:))*vv/1000;
```

2. Calculate resection volume (based on post-operative contrast enhanced T1 MRI)

```
mask_resect=load_untouch_nii('resection_mask.nii.gz'); %load resect mask
roi_resect =logical(mask_resect.img); % make it logical
% volume calculation
vv=mask_resect.hdr.dime.pixdim(2)*mask_resect.hdr.dime.pixdim(3)*mask_re
```

```
sect.hdr.dime.pixdim(4);
vol_resect=sum(mask_resect.img(:))*vv/1000;
```

3. Extent of resection (EOR)

$$EOR = \frac{(\text{resection volume}) \cap (\text{preoperative lesion volume})}{\text{preoperative lesion volume}}$$

```
Roi_EOR=combineroi(roi_lesion,roi_resect,'intersection');
vol_EOR=sum(roi_EOR(:))*vv/1000;
EOR= vol_EOR/vol_lesion
```

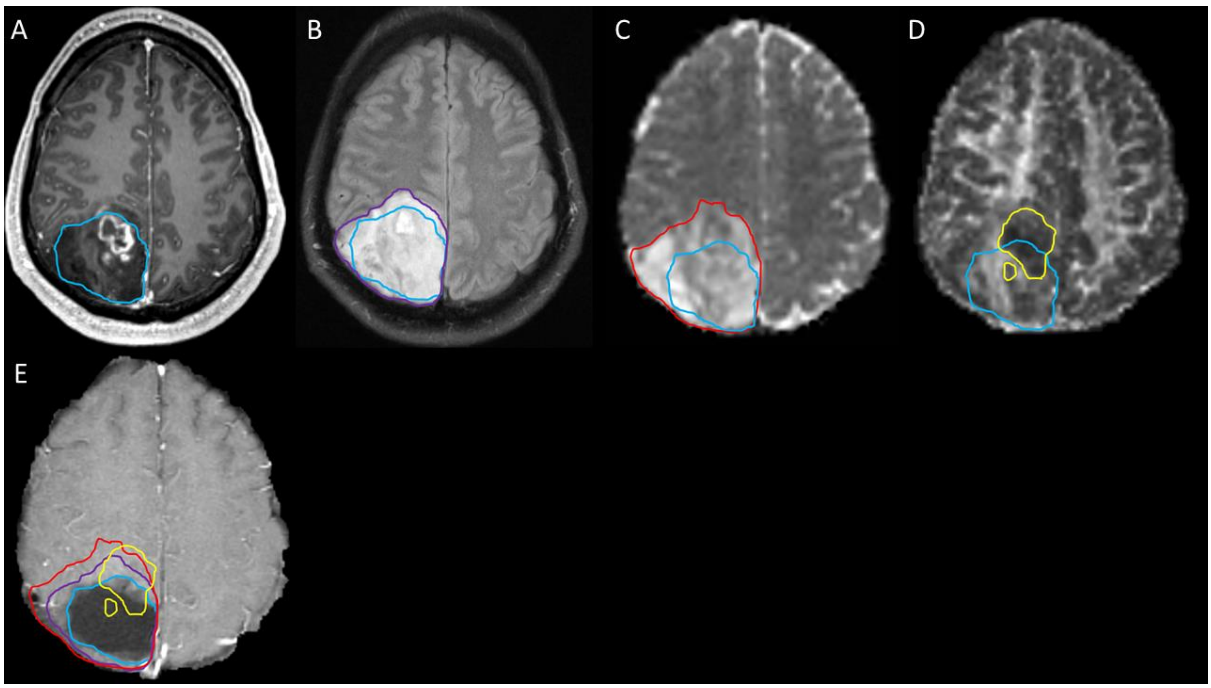

Figure 5.1 Regions of interest and EOR

Presurgical postcontrast T1-weighted image (A), FLAIR (B), and diffusion tensor images (C and D) are shown with the resected area contoured in *blue* in a representative patient. The abnormal FLAIR region (B, *purple*), the isotropic abnormality (C, *red*) and the anisotropic abnormality (C, *yellow*) are outlined. E: Summary of the regions of interest in a postsurgical contrast-enhanced T1-weighted image.

5.3 Results

5.3.1 Patients' Characteristics

Patients' clinical characteristics are shown in Table 5.1. Complete resection based on postcontrast T1-weighted imaging was achieved in 24 patients (77% of 31 patients). Ten patients had the tumour located within an eloquent area, which included the primary motor or sensory cortex, speech center, internal capsule, and basal ganglia. Ten patients had tumour located in a near-eloquent area, which included the supplementary motor area, corpus callosum, and proximity to the calcarine fissure and the speech center. The mean midline shift was 3.3 mm (± 3.7 mm; range 0-11.9 mm). The mean presurgical, contrast enhanced tumour volume was 46 ml (± 30 ml; range 8-119 ml).

The volume of the resection area was 53 ml (± 31 ml; range 10 - 131 ml), which was significantly larger than the presurgical tumour ($p = 0.001$). A total of 57% of the abnormal p area, 83% of the abnormal q area, and 59% of the increased FLAIR signal area was resected. Residual tumour volume based on p, q, FLAIR, and postcontrast T1-weighted images was 38.4 ml (± 30.2 ml; range 4.4-129.4 ml), 8 ml (± 9.7 ml; range 0-36 ml), 40.7 ml (± 32.7 ml; range 0.4-127.9 ml), and 2.7 ml (± 6.8 ml; range 0-26.6 ml), respectively. None of the patients had a major postsurgical neurological deficit or Karnofsky Performance Scale score of less than 70, which was our condition to undergo temozolomide chemoradiotherapy.

TABLE 5.1 Patient characteristics

Characteristic	Value
Total no of patients	31
Male	19
Female	12
Age, yrs	56 ± 11
Tumour location, no.	
Eloquent	10
Near eloquent	12
Non eloquent	9
Midline shift (mm)	3.3 ± 3.7
Presurgical tumour size, by imaging type, ml	
T1 contras enhanced	46 ± 30
FLAIR	84 ± 44
Isotropic (p) DTI	83 ± 44
Isotropic (q) DTI	51 ± 23
Extent of resection, by imaging type, %	
T1 post contrast	136 ± 71
FLAIR	58 ± 21
Isotropic (p) DTI	57 ± 18
Isotropic (q) DTI	83 ± 20
Residual tumour size, by imaging type, ml	
Postcontrast T1-weighted image	2.7 ± 6.7
FLAIR	41 ± 32
Isotropic (p) DTI	38 ± 30
Isotropic (q) DTI	8 ± 9.6
GTR,* no. of patients	24
STR,* no. of patients	7
IDH-1 positive, no. of patients	3
MGMT methylation positive, no. of patients	10
Progression free survival, days	367 ± 263
Overall survival, days	559 ± 292

Data are given as mean ± SD unless otherwise indicated. DTI = diffusion tensor imaging; FLAIR = fluid attenuated inversion recovery; GTR = gross total resection; IDH-1 = isocitrate dehydrogenase-1; MGMT = O6-methylguanine-DNA-methyltransferase; STR = subtotal resection.

*Based on contrast-enhanced T1-weighted image

5.3.2 EOR and Patient Outcome

Univariate Cox regression models for each variable showed a significant correlation of progression-free survival with the EOR of the p area (p = 0.030), complete resection of the contrast-enhanced lesion (p = 0.004), and MGMT methylation status (p = 0.041). Multivariate analysis was used to test the EOR with other covariates (Table 5.2). The results showed that resection of the more abnormal p was a protective predictor of tumour progression (HR 0.911; p = 0.009). The EOR of abnormal q areas was also significantly correlated with progression-free survival in the multivariate analysis (HR 0.935; p = 0.006). The EOR based on FLAIR showed no association with progression free survival in either univariate or multivariate analysis (p = 0.994 and p = 0.799, respectively). The presence of MGMT methylation was found to be a significant predictor of progression-free survival in the multivariate models for p (HR 4.626; p = 0.009), q (HR 6.716; p = 0.006), and FLAIR (HR 95.941; p = 0.001).

TABLE 2. Extent of resection and patients' outcome

EOR	Progression-Free Survival			Overall Survival		
by Imaging Type	*p* Value	HR	95% CI	*p* Value	HR	95% CI
p	0.009*	0.911	0.850–0.977	0.795	0.993	0.940–1.049
q	0.006*	0.935	0.891–0.980	0.041*	0.965	0.934–0.999
FLAIR	0.799	0.997	0.926–1.061	0.052	1.062	1.999–1.129
T1C	0.094	6.499	0.727–58.069	0.050*	9.946	1.005–98.464

Multivariate analysis results showing age, MGMT methylation status, IDH-1 mutation status, presurgical tumour volume based on post contrast T1-weighted, midline shift, and tumour eloquent location as covariates. EOR = extent of resection; HR = hazard ratio; p = isotropic component; q = anisotropic component; T1C = postcontrast T1-weighted imaging. *Statistically significant.

For overall survival, multivariate analysis was performed after controlling for age, MGMT methylation status, IDH-1 mutation status, presurgical tumour volume, tumour eloquence, and midline shift. Both the EOR based on the q map and the EOR based on postcontrast T1-weighted images were identified as predictors for overall survival (HR 0.965, p = 0.041; HR 9.946, p = 0.050, respectively). The MGMT methylation status was significantly associated with overall survival in the multivariate models for p map (HR 3.737; p = 0.043), q map (HR 4.932; p = 0.012), and FLAIR (HR 10.274; p = 0.009) images. Presurgical tumour volume based on postcontrast T1-weighted images was found to be a covariate associated with increased hazard ratio relative to EOR of the q abnormality (HR 1.039; p = 0.024) and on the enhanced area of the postcontrast T1-weighted image (HR 1.037; p = 0.040).

Previous results indicated the importance of the EOR, especially q abnormality, on outcome; therefore, we explored this in more detail. Classifying patients into 2 groups by using the median of the extent of abnormal q resection resulted in a resection cutoff of 89% of the q abnormality. Patients with a resection of greater than 89% of the q abnormality had a significantly longer progression-free survival (mean 421 ± 311 days) than those with a resection of less than 89% of the abnormality (257 ± 214 days; p = 0.034) and better overall survival (621.9 ± 389.0 days vs 518.13 ± 264.7 days; p = 0.011) (Fig. 5.3). There was no statistical difference between these 2 subgroups in age, sex, tumour location, number of patients receiving a gross total resection, or MGMT methylation or IDH-1 mutation status (Table 5.3). Similar results were seen when subgrouping patients with the median extent of p resection: Longer progression-free survival was shown in patients with greater than 60% resection of the p abnormal area (421 ± 311 vs 258 ± 176; p = 0.046).

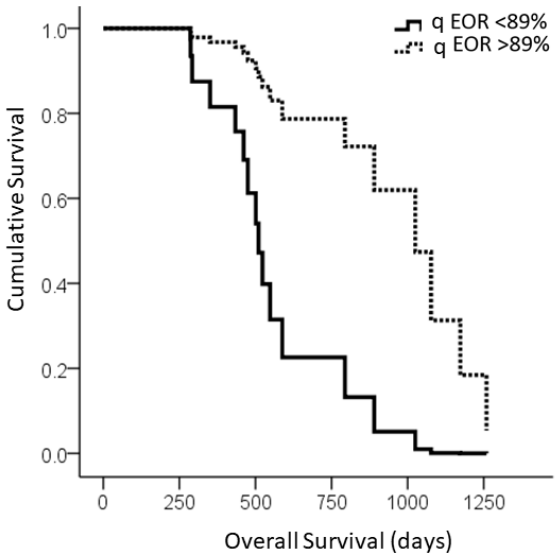

Figure 5.3 Patient overall survival according to abnormal q resection ratio

Cox regression survival analysis showed that patients with a resection of greater than 89% of the q abnormality had a better overall survival than patients with less than 89% resection (p = 0.011).

In our study, 26 patients (83.9%) had tumour recurrence within 2 cm adjacent to the resection cavity. Three patients (9.7%) had distal recurrence more than 2 cm from the original resection cavity, and 2 had recurrence both locally and distally. All patients with solely distal recurrence received complete resection of the enhanced lesion shown on the postcontrast T1-weighted image and a greater EOR of the q abnormal area (97.7%) than the others (87.4%), and 2 were MGMT methylated. Progression-free survival (721 ± 270 days) and overall survival (954 ± 461 days) were also longer in patients with distal recurrence.

TABLE 5.3 Patient characteristics for the subgroups of q resection area

Characteristic	q EOR <89%	q EOR >89%	*p* Value*
M	9	10	1
F	6	6	
Age, yrs	53.67 ± 13.16	58.68 ± 8.8	0.4168
Tumour location, no.			0.1298
Eloquent	5	5	
Near eloquent	8	4	
Noneloquent	2	7	
Midline shift, mm	3.33 ± 3.90	3.65 ± 3.63	0.8138
Presurgical tumour size, by imaging type, ml			
Postcontrast T1-weighted image	35.9 ± 18.4	53.3 ± 30.6	0.0682
FLAIR	81.1 ± 37.8	95.8 ± 52.2	0.3888
Isotropic (p) DTI	80.1 ± 38.1	90.9 ± 48.2	0.4948
Anisotropic (q) DTI	48.8 ± 14.3	54.5 ± 30.8	0.5147
GTR†, no. of patients	9	15	0.0693
STR†, no. of patients	6	1	
IDH-1 positive, no. of patients	2	1	0.5050
MGMT methylation positive, no. of patients	5	5	0.9013
Progression-free survival‡, days	257 ± 214	421 ± 311	0.034*
Overall survival‡, days	518.13 ± 264.7	621.9± 389.0	0.011*

Data given as mean ± SD unless otherwise indicated.

*Statistically significant.

†Based on contrast

‡Analyzed by multivariate Cox regression model.

5.3.3 Residual Tumour Volume and Patient Outcome

The correlations of patients' outcome and residual tumour volume based on different MR images are summarized in Table 4. A larger residual volume on DTI was associated with a decrease in progression-free survival, which was statistically significant for the q abnormality (HR 1.118; p = 0.008), while residual volume of the p abnormality was not significant (HR 1.28; p = 0.074). Residual FLAIR volume was not correlated with progression-free survival. Overall survival was not influenced by the residual abnormal p, q, or contrast-enhanced lesion volumes. Residual FLAIR volume decreased the hazard ratio of overall survival (HR 0.942; p = 0.008).

TABLE 5.4 Residual tumour volume and patients' outcome

Residual Tumour Imaging	Progression-Free Survival			Overall Survival		
	p Value	HR	95% CI	*p* Value	HR	95% CI
Postcontrast T1-weighted image	0.060	1.393	0.986–1.969	0.401	1.140	0.840–1.549
p	0.074	1.028	0.997–1.059	0.942	0.999	0.970–1.029
q	0.008*	1.118	1.029–1.215	0.080	1.053	0.994–1.116
FLAIR	0.882	1.003	0.968–1.038	0.008*	0.939	0.897–0.983

Multivariate analysis results showing age, MGMT methylation status, IDH-1 mutation status, presurgical tumour volume based on T1 contrast imaging, midline shift, and tumour eloquent location as covariates.

*Statistically significant.

5.4 Discussion and Conclusion

Discussion

In this study, we retrospectively reviewed the correlation between the EOR based on DTI and patients' outcome. Although the intention of initial resection was based on 5-ALA rather than on any DTI parameter, this study showed, via multivariate Cox regression model, a significant correlation between the EOR, based on both the p map and q map, and progression-free survival. Furthermore, a favorable overall survival was seen in patients who received greater resection of the q map and the enhanced area on postcontrast T1-weighted images. Thus, by resecting more abnormal DTI areas, most importantly the q area, the infiltrating tumour burden decreases, leading to a better outcome.

The significance of resecting more of the contrast-enhanced lesion has been shown clearly to correlate with patient survival. Sanai and colleagues showed that improved overall survival begins at a 78% resection and continues to increase as resection of the contrast-enhanced area becomes greater[119]. A non-volumetric study of high-grade glioma has also shown a longer overall survival associated with complete resection rather than with incomplete resection (16.7 vs 11.8 months, respectively; $p < 0.001$)[136]. Others have reported the synergistic clinical benefit of the EOR and concomitant chemoradiotherapy[134]. Moreover, the benefit of reduced tumour burden is related to the efficacy of 1,3- bis (2-chloroethyl)-1-nitrosourea (BCNU): In one study, a lower concentration was needed to achieve 90% growth inhibition in low-tumour-burden groups[88]. In patients receiving BCNU wafers during surgery, longer median survival has been noted in the complete-resection group compared with those in the subtotal-resection group[137]. Therefore, reduction of contrast-enhancing tumour burden is an important prognostic factor for patient outcome.

To date, most studies have defined EOR using the contrast enhanced area only; however, a false-negative rate of 16% was found in normal-appearing areas on T1-weighted images[105], and tumour cells often extend beyond the contrast-enhanced area. We have shown previously that specific DTI signatures can predict this microscopic tumour invasion[105,111]. In particular, regions with greater than a 10% increase of p signified white matter infiltration by tumour, whereas regions with greater than a 12% decrease in q showed white matter disruption by cancer. Therefore, using DTI can better delineate the actual tumour margin and show the invasive area of tumour. Although we did not perform a histological correlation in this study, previous research has validated a correlation between DTI and viable tumour cells[29].

A previously conducted tumour-resection treatment-bias study showed that complete resection was more often achieved in younger patients and in those with tumours in non-eloquent tumour locations[136]. We tested our result by using a median q-abnormality EOR of 89% as the cutoff to stratify patients into 2 groups. In these groups, a longer progression-free survival was seen in those with a greater than 89% q-abnormality resection, but other variables, including age, tumour eloquence, MGMT methylation status, IDH mutation, midline shift, presurgical tumour size, and complete resection of the enhanced lesion on postcontrast T1-weighted images, were all comparable (Table 5.3). A bias, therefore, could not be identified, which strengthens our results, indicating the importance of the EOR based on DTI.

Specifically looking at the patients with distal recurrence, a previous study showed a correlation between extended resection and recurrence pattern, with a better prognosis in those with distal recurrence[23]. In our study, all 3 patients with distal recurrence received a greater EOR of the DTI-detected abnormality (EOR of q abnormality > 97%) beyond the contrast-enhanced area. Although the number in our

study is small, this finding may indicate that distal recurrence occurs in those with a better local control based on DTI and consequently resulted in a better prognosis.

We also examined the residual tumour volume based on different MR sequences. More abnormal q volume left after surgery can significantly increase the risk of progression and marginally decrease overall survival. Grabowski and colleagues showed that residual contrast-enhanced lesion volume of more than 2 cm^3 after surgical resection was a strong, unfavorable predictor of overall survival[39]. Furthermore, others also concluded that a residual contrast-enhanced tumour volume of less than 10 cm^3 can lead to both prolonged time to progression and survival[65]. In our results, only marginal significance in progression-free survival was noted based on postcontrast T1-weighted imaging. This may be due to the limited numbers of patients in our study. Regardless of the limited numbers, we clearly displayed the advantage of the q map, which, according to a previous biopsy studies, represents regions of tumour cells[105]. Thus, a smaller residual abnormality in the q region indicated a lower tumour load and a better prognosis.

Conclusion

The expanding application of DTI in patients with brain tumours can demonstrate not only possible tumour invasion but also can provide a guide for surgeons. Our results underscore the importance of abnormal DTI area, especially of abnormal q area, showing that patients who received larger EOR and who had less residual abnormal DTI had better progression-free survival and overall survival. Further prospective studies are needed to clarify the clinical benefit of incorporating DTI into surgical planning.

CHAPTER 6

Characterizing Tissue Anisotropy of the Peri-tumoural Region in Glioblastoma Using Diffusion Tensor Imaging

6.1 Introduction

The malignancy of the GBM has been discussed in Chapter 1.1 and 1.2. Its poor prognosis may be due in part to our inability to detect the full extent of the tumour margin using standard structural MRI. Therefore, it is important to use advanced MR techniques in the detection of GBM (Chapter 1.3), especially DTI. The diffusion tensor can be decomposed into isotropic component (p) and anisotropic component (q)[100], which can be used to identify whether the peritumoural white matter is infiltrated, displaced or disrupted by the glioblastoma. A recent study focused on the peritumoural p map had shown an increase in tumour metabolic activity and regional perfusion in the tumour margin[113]. On the other hand, an abnormal q can represent GBM gross tumour[105]. The area of the abnormal q is different, sometimes larger than the contrast enhancing compartment (Chapter 5, 46 ± 30ml vs 51± 23ml, p = 0.0004). Assessing the extent of resection based on DTI has shown that a larger volume of resection of the DTI, especially the abnormal q areas, was shown to prolong progression free survival and overall survival[166] (Chapter 5) due to a better local control. This drives the intention to understand more about the peritumoural area with abnormal DTI q.

Multi-voxel proton MR spectroscopy (^{1}H-MRS) can detect and quantify specific molecule compound by using electron screening and chemical shift in certain regions of interest in the brain[63] (a more detailed discussion was presented in Chapter 1.3.4.). In gliomas, the Choline (Cho)/ N-acetyl aspartate (NAA) index is an important marker of cellular proliferation[78]. Studies have shown that distinct differences exist in the peritumoural ^{1}H-MRS characteristics that can differentiate GBM from the non-invasive meningioma[163]. Dynamic susceptibility perfusion MR (DSC-MRI), another valuable MR technique, can be used to measure the relative cerebral blood volume (rCBV) a measure of tumour vascularity[142], angiogenesis[4] and tumour cellularity[110] (also see Chapter 1.3.3).

Therefore, in this chapter, our aim is to analyze the peritumoural tissue characteristics beyond the contrast enhancing compartment by using ^{1}H-MRS and DSC-MRI. Utilizing the DTI anisotropic q abnormality map, peritumoural DTI-defined invasive regions of interest were compared to other peritumoural areas with normal DTI which can further provide a better understanding of the GBM local invasive environment.

6.2 Method

Patient inclusion criteria were discussed in Chapter 3.1. Detailed inclusion patient list was shown in Appendix A. Patients with complete pre-operative diagnostic MRI and clinical data were included.

MRI parameter and Imaging processing were as described in Chapter 3.2. All patients received standardized preoperative 3D volumetric T1 weight with contrast enhancement (MPRAGE), T1 weighted without contrast, T2 weighted, FLAIR, DTI, DWI, MRS and DSC-MRI within one week before surgical intervention.

6.2.1 Regions of Interest and DTI pattern

The peritumoural abnormal q ROIs were calculated by subtracting the contrast enhanced ROIs from the abnormal q areas in Matlab (MathWorks Inc., Natick, MA, USA). The abnormal q map were drawn manually by a neurosurgeon (JLY) by using 3D slicer (http://www.slicer.org/).[33] Previous studies have shown fair inter- and intra-rater agreement (Dice score: 0.68 ± 0.08 in the q ROIs, Chapter 3.2.8). Contrast enhancing compartment ROIs were drawn semi-automatically by threshold selection and manually correction by using 3D slicer.

Four regions of interest were compared for characterizing the peritumoural areas outside of the contrast enhancing compartments (Figure 6.1).

1. The peritumoural abnormal q ROIs;
2. The peritumoural ROIs without q abnormality;
3. The contrast enhancing ROIs (CE, excluding the central necrotic part);
4. The contralateral normal appearing white matter (NAWM).

In addition, our previous study had shown that areas of abnormal q are generally larger than the contrast enhancing compartment (Chapter 5)[166]. Therefore, patients were classified into two groups according to the pattern of q abnormality: Patients who had the q abnormal area larger than contrast enhancing area and those had the q abnormal area equal or smaller than the contrast enhancing areas.

6.2.2 ^{1}H-MRS data acquisition

Tissue characteristics including total N-acetyl-aspartate (NAA), myo-inositol (Ins), total choline (Cho) including phosphocholine (PCh) and glycerylphosphorylcholine (GPC), glutamate (Glu) and glutamine (Gln), and glutathione (GSH) were all calculated as a ratio to the total creatinine for each spectroscopy voxel. Choline/NAA ratio was also calculated. Due to a bigger size of MRS voxel (1x 1 x 2 cm) than structure MRI and DTI, ROIs data were included only if it occupied more than 50% of the MRS voxel. The selection of the corresponding MRS voxel was done in two approaches.

1. Visually selection of the voxels that were occupied by the ROIs for more than 1/2 of the voxel size.
2. A 3 dimensional voxel-wise approach with an in-house program in R (R Development Core Team, 2008) (Figure 6.2). By using the 3D voxel wise approach, multiple slices of the MRS data could be obtained from different ROIs (Figure 6.2 blue voxels). This can provide an objective method for the voxel selection. The program is developed together by two members of the lab Dr. Timothy J Larkin and Dr. Daniel M Fountain (Cambridge Brain Tumour Imaging Laboratory, Cambridge, UK) and further modified to fit the study (Figure 6.3). Detailed script for the method will be shown in Appendix F.

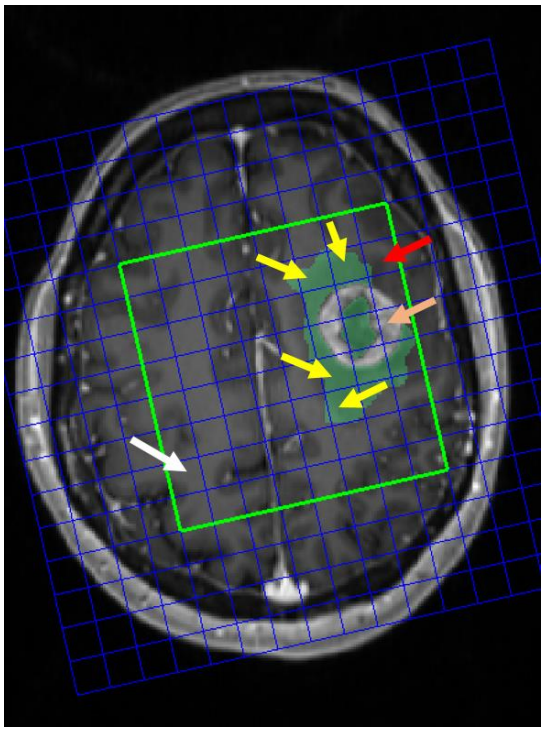

Figure 6.1 Illustration for different ROIs

Four regions of interests (ROIs) are indicated for imaging characteristics comparison. The yellow arrows indicates the peritumoural abnormal q ROIs; red arrow indicates the peritumoural ROIs without q abnormality; orange arrow indicates the contrast-enhancing compartment; white arrow indicates the contralateral normal appearing white matter.

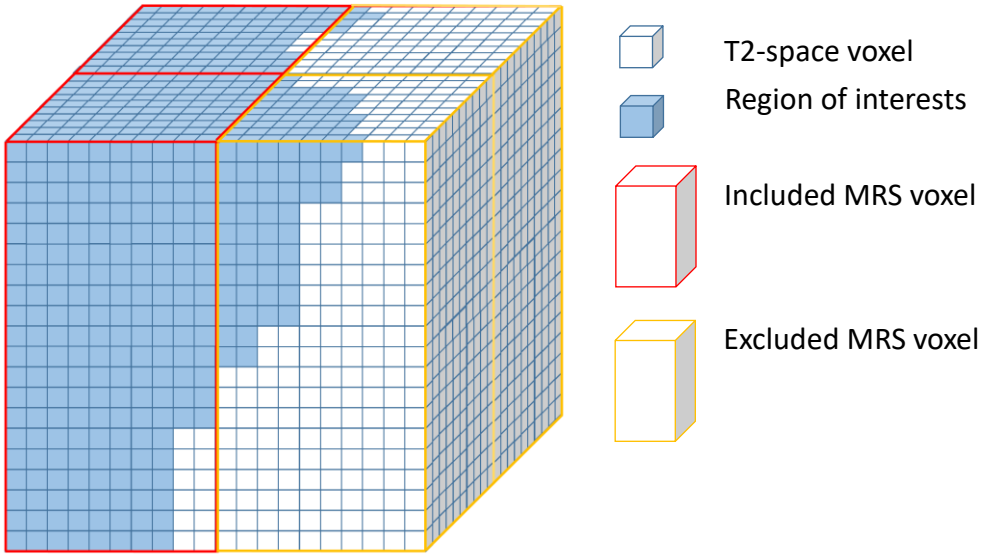

Figure 6.2 3D voxel-wise method for MRS data retrieve

This figure illustrates the 3D voxel-wise method for MRS data retrieve. White cubes represent T2-space voxel (1 x 1 x 1 mm), and the blue cubes represent regions of interest. MRS data would be included if regions of interest occupy more than 1/2 of the MRS voxel (red outline), else it would be excluded (yellow outline).

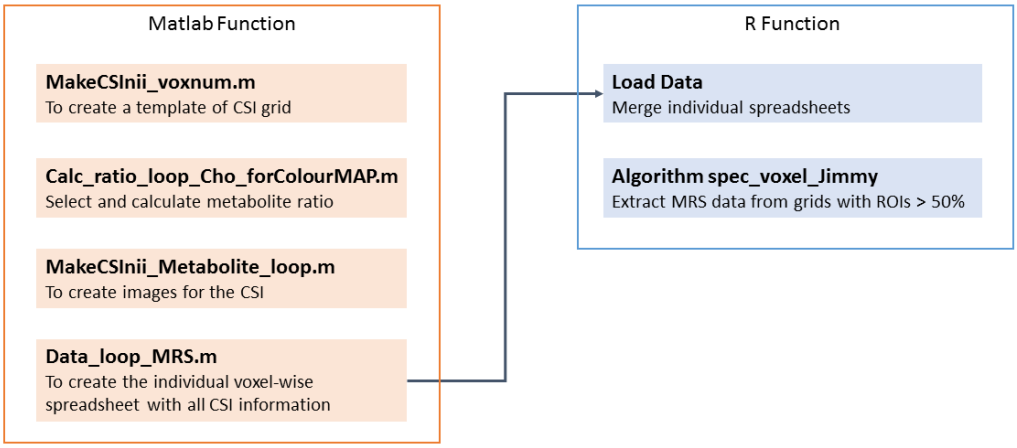

Figure 6.3 Workflow for the 3D voxel-wise approach for MRS data acquisition

Matlab functions (orange) were proceeded firstly to extract all MRS information and imaging information (for example, voxel position coordinates). Then by using R function (blue), can test if the MRS grids have ROIs for more than 50% to obtain the needed MRS metabolite data. CSI: chemical shift imaging; ROI: regions of interest

Statistics

Data were analyzed by using SPSS version 22 (IBM Inc.). MRS data and rCBV between different ROI groups were compared by using one-way ANOVA test. Pair *t*-test was used to compares imaging data between the peritumoural abnormal q ROIs and the peritumoural ROIs without q abnormality. Comparison of patient's clinical characteristics between different patterns of q abnormality, including age, gender, percentage of the total resection of the contrast enhancing tumour, use of gliadel wafer, Isocitrate dehydrogenase-1 (IDH-1) mutation status, O^6-methylguanine-DNA methyltransferase (MGMT) methylation status, were calculated by pair *t*-test for continuous data and by chi-square with Fisher's exact for small-number categorical data. Overall survival and progression free survival between different groups were calculated by Kaplan Meier with log-rank test. The statistical significance was defined by two-sided p-value < 0.05.

6.3 Results

51 patients (mean age 60.2 years, range 36.7 - 73.8) were included in this study. There were 13 female and 38 male. The complete resection based on contrast enhanced T1 weighted MRI were achieved in 76.3% of the patients. IDH-1 mutation status was obtained in 40 patients, and 2 were mutated type. MGMT promoter methylation status was available in 41 patients with 21 methylated. The median overall survival was 330 days ± 288.8 days (median ± SD), and the progression free survival was 194 ± 179.5 days (median ± SD).

Number of patients with available MRS spectra data retrieved by different methods in different ROIs were shown in Table 6.1. In the contrast enhancing ROIs, different substance MRS data were included in 32 to 49 patients. In peritumoural abnormal q ROIs, available MRS data were obtained from 22 to 29 patients. And 42 to 49 patients were included in the peritumoural ROIs without q abnormality for different substances. The unavailable data were mostly due to high standard deviation (>20%) of the normalized voxel MRS data, and the size of the ROIs that were smaller than 50% of the MRS voxel.

Volume of the peritumoural abnormal q ROIs in all patients was 48.69 ± 30.34 ml (mean ± SD), and the volume of contrast enhancing ROIs was 39.55 ± 28.02 ml (mean ± SD). 25 out of 51 patients had the q abnormality area greater than the contrast enhancing area for at least ½ of the MRS voxel (60.9 ± 34.8 ml versus 40.0 ± 34.6 ml), while 26 out of 51 patients had q abnormality area equally or smaller than the enhancing area (37.5 ± 21.4 ml versus 39.2 ± 21.8 ml).

Table 6.1 Number of patients with available MRS data of different substances

	Peritumoural abnormal q ROIs		Peritumoural ROIs without q abnormality		CE		NAWM	
	Voxel-wise	Visual	Voxel-wise	Visual	Voxel-wise	Visual	Voxel-wise	Visual
Cho/Cr	25	27	45	27	43	49	43	47
NAA/Cr	25	25	45	48	43	36	43	46
Cho/NAA	25	24	45	48	43	38	43	46
Ins/Cr	23	26	45	49	43	46	43	47
Glu+Gln /Cr	29	22	45	42	43	32	36	40

CE: contrast enhanced ROIs

NAWM: contra-lateral normal appearing white mater

Voxel-wise: 3D voxel-wise approach for MRS data acquisition

Visual: visually inspection for the selection of corresponding MRS data

6.3.1 ^{1}H-MRS tissue characteristics using 3D voxel-wise method

Using 3D voxel-wise approach for ^{1}H-MRS data retrieve, Cho/Cr were different in all four ROIs ($p < 0.0001$, Figure 6.4A), highest in the contrast enhancing ROIs, followed by peritumoural abnormal q ROIs, peritumoural ROIs without q abnormality and the contralateral NAWM. Subgroup analysis showed higher Cho/Cr in the peritumoural abnormal q ROIs than ROIs without q abnormality ($p = 0.0219$). Total NAA/Cr showed increase in the contrast enhancing ROIs ($p < 0.0001$, Figure 6.4B), but no significant difference between peritumoural abnormal q ROIs and ROIs without q abnormality ($p = 0.3532$). Significant elevation of Cho/NAA ratio was noted in the contrast enhancing ROIs ($p < 0.0001$, Figure 6.4C). In the peritumoural abnormal q ROIs also showed increase in Cho/NAA ratio, compared to the ROIs without q abnormality ($p= 0.0346$) and contralateral NAWM ($p = 0.0021$). The Glu/Cr was found to be higher over the contrast enhancing ROIs and peritumoural abnormal q ROIs than the contralateral NAWM ($p < 0.0001$, $p = 0.0158$, Figure 6.4D). Glu/Cr of the ROIs without q abnormality

had no statistical significant difference to the peritumoural abnormal q ROIs (p = 0.6981) and contralateral NAWM (p= 0.0682). In addition, there is a significant decrease in Ins/Cr in peritumoural abnormal q ROIs, compared to contrast enhancing ROIs and contralateral NAWM (p < 0.0001, p = 0.0011, Figure 6.4E).

Relative CBV were higher in contrast enhancing ROIs and all peritumoural area than the contralateral NAWM (p< 0.0001). Subgroup analysis showed marginal increase of rCBV in peritumoural abnormal q ROIs than the peritumoural ROIs without q abnormality (p = 0.0798, Figure 6.4F).

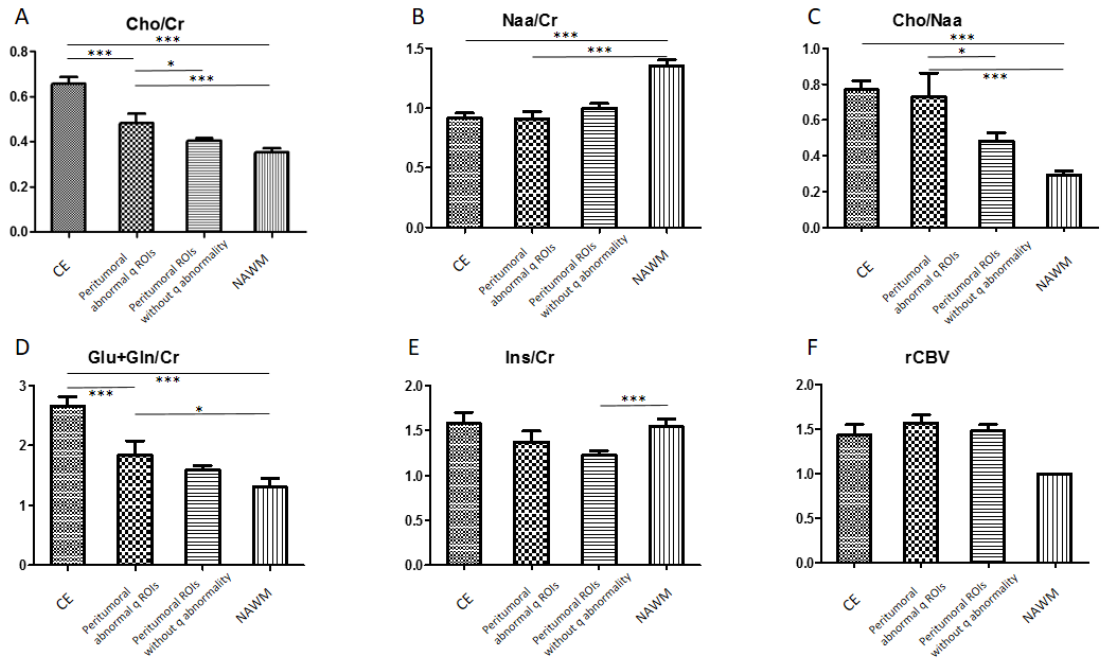

Figure 6.4 MRS characteristics between different ROIs

The MRS data of different chemical compounds (A-E) and rCBV (F) between different regions of interest (ROIs). Comparison between the ROIs within contrast enhancing compartment (CE), the peritumoural q abnormal ROIs, the peritumoural normal q ROIs and the contralateral normal appearing white matter (NAWM). Note that in the peritumoural q abnormal ROIs have higher Cho/Naa and higher Cho/Cr than the peritumoural normal q ROIs.

Important significant difference are marked the lines and stars. *: p < 0.05; **: p< 0.01; ***: p < 0.001

6.3.2 MRS data retrieve by using different method

Comparing visual inspection and 3D voxel-wise method for MRS data retrieve, no significant difference of the data value was noted between two methods (Table 6.2). In all four ROIs, there were comparable value of the Cho/Cr, NAA+NAAG/Cr, Cho/NAA, Glu+Gln/Cr and Ins/Cr in both methods.

In comparison to the visual inspection method, using 3D voxel wise method had 2 more missing data in Cho/Cr, 3 more missing data in Ins/Cr, 1 more missing data in Glu+Gln/Cr and one less missing data in Cho/NAA. On the other hand, one more missing data was found in visual inspection method than the 3D voxel-wise method (Table 6.1).

6.3.3 Clinical Outcome of Different q Abnormality Patterns

25 patients had peritumoural abnormal q ROIs larger than the contrast enhancing ROIs and 26 patients were found with a smaller peritumoural abnormal q ROIs. The overall survival was significantly longer in patients with larger peritumoural abnormal q ROIs than those with a smaller peritumoural abnormal q ROIs (median: 405 vs 310 days, $p = 0.0103$) (Figure 6.5A). And the progression-free survival is also longer in this larger abnormal q ROIs group (median: 221 vs 164 days, $p = 0.0346$). There were no statistical difference in age, gender, total resection of the contrast enhancing compartment, use of gliadel wafer, MGMT methylation status and IDH-1 mutation status between two groups of patients (Table 6.3).

Table 6.2 Comparison of different method for MRS data retrieve

Peritumoural abnormal q	3D voxel-wise approach	Visual inspection	
ROIs	value	value	*p* value
Cho/Cr	0.486±0.042	0.442±0.021	0.37
NAA/Cr	0.913±0.059	0.946±0.061	0.70
Cho/NAA	0.731±0.131	0.639±0.149	0.64
Ins/Cr	1.373±0.121	1.207±0.064	0.22
Glu+Gln /Cr	1.842±0.237	1.772±0.138	0.40
The peritumoural ROIs	3D voxel-wise approach	Visual inspection	
without q abnormality	value	value	*p* value
Cho/Cr	0.404±0.090	0.390±0.096	0.54
NAA/Cr	1.001±0.253	1.026±0.297	0.65
Cho/NAA	0.483±0.307	0.449±0.309	0.55
Ins/Cr	1.223±0.351	1.305±0.810	0.53
Glu+Gln /Cr	1.156±0.351	1.748±0.710	0.23
	3D voxel-wise approach	Visual inspection	
CE	value	value	*p* value
Cho/Cr	0.657±0.204	0.768±0.408	0.10
NAA/Cr	0.916±0.279	0.920±0.406	0.52
Cho/NAA	0.769±0.319	0.879±0.505	0.24
Ins/Cr	1.579±0.834	1.661±0.865	0.65
Glu+Gln /Cr	2.654±1.072	3.137±2.184	0.90
	3D voxel-wise approach	Visual inspection	
NAWM	value	value	*p* value
Cho/Cr	0.353±0.106	0.355±0.102	0.95
NAA/Cr	1.356±0.302	1.356±0.356	0.95
Cho/NAA	0.293±0.149	0.288±0.146	0.90
Ins/Cr	1.542±0.584	1.520±0.560	0.93
Glu+Gln /Cr	1.307±0.833	1.341±0.792	0.26

Table 6.3 Clinical characteristics in patients with different q abnormality pattern

	q ≤ T1C	q > T1C	*p* value
Numbers	26	25	
Age (years old)	60.1 ±8.9	60.1 ± 9.0	0.98
Gender (M/F)	20/6	18/7	0.06
CRET Rate (%)	77.8	68.4	0.71
Gliadel Use (%)	52.9	73.7	0.30
IDH-1 mutation (no.)	0	2	0.22
MGMT methylation (no.)	10	11	0.76
Progression free survival (days)	164	221	0.03
Overall survival (days)	310	405	0.01

q ≤ T1C: patient group with q abnormality areas smaller or equal than contrast enhancing areas

q > T1C: patient group with q abnormality areas larger than contrast enhancing areas fore more than 1/2 of MRS voxel size.

CRET: complete resection of the contrast enhancing compartment

IDH-1: isocitrate dehydrogenase-1

MGMT: O^6-methylguanine-DNA methyltransferase

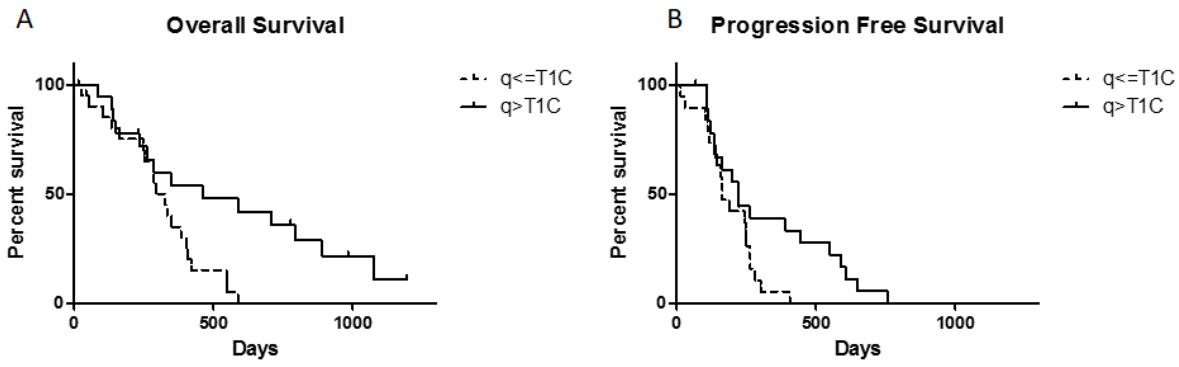

Figure 6.5 Survival difference between different q abnormality patterns

For patients with q abnormal ROIs larger than contrast enhancing area, log-rank test showed a longer overall survival than patients with smaller q abnormal ROIs (4A, median: 405 vs 310 days, p = 0.0103). Besides, progression free survival was also longer in the larger q abnormal ROIs group (4B, median: 221 vs 164 days, p = 0.0346).

q<=T1C: patients with the abnormal q ROIs smaller than contrast enhancing compartment
q > T1C: patients with the abnormal q ROIs larger than contrast enhancing compartment

Table 6.4 Summary of the Imaging Characteristics

	Cho/Cr	NAA/Cr	Cho/NAA	Glu+Gln/Cr	Ins/Cr	rCBV
CE	↑↑↑	↓↓↓	↑↑↑	↑↑↑	-	↑↑↑
Peritumoural q abnormal areas	↑↑↑	↓↓↓	↑↑	↑	-	↑↑↑
Peritumoural ROIs without q abnormality	↑	↓↓	↑	-	↓↓↓	↑↑

CE: contrast enhanced ROIs

↑ and ↓ illustrated the increase and decrease of the value. The number of the arrows showed the significance of the change. ↑↑↑/ ↓↓↓: $p < 0.001$, ↑↑/ ↓↓: $p < 0.01$, ↑/ ↓: $p < 0.05$

6.4 Discussion and Conclusion

Discussion

In our study, we found 25 patients who had the q abnormal ROIs larger than the contrast enhancing compartment. And in these peritumoural q abnormal ROIs, compared to those peritumoural ROIs without q abnormal, a significant increase in Cho/NAA, especially Cho/Cr, can be noticed by using ^{1}H-MRS (summarize in Table 6.4). Furthermore, patterns of these q abnormal ROIs can have different clinical prognostic outcome.

It is clear that GBM cells can extend beyond contrast enhancing compartment and in a previous study where this peri-tumoural region was biopsied had shown evidence of cancer cell infiltration in up to one third of patients.[70] However, conventional structural MRI sequences fail to detect this invasive margin. Many studies have attempted to use multimodal MR imaging of the peritumoural areas to differentiate GBM from less invasive metastatic brain tumours or benign brain tumours.[113] Tsougos et al. had shown an increase in Cho/Cr, rCBV and a decrease in NAA/Cr were found in the peritumoural areas of GBM compared to metastatic tumour.[149] Other studies showed an increase in Cho/Cr, Cr/NAA, and Ins/Cr[163] in GBM peritumoural areas compared to meningioma. Our results not only showed an increase cell turnover rate (increase in Cho/Cr) but also a higher Cho/NAA in the peritumoural q abnormal region, compared to peritumoural areas without q abnormality. Although NAA/Cr showed no difference between peritumoural q abnormal and q normal ROIs, NAA/Cr in all peritumoural ROIs were lower than the contralateral normal appearing white mater which is compatible with other studies.

Some studies showed inconsistent results of DTI in the peritumoural areas, in Tsougos's study there was no difference of apparent diffusion coefficiency (ADC) or fractional anisotropy (FA) between the peritumoural area and control[149], more studies have shown DTI as an imaging biomarker in the invasive tumour margin. Min et al. showed a significant higher regression coefficiency of radial diffusivity to axial diffusivity and a lower FA[79], and Wang et al. also shown a decrease in the q component of DTI in the peritumoural area. Furthermore, our previous biopsy studies also shown that gross cancer tissue can be shown in abnormal DTI especially in the q area (decrease > 12%).[105] Sternberg et al. concluded that DTI is the most effective modality to delineate the tumour invasion margin beyond the conventional MRI[132].

In our results, an increase of Glu+Gln/Cr in not only contrast enhancing compartment but also in the peritumoural q abnormal ROIs compared to the contralateral control. Glutamate is known to play an important role in tumour invasion such as the excitatory neurotoxicity to peritumoural neuron and also the extracellular matrix which facilitate the cancer cell migration.[129] Therefore, this finding supports the invasive potential in the peritumoural q abnormal ROI.

The level of the Ins/Cr was lower than control in the peritumoural ROIs especially in those area without q abnormality. Myo-inositol is known as a cerebral osmolyte and also an astrocyte marker which can be seen in various intracranial pathology.[147] The change of the Ins/Cr level is variable, Castillo et al showed an increase of Ins/Cr in low grade glioma and decrease in glioblastoma.[16] The decrease of the Ins/Cr may due to reduced reactive astrocyte with in the peritumoural abnormal q ROIs. Other causes of the decrease of myo-inositol may be seen in stroke, hepatic encephalopathy, due to the balance of osmoregulation. However, this result can be minimize after normalization by the Cr. Therefore, the decrease of myo-inositol in the peritumoural

area in our series due to marked peritumoural oedema is less likely. Another study had shown and decrease of Ins/Cr may be due to an elevation of the Ins/Cr in the contralateral normal appearing white matter that Kellenberg et al had described possible tumour infiltration in the contralateral cerebral hemisphere of the untreated GBM patients with an increase of myo-inositol[62].

Our DSC-MRI showed only marginal higher rCBV in the peritumoural abnormal q ROIs than in the peritumoural ROIs without q abnormality (p = 0.0798). However, there is a significant elevated in all peritumoural ROIs which is compatible with our previous studies[113]. An increase of rCBV is resulted from the increase tumour density followed by hypoxia then angiogenesis which is correlated to cellular proliferation in high-grade glioma.[110] Other groups have shown that the site of increased rCBV may potentially predict sites of tumour progression.[9]

Our study has shown that different patterns of abnormal q ROIs impact on clinical outcome. We have shown that there is a better overall survival and progression free survival in those with larger abnormal q ROIs than contrast enhanced areas. This was independent of age, resection type, IDH-1 mutation status and MGMT methylation status between two groups. Our previous studies showed DTI abnormality patterns can be classified into localised, minimal and diffused types and is associated with prognosis[83]. The classification was based on the relationship of p and q abnormal area but not with the contrast-enhancing area. As previously described, a higher Cho/Cr level, which represents higher cell turnover rate. And all patients in our study received standard temozolomide chemoradiotherapy after surgery. Therefore, our hypothesis is that a possible better chemo- radiosensitivity can be seen in this group of patients. Studies had shown the use of MRS for assessment of the treatment response.[51] Preul et al showed that in the chemotherapy responder, there were increase in baseline NAA,

Cr and lactate but not the baseline Cho or lipid metabolites, however the ROIs in this studies was obtained within the contrast enhancing compartment.[103] Another study of 14 patients showed that a lower baseline NAA/Cr and higher Cho/Cr in the peritumoural non-enhancing region were associated with poor outcome.[6] Our results provides a different aspect to assess the clinical outcome.

In this study, we used two different method to select ROI in MRS voxel. One of the limitation on most MRS studies was to use visual inspection by experienced expert to select the MRS voxel from the overlaying ROIs. However, as the MRS voxel is usually larger than other MRI sequences, and the shape of the GBM often grows irregularly, the 3D voxel-wise approach which the MRS data were retrieved automatically according to the different ROIs can minimize the possible error of visually inspection. Although, there was no statistical difference of the metabolites value in our results, the 3D voxel-wise approach tends to have higher standard of voxel selection, we found more missing data than visual inspection. This may indicate that the 3D voxel-wise approach automatic selection had a higher standard on the MRS voxel quality control.

Conclusion

In conclusion, a tumour invasive margin can be identify by using DTI. In the peritumoural q abnormal ROIs, there was higher Cho/NAA, especially Cho/Cr which indicates tumour activity. In addition, different patterns of the peritumoural abnormal q may have clinical implication that a larger abnormal q than contrast enhancing compartment showed a better progress free survival and overall survival.

CHAPTER 7

MR Imaging Characteristics of the Peritumoural Progression Zone

7.1 Introduction

The high local progression rate of GBM after treatment is largely due to the difficulty in identifying the invasive non-contrast enhancing margin. Studies had shown that the GBM cancer cell can extend to the non-contrast enhancing area[70,71]. Therefore, the recurrence is inevitably even in patients with a total resection of the contrast enhancing tumour and subsequent chemoradiotherapy. And the recurrence usually happens in or directly adjacent to the resection area in up to 90% of the cases[101].

However, the imaging characteristics of this peritumoural non-enhanced invasive area is still not clear. The conventional structural MRI failed to identify this area and has been addressed in Chapter 1.3.1. Further application of advanced MR techniques and radiomics (Chapter 1.3.2~1.3.5) in the diagnosis of GBM provide more understandings of the peritumoural area (Chapter 5 and 6).

Thus, in this chapter we aimed to characterize the preoperative peritumoural non-enhanced area that demonstrated to have generated tumour progression later on. And further applied these features, together with radiomics features to identify areas of GBM progression on the preoperative MRI by using the convolutional neural network.

7.2 Methods

7.2.1 Patient inclusion criteria

We retrospectively included 57 patients with a newly diagnosed cerebral glioblastoma in this study. The exclusion and inclusion criteria were described as in Chapter 3.1. All 57 patients had preoperative MRI in Cambridge University Hospital with same imaging protocol. 37 patients received follow-up MRI in Cambridge University Hospital were assigned to training group, and another 20 patients who had follow-up MRI in local hospital were assigned as external validation group. The MRI scans of the external validation group were acquired after the training results of the training group. 5 of thr 57 patients had pseudoprogression prior to true progression. General characteristics were shown in Table 7.1.

7.2.2 MRI Data Acquisition and Imaging Processing

MRI data acquisition and imaging processing were described in Chapter 3.2.

Regions of Interests

Two main regions of interest (ROIs), progression areas and non-progression areas were created in this study (Figure 7.1).

The site of tumour progression and pseudoprogression were created by coregistration of the progression contrast enhanced T1 MRI to the pre-operative diagnostic MRI. The psueodoprogression was defined by stable or regression of the contrast enhancing lesion in the follow up MRI. This was done by using a previous described two stage non-linear semi-automatic coregistration[151] (Chapter 4). In short, firstly, we calculated the transformation matrix between preoperative tumour and postsurgical resection cavity by using the linear FLIRT co-registration. Then we applied this transformation matrix to a non-linear FNIRT transformation to coregister the brain.

The non-progression area were created from the peritumoural 5, 10, 15, 20 mm excluding the progression areas. In addition, a contralateral area of normal appearing with matter (NAWM) as control representing normal brain tissue.

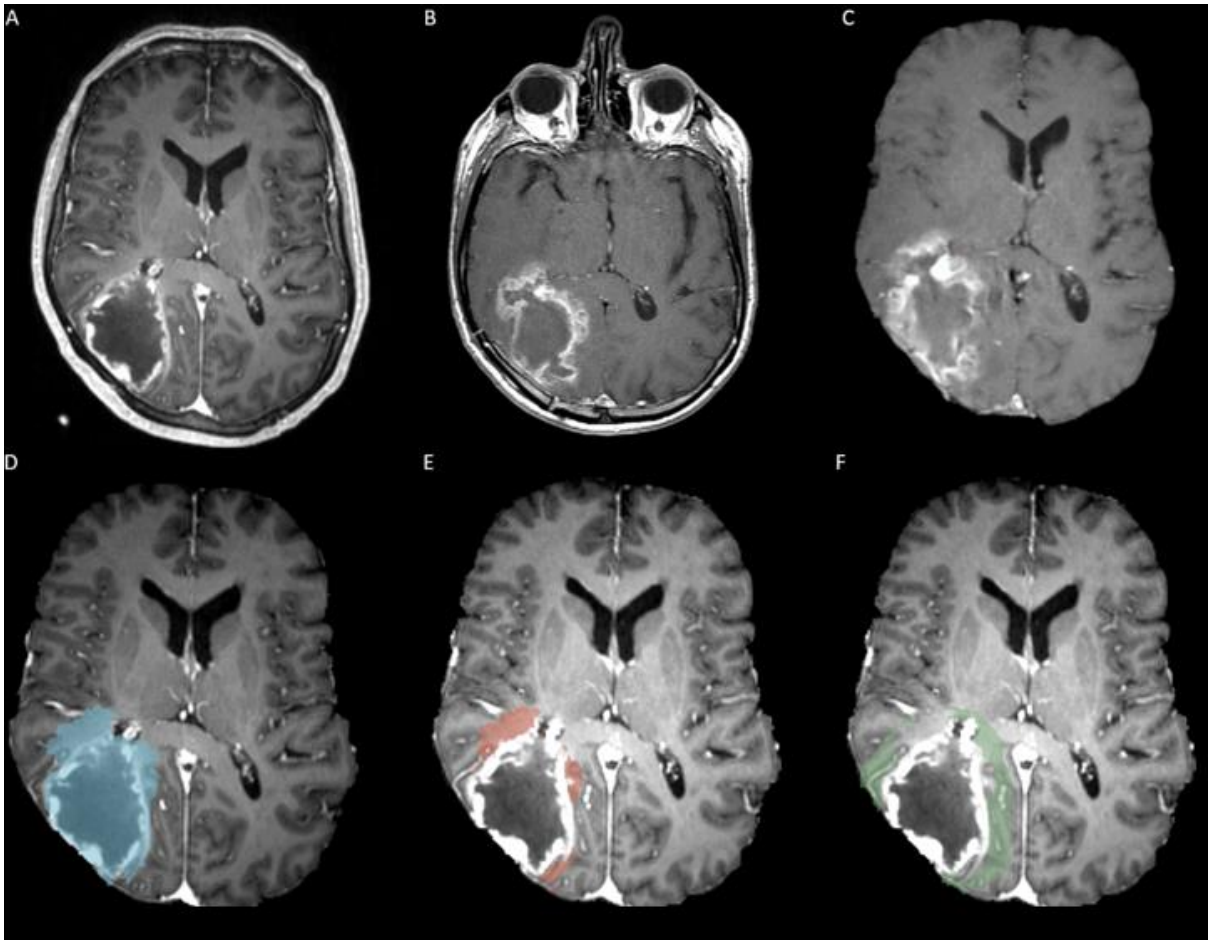

Figure 7.1

An example of tumour progression (B) was coregistered to presurgical image (A). The coregistered image (C, D blue) can further create progression area (E, red) and 10mm non-progression area (F, green).

Table 7.1 General Characteristics of the Patients

	Training Group	Validation Group	Pseudo-progression	*p*-value
Total number of patients	37	20	5	
Males/ females	24/ 13	14/ 6	4/ 1	
Age (years)	55 ± 12	60 ± 9	55 ± 9	0.29
Tumour location				0.78
Eloquent	8	4	0	
Near eloquent	14	9	3	
Non eloquent	15	7	2	
Midline shift (mm)	3.8 ± 3.8	3.3 ± 3.1	2.9 ± 3.6	0.84
Pre-OP tumour size (mL)[1]	44 ± 25	39 ± 26	40 ±14	0.76
GTR/ STR[1]	29/ 8	13/ 7	5/ 0	0.22
PFS (median, days)	262	181	778	0.01
OS (median, days)	523	407	864	0.01
MGMT un-methylated	16	4	1	0.81
methylated	10	9	3	
IDH-1 wild type	34	17	4	0.58
mutated	3	1	1	

[1] the pre-operative tumour volume and the extent of resection were evaluated based on the contrast enhanced T1-weighted MRI

GTR = gross total resection; STR = subtotal resection; PFS (progression free survival); OS = overall survival; MGMT = O^6-methylguanine DNA methyltransferase; IDH-1 = Isocitrate dehydrogenase.

7.2.3 Radiomics Analysis and Machine Learning

Scheme of the radiomics analysis was shown on Figure 7.2.

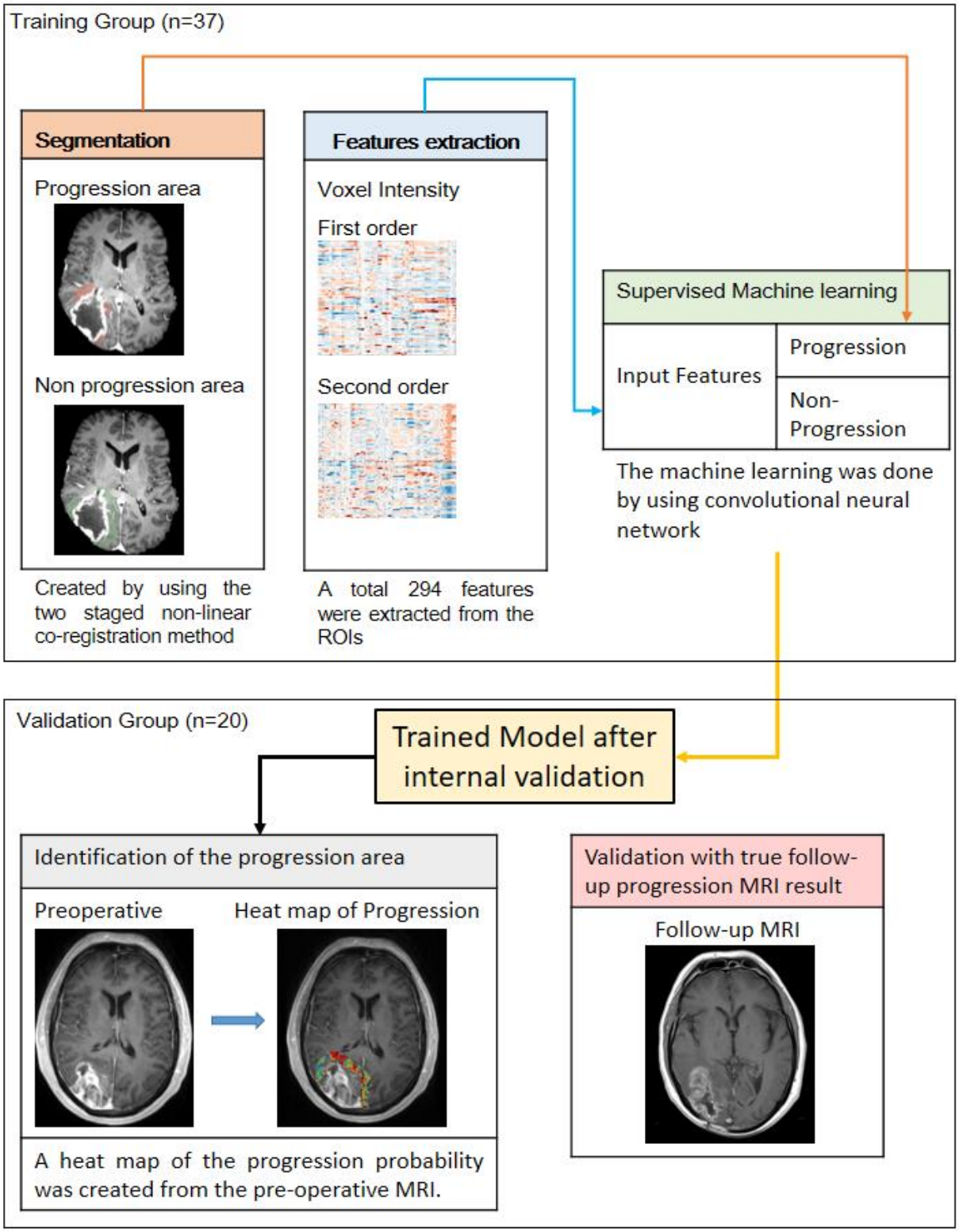

Figure 7.2 Scheme of the Radiomics Analysis

The preoperative multimodal MRI features were extracted using Matlab (MathWorks Inc., Natick, MA, USA), this includes two main components:

1. Voxel value extracted from different MR techniques, including contrast enhanced T1, FLAIR, ADC, FA, p, q and rCBV.
2. Radiomics features, including first and second order features.

Voxel value

Mean if the voxel value extracted from different ROIs (Figure 7.1) were done by using the following Matlab function.

```
% Load different MRI sequences
data=load_untouch_nii('FLAIR.nii.gz'); % use FLAIR as an example here
% Load ROI file
mask=load_untouch_nii('ROI.nii');
data1=data.img;
mask1=logical(mask.img);
pixels=data1(mask1);
FLAIR=mean(pixels); % FLAIR is the mean voxel value extracted from the ROI
```

First Order Radiomics Features

First order and second order radiomics features were extracted from 7 different MR sequences using Matlab. The MATLAB software code used to compute in the second order texture features were shared by the license under the GNU General Public License at: https://github.com/mvallieres/radiomics.

The first order features describe the grey scale level of the voxel without concern of the spatial relationship. This includes mean, standard deviation, median, minimum, maximum, variance, skewness, kurtosis, energy, entropy, uniformity, root mean square, mean gray level. Mathematics details were as following[1,98]:

$$Mean\ (\mu) = \frac{1}{n_x n_y n_z} \sum_{n=1}^{n_x n_y n_z} \left(X_{n_x}, Y_{n_y}, Z_{n_z}\right)$$

$$Standard\ deviation = \sqrt{\frac{1}{n_x n_y n_z - 1} \sum_{n=1}^{n_x n_y n_z} \left(X_{n_x} Y_{n_y} Z_{n_z} - \mu\right)^2}$$

Median: the value separate the higher half from the lower half in the total volume.

$$Minimum = \min\left(X_{n_x} Y_{n_y} Z_{n_z}\right)$$

$$Maximum = \max\left(X_{n_x} Y_{n_y} Z_{n_z}\right)$$

$$Variance\ (\sigma^2) = \frac{1}{n_x n_y n_z - 1} \sum_{n=1}^{n_x n_y n_z} \left(X_{n_x} Y_{n_y} Z_{n_z} - \mu\right)^2$$

Skewness refer to the asymmetry of the probability distribution to its mean. If the distribution is completely symmetric, the mean is equal to the median and gives us zero skewness.

$$Skweness\ (\gamma_1) = \left(\frac{\mu^3}{\sigma^3}\right) = \frac{\left(\frac{1}{n_x n_y n_z} \sum_{n=1}^{n_x n_y n_z} \left(X_{n_x}, Y_{n_y}, Z_{n_z}\right)\right)^3}{\left(\frac{1}{n_x n_y n_z - 1} \sum_{n=1}^{n_x n_y n_z} \left(X_{n_x} Y_{n_y} Z_{n_z} - \mu\right)^2\right)^3}$$

Kurtosis is another way to measure the tailedness of the distribution of the value. It shows the values are more concentrated around the mean or are more concentrated to both tails of its distribution.

$$Kurtosis\ (\gamma_2) = \left(\frac{\mu^4}{\sigma^4}\right) = \frac{\left(\frac{1}{n_x n_y n_z} \sum_{n=1}^{n_x n_y n_z} \left(X_{n_x}, Y_{n_y}, Z_{n_z}\right)\right)^4}{\left(\frac{1}{n_x n_y n_z - 1} \sum_{n=1}^{n_x n_y n_z} \left(X_{n_x} Y_{n_y} Z_{n_z} - \mu\right)^2\right)^2} - 3$$

Energy is the summation of the total voxel value in three dimension.

$$Energy = \sum_{n=1}^{n_x n_y n_z} \left(X_{n_x}, Y_{n_y}, Z_{n_z}\right)^2$$

Entropy refers to the uncertainty or non-uniformity of the voxel value. A low entropy means the voxel value of the images were organized or compacted in a certain value. In the contrast, and a higher entropy shows higher disorder. P is the first order histogram and $P(i)$is the fraction of voxles with gray level i. N_g is the number of discrete in gray level.

$$Entrophy(H) = -\sum_{n=i}^{N_g} P(i) \log_2 P(i)$$

$$Uniformity = \sum_{n=i}^{N_g} P(i)^2$$

Root mean square (RMS) is the square root of the squared mean in all voxels. Therefore it is a natural number which is not affected by the positive or negative value in each voxel.

$$RMS = \sqrt{\left(\frac{1}{n_x n_y n_z} \sum_{n=1}^{n_x n_y n_z} \left(X_{n_x}, Y_{n_y}, Z_{n_z}\right)\right)^2}$$

Mean gray level is the summation of the gray level $P(x)$ multiplied by the first order histogram fraction of voxles $P(i)$.

$$Mean\ gray\ level = \sum_{n=i}^{N_g} P(x)P(i)$$

Second Order Radiomics Features

The second order features refer to the texture analysis. The texture analysis was described firstly by Haralick et al in 1973[44]. This provides information for the description of the spatial distribution of the voxel intensities. Two main groups of features, gray level co-occurrence matrix (GLCM) and gray level run-length matrix (GLRLM), were extracted. In order to generate spatial information represents each voxel, a 5 x 5 x 5 voxel of interest (VOI) was created for each voxel (Figure 7.3).

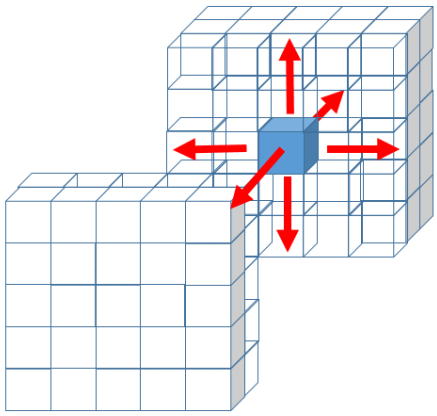

Figure 7.3

For each voxel in the ROIs (blue cubic), the adjacent 124 voxel were taken to create a 5 x 5 x 5 voxel of interest (VOI) to generate the gray level matrix for the extraction of the texture features.

Gray level co-occurrence matrix (GLCM)

The GLCM is defined as $\mathrm{P}(i, j; \delta, \alpha)$, a matrix with size N_g x N_g. This was created by calculating how often a voxel with the signal intensity value (i, grey level) occurs in a spatial relationship to a voxel with the value j with distance δ and direction α. N_g is the number of discrete intensity levels in the images. Let:

$P(i,j)$: the co-occurrence matrix

N_g: the number of discrete intensity levels in the images

μ: the mean of $P(i,j)$

μ_x: the mean of $P(i)$

μ_y : the mean of column $P(j)$

σ_x: the standard deviation of row $P(i)$

σ_y: the standard deviation of column $P(j)$

$P_x^{(i)} = \sum_{j=1}^{N_g} P(i)$: marginal row probabilities

$P_x^{(j)} = \sum_{i=1}^{N_g} P(j)$: marginal column probabilities

$$P_{x+y}(k) = \sum_{i=1}^{N_g} \sum_{j=1}^{N_g} P(i,j)\,, i+j=k, k = 2,3,4,\dots,2N_g$$

$$P_{x-y}(k) = \sum_{i=1}^{N_g} \sum_{j=1}^{N_g} P(i,j)\,, i+j=k, k = 0,1,2,\dots,N_g-1$$

$H = -\sum_{i=1}^{N_g}\sum_{j=1}^{N_g} P(i,j)\log_2 P(i,j)$: the entropy of $P(i,j)$

$Hx = -\sum_{i=1}^{N_g}\sum_{j=1}^{N_g} P_x(i)\log_2 P_x(i)$: the entropy of $P(i)$

$Hy = -\sum_{i=1}^{N_g}\sum_{j=1}^{N_g} P_y(j)\log_2 P_y(j)$: the entropy of $P(j)$

$HXY1 = -\sum_{i=1}^{N_g}\sum_{j=1}^{N_g} P(i,j)\log\big(P_x(i),P_y(j)\big)$

$HXY2 = -\sum_{i=1}^{N_g}\sum_{j=1}^{N_g} P_x(i)P_y(j)\log\big(P_x(i),P_y(j)\big)$

The GLCM calculated features were listed as following:

Auto-correlation is the measure of the coarseness of an image and the evaluation of the linear spatial relationship between texture primitives.

$$autocorrelation = -\sum_{i=1}^{N_g}\sum_{j=1}^{N_g} ijP(i,j)$$

Contrast represents the local intensity variance

$$contrast = -\sum_{i=1}^{N_g}\sum_{j=1}^{N_g}|i-j|^2 P(i,j)$$

Correlation shows the linear dependence of the intensity value between each neighborhood voxels.

$$crrelation = \sum_{i=1}^{N_g}\sum_{j=1}^{N_g}\frac{P(i,j)(i-\mu_i(i))(j-\mu_j(j))}{\sigma_x(i)\sigma_y(j)}$$

Cluster prominence and cluster chad are measures of the asymmetry of the matrix[167]. The images are asymmetric when the cluster prominence and the cluster shad are high.

$$Cluster\ prominence = \sum_{i=1}^{N_g}\sum_{j=1}^{N_g}\left[i+j-\mu_x(i)-\mu_y(j)\right]^4 P(i,j)$$

$$Cluster\ shad = \sum_{i=1}^{N_g}\sum_{j=1}^{N_g}\left[i+j-\mu_x(i)-\mu_y(j)\right]^3 P(i,j)$$

$$Dissimilarity = \sum_{i=1}^{N_g}\sum_{j=1}^{N_g}|i-j|P(i,j)$$

Energy is the measurement of the images homogeneity.

$$Energy = \sum_{i=1}^{N_g}\sum_{j=1}^{N_g}[P(i,j)]^2$$

Entropy represents the randomness of the image texture which can be used as the measurement of the inhomogeneity. A homogeneous image can have a low entropy value.

$$Entropy\ (H) = -\sum_{i=1}^{N_g}\sum_{j=1}^{N_g}P(i,j)\log_2 P(i,j)$$

$$Difference\ of\ Entropy = \sum_{i=1}^{N_g-1}P_{x+y}(i)\log_2\left[P_{x+y}(i)\right]$$

$$Sum\ of\ Entropy = -\sum_{i=2}^{2N_g}P_{x+y}(i)\log_2\left[P_{x+y}(i)\right]$$

$$Information\ measure\ of\ correlation\ 1 = \frac{H - HXY1}{max\{HX, HY\}}$$

$$Information\ measure\ of\ correlation\ 2 = \sqrt{1 - e^{-2(HXY2 - HXY)}}$$

Homogeneity is the uniformity of the voxel intensity in the matrix.

$$Homogeneity - M = \sum_{i=1}^{N_g} \sum_{j=1}^{N_g} \frac{P(i,j)}{1 + |i + j|}$$

$$Homogeneity - P = \sum_{i=1}^{N_g} \sum_{j=1}^{N_g} \frac{P(i,j)}{1 + |i + j|^2}$$

Variance (sum of square) refers to the gray level variability of the voxels. A higher variance occurs when the gray level value differs from the mean.

$$Variance = \frac{1}{N_g \times N_g} \sum_{i=1}^{N_g} \sum_{j=1}^{N_g} \left[(i - \mu_i)^2 P(i,j) + \left(j - \mu_j\right)^2 P(i,j) \right]$$

$$Sum\ of\ Variance = \sum_{i=2}^{2N_g} (i - SE)^2\ P_{x+y}(i)$$

$$Sum\ of\ Average = \sum_{i=2}^{2N_g} \left[i P_{x+y}(i) \right]$$

$$Maximal\ probability = max\{P(i,j)\}$$

Inverse difference moment normalized measures the localized homogeneity of an image. In contrast to homogeneity- P, it normalizes the square of the difference between values by dividing over the square of the total number of discrete values. Inversed difference normalized is another way to measure the homogeneity.

$$Inverse\ difference\ moment\ normalized = \sum_{i=1}^{N_g} \sum_{j=1}^{N_g} \frac{P(i,j)}{1 + \left(\frac{|i + j|^2}{N^2} \right)}$$

$$Inverse\ difference\ normalized = \sum_{i=1}^{N_g} \sum_{j=1}^{N_g} \frac{P(i,j)}{1 + \left(\frac{|i + j|}{N} \right)}$$

Gray level run length matrix (GLRLM)

Gray level run length matrix ($P(i,j)|\theta$) quantifies the runs of gray level i and the length j in the volume ($V_{(x,y,z)}$). N_g represents the number of discrete gray levels intensity in V, and L_r is the length of the longest run in V.

Short run emphasis is the measurement of the short run length which is higher in a finer texture.

$$Short\ run\ length = \sum_{i=1}^{N_g} \sum_{j=1}^{L_r} \frac{P(i,j)}{j^2}$$

Long run length, in contrast to short run lengths represents a more coarse texture in a higher value.

$$Long\ run\ length = \sum_{i=1}^{N_g} \sum_{j=1}^{L_r} j^2\ P(i,j)$$

Gray level non-uniformity measures the similarity of the gray level intensity in the image.

$$Gray\ level\ non-unifirmity = \sum_{i=1}^{N_g} \left(\sum_{j=1}^{L_r} P(i,j) \right)^2$$

Run length non-uniformity measures the similarity of the run lengths in the image.

$$Run\ length\ non-unifirmity = \sum_{j=1}^{L_r} \left(\sum_{i=1}^{N_g} P(i,j) \right)^2$$

Run percentage measures the homogeneity and distribution of runs of an image.

$$Run\ Percentage = \frac{\sum_{i=1}^{N_g} \sum_{j=1}^{L_r} P(i,j)}{\sum_{j=1}^{L_r} j \sum_{i=1}^{N_g} P(i,j)}$$

Low gray level emphasis shows the distribution of low gray level intensity. Therefore, a lower value represents a greater concentration of low gray level intensity in the image. On the other hand, high gray level emphasis shows the distribution of high gray level

intensity in the image.

$$Low\ gray\ level\ enphasis = \sum_{i=1}^{N_g} \sum_{j=1}^{L_r} \frac{P(i,j)}{i^2}$$

$$High\ gray\ level\ enphasis = \sum_{i=1}^{N_g} \sum_{j=1}^{L_r} i^2 P(i,j)$$

Putting the above-mentioned features together, a total 13 first order features and 29 second order texture features generated a total number of 294 features from 7 different MR sequences. These features were applied to train supervised machine learning voxel-wised. Different machine learning models had been proposed by previous study[97]. Our preliminary results (used only training group with voxel intensity from different MR sequences as input features) showed that the convolutional neural network (CNN) had the best accuracy (Table 7.2). The CNN was processed by using the Neural Network Toolbox in Matlab version 2016b (Figure 7.2).

After the establishment of the trained model, a heat map of the probability of progression was calculated from the preoperative MRI of the validation group (Figure 7.2, gray box). These results were then compared and validated with their true follow-up progression MRI in both training group and external validation group. For external validation, 3 repeated trainings were done to optimise the validation.

Table 7.2 Comparison between different machine learning models

Machine learning model	Overall Accuracy
Tree	60.8-67.6%
Discriminant	60.8-62.5%
Supporting vector machine	64.9-73.8%
K near neighborhood	25-66.9%
Ensemble boosted tree	69.8%
Convolutional neural network	85.1%

The training results were calculated by using gray level intensity of each voxel from different MR sequences in 32 training group patients.

Statistical analysis

General patients' characteristics were tested for group differences with a t-test or Mann-Witney U test for continuous variable depending on the normality of the data. A chi-square test was used for categorical data. Differences between MRI characteristics of the preoperative area later showing tumour progression and non-progression areas were done using paired t-test. Two-sided *p*-values were used. All statistical tests were performed using SPSS version 22 (IBM Inc., New York, USA).

7.3 Results

7.3.1 Multimodal MRI Characteristics

Multimodal MRI characteristics were shown in Figure 7.4. The ADC values in the progression area were lower than 5mm and 10 mm peri-tumoural non-progression area (Figure 7.4 A, $p < 0.001$, 0.029). Fractional anisotropy (FA) showed lower in progression area than 5 mm non-progression area (Figure 7.4 B, $p = 0.041$). The isotropic p component showed a significant decrease in progression area than 5mm and 10mm of non-progression area (Figure 7.4 D, $p < 0.001$). In areas of progression, anisotropic q did not show difference between progression and non-progression area (Figure 7.4 E). In areas of later progression, there was significant increase in the FLAIR signal (Figure 7.4 C, $p = 0.020 \sim < 0.001$) and contrast enhanced T1 MRI (Figure 7.4 G, $p = 0.026 \sim 0.0004$) compared to non-progression area. Relative cerebral blood volume, was increased in the progression areas than 15-20 mm non-progression area (Figure 7.4 F, $p = 0.038 \sim 0.042$). A higher Cho/NAA and lower NAA can be seen in the progression areas but without statistical significance (Figure 7.4 H).

7.3.2 Radiomics Features

Thirty-five out of the 91 first order radiomics features had significant difference between progression area and non-progression area (Figure 7.5). Most distinct features were in ADC, p and contrast enhanced T1 MRI (Figure 7.5 A, C, F). In the 203 second order radiomics features, 77 were found to have significant difference between progression and non-progression areas (Figure 7.6). Total 112 radiomics features were identified in the progression areas.

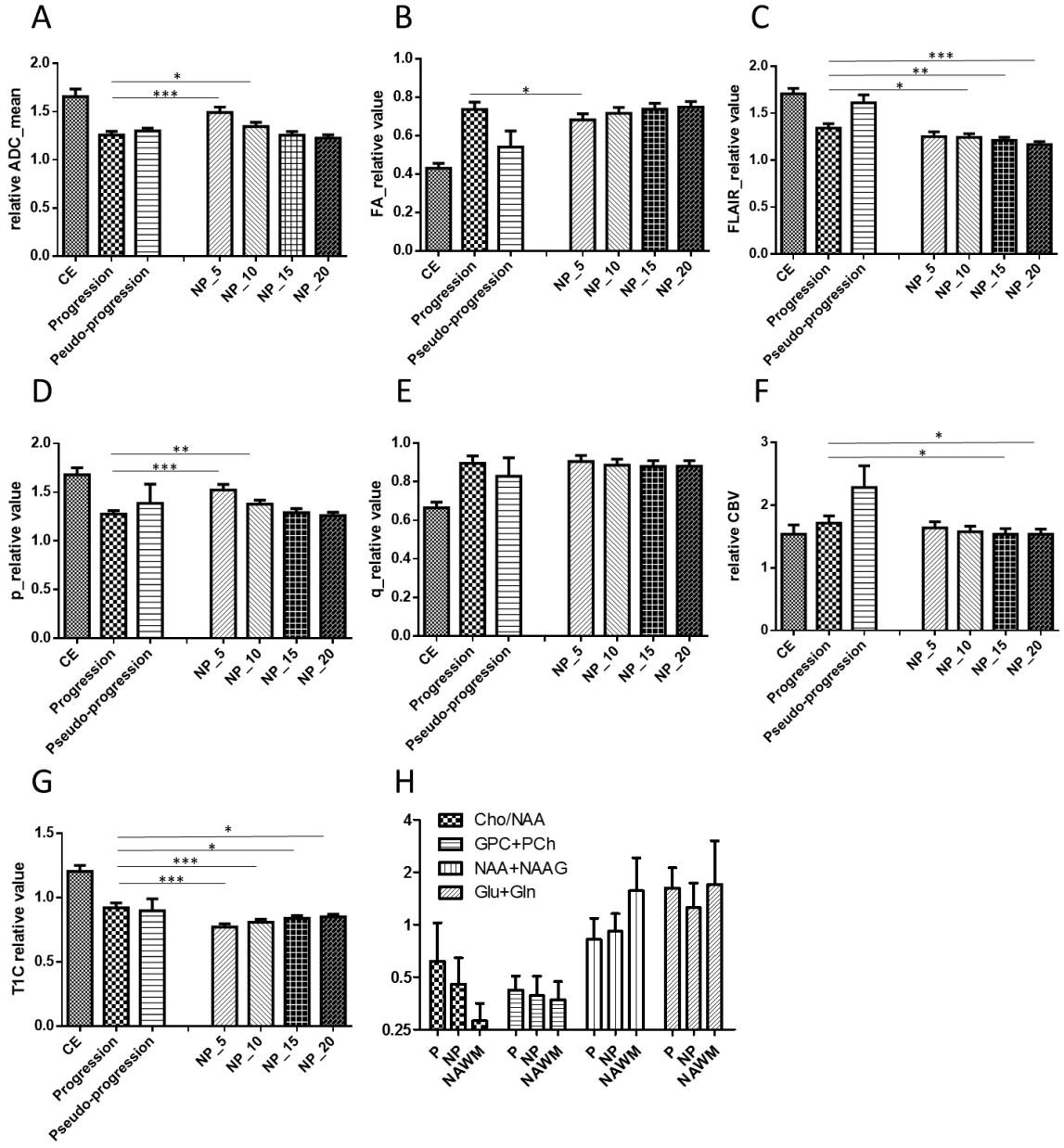

Figure 7.4

Figure 7.4 showed the MRI characteristics (A-G) of contrast enhanced, progression, non-progression (NP) area in 5-20 mm peritumoural area and contralateral normal appearing white matter (NAWM, control). H showed MRS of Cho/NAA, Choline, NAA+NAAG and Glu+Gln of progression (P), non-progression (NP) and NAWM.

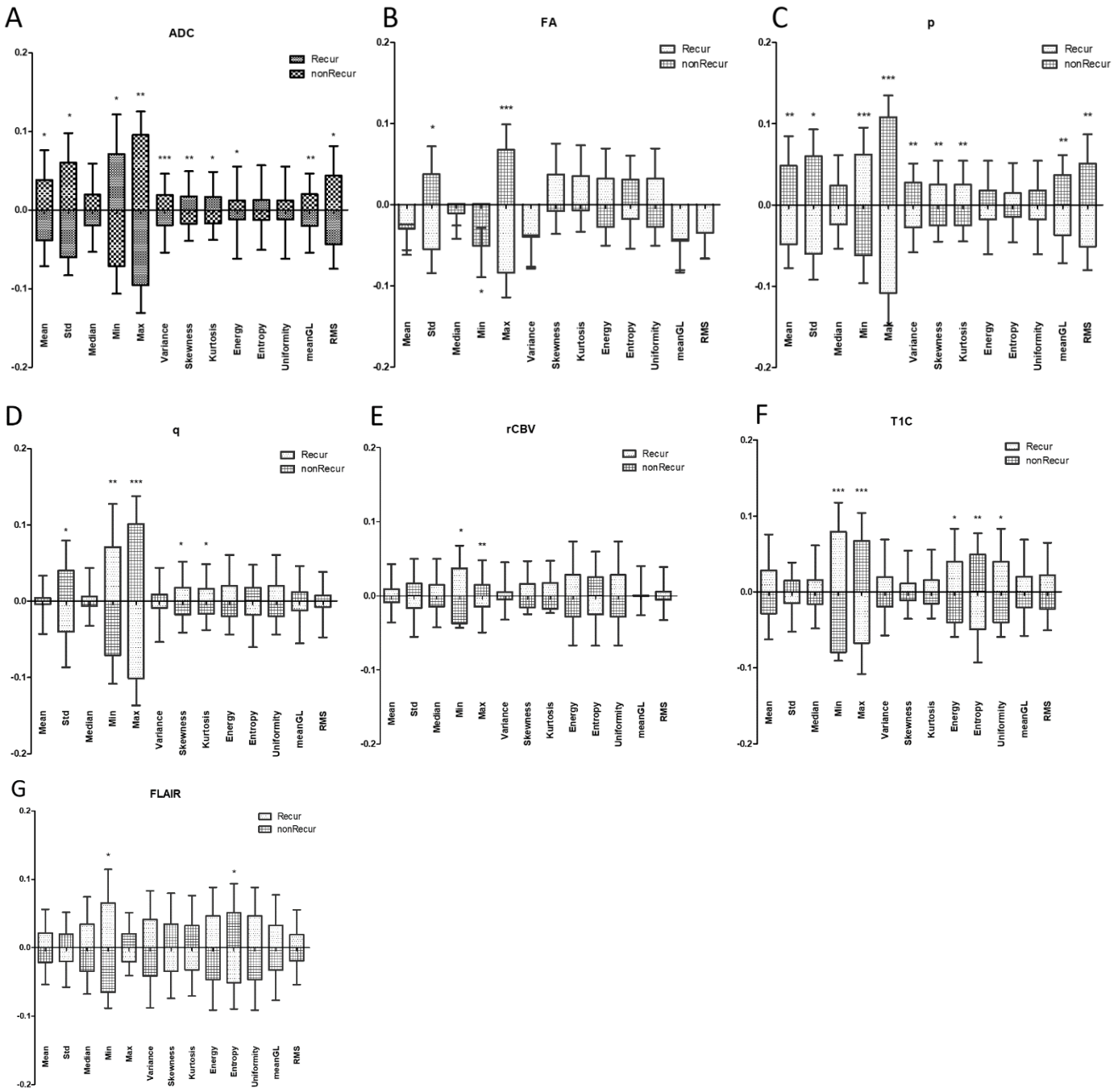

Figure 7.5 First order radiomics features

Comparison of the first order radiomics features between progression and non-progression area.

* $p < 0.05$; ** $p < 0.01$; *** $p < 0.001$

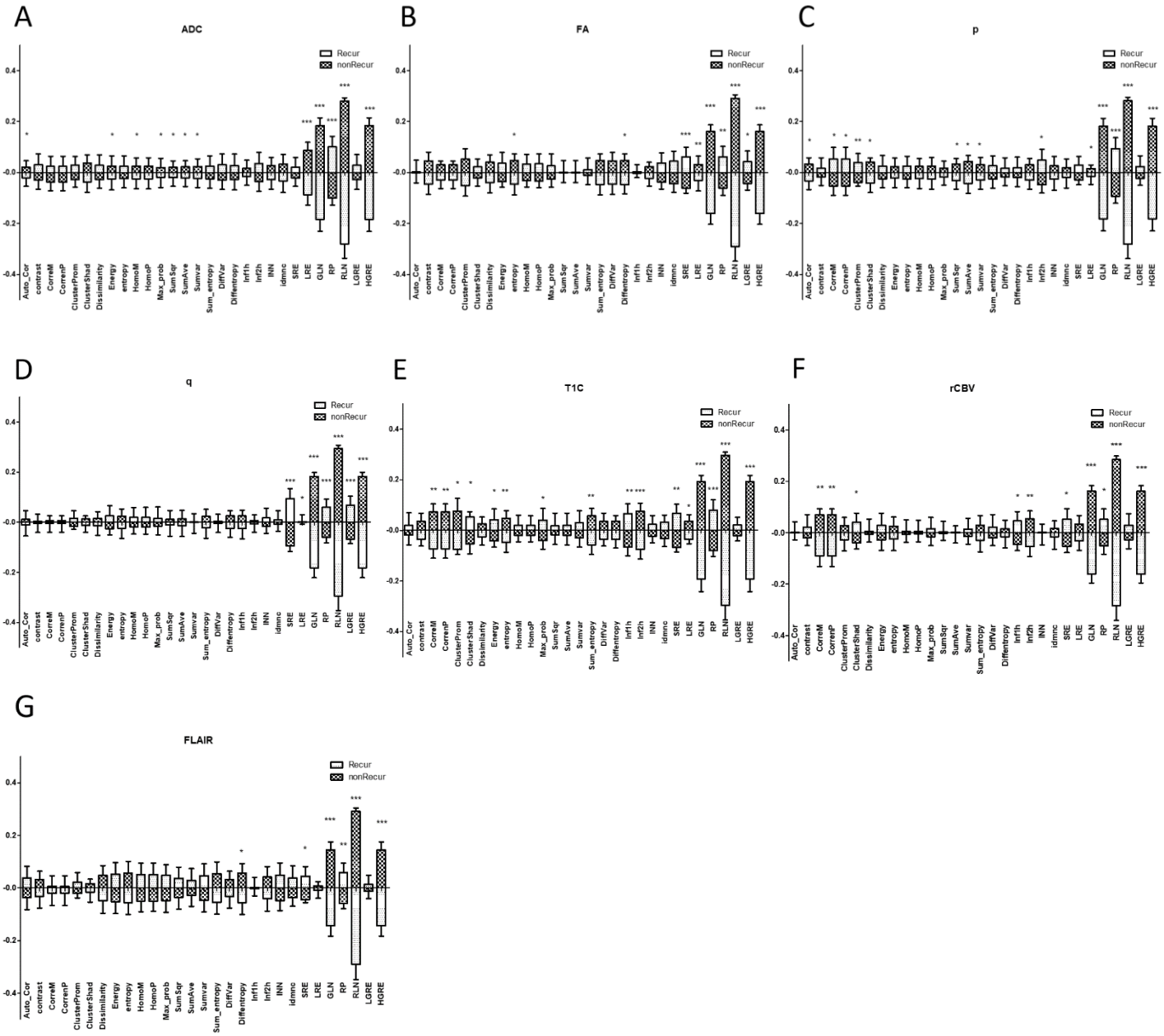

Figure 7.6 Secondary radiomics features

Comparison of the secondary order radiomics features between progression and non-progression area.

* $p < 0.05$; ** $p < 0.01$; *** $p < 0.001$

7.3.3 Identification of the progression areas from the pre-operative MRIs

In the training set (n = 32) of the supervised convolutional neural network, the overall accuracy 92.6% (Figure 7.7). The training, testing and validation accuracy were 92.7%, 92.4% and 92.4% respectively. The overall sensitivity was 80% and the overall specificity was 97.7%.

Further application of the trained model can be used to generate predicted areas of progression on the preoperative MRI, and the example case from training group was shown in Figure 7.8.

External validation in the 20 cases were done by overlapping the resulted progression map drawn by the convolutional neural network model and the actual progression MRI (Figure 7.9). 3 repeated validation results were shown in Table 7.3. The overall accuracy in the validation group was 78%. The positive predict value and the negative predict value were 17% and 78%.

Figure 7.7

The confusion matrix of the voxel-wise radiomics features in the supervised convolutional neural network model. The overall sensitivity, specificity and accuracy were 80%, 97.7% and 92.6% respectively.

Table 7.3 External Validation

	PPV	NPV	Overall Accuracy
Test 1	0.193	0.785	0.780
Test 2	0.134	0.785	0.780
Test 3	0.173	0.785	0.780
	0.167	0.785	0.780

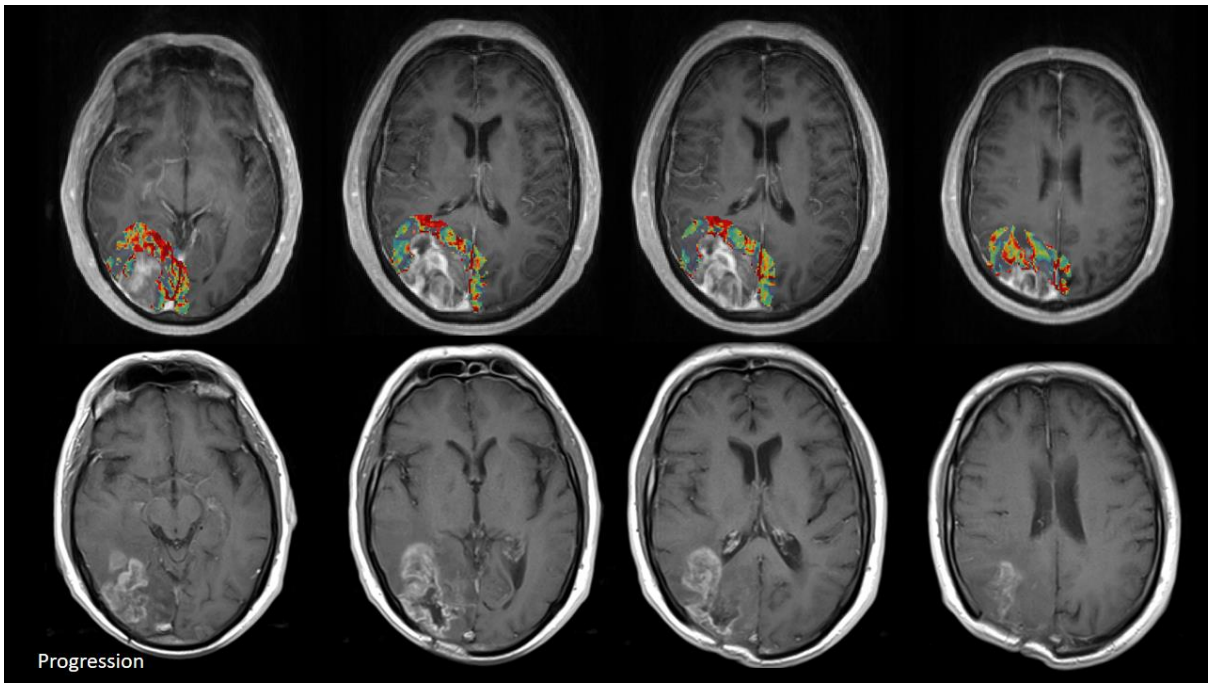

Figure 7.8

A representative case from the training group showed fair result of the identification of the progression area form the preoperative MRI. It showed a high probability of progression over the area near right lateral ventricle.

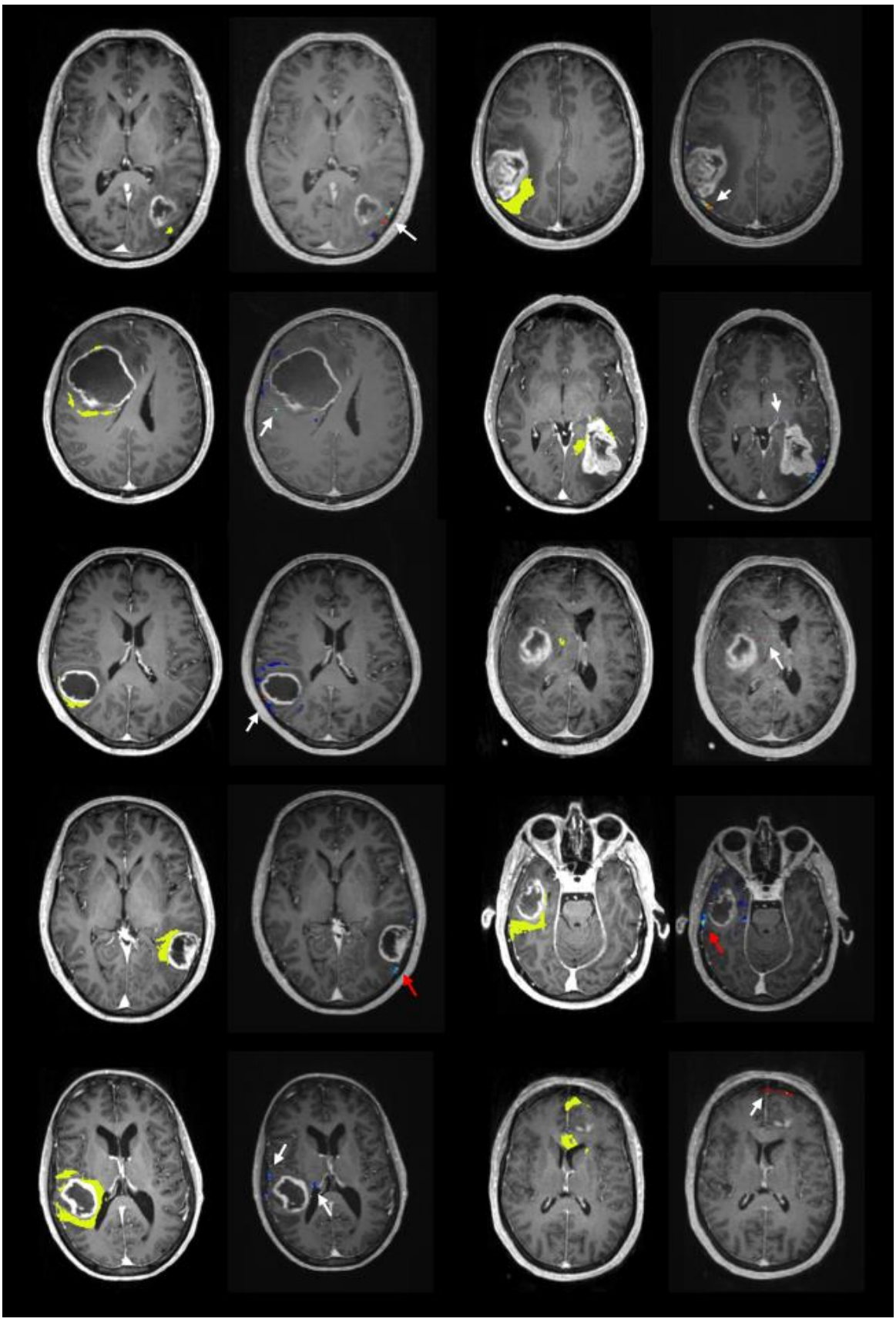

Figure 7.9 (part 1)

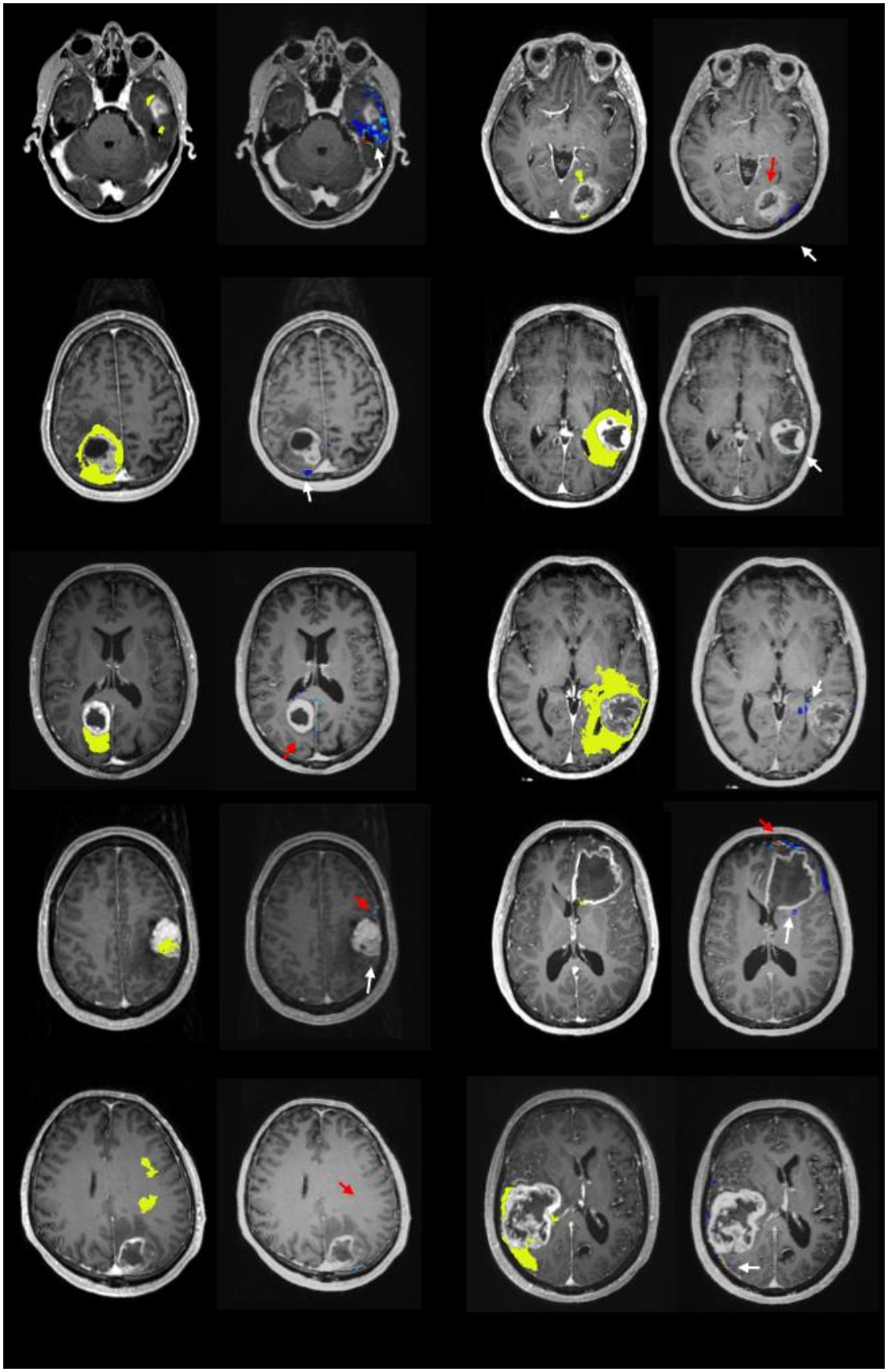

Figure 7.9 (part 2)

Figure 7.9

Progression probability heat maps were drawn on 20 external validation cases. The true progression on the follow up MRI were masked as yellow in each pair over the left hand side. The right figure in each pair showed the probability heat map. White arrow indicates a fair identification, while red arrow showed the suboptimal identification.

7.4 Discussion and Conclusion

Discussion

In this study, we showed distinctive imaging characteristics in the peritumoural areas that potentially progress. Lower ADC, p and higher FLAIR, contrast enhanced T1 signal were noted in these area. Furthermore, the comparison between progression and non-progression area by using radiomics features showed up to 112 different features. These features support the identification of the peritumoural invasive areas.

We found a significant lower ADC pixel value in the progression areas this may due to the increase cancer cellularity in this invasive peritumoural areas. ADC is usually used to quantify the diffusivity of the water. In the circumstances of the normal brain tissue or increase extracellular fluid, ADC may increase due to the un-restriction of the water diffusion. On the other hand, ADC may decrease due to increase cellularity which resulted to the restriction of the extracellular fluid diffusion[24]. ADC can be seen in higher grade glioma[143] resulted in a worse prognosis. In addition, an increase in ADC after treatment can be a favourable prognostic predictor[49].

DTI p is another representative form of the mean diffusivity. Therefore, similar results to the ADC were expected. Previous biopsy had shown an increase of 10% in the p can show tumour infiltration[105] and further MRS and rCBV study also showed that in these p abnormal peritumoural area can have higher Cho/NAA ratio and higher rCBV which refers to high cellular turnover rate and angiogenesis[113]. These cancer cell activity findings were compatible with our results that showed a lower DTI p in the peritumoural progression area. Our results did not show that DTI q as a feature contributed to the identification of the progression area. We have known from previous study that the DTI q was found to be largely representative of the cancer itself. In

Chapter 6, we showed this abnormal q map can be larger than the contrast enhancing lesion in approximate 50% of the GBM. Moreover, extent of resection study showed that a larger resection areas of the abnormal q can result in a better prognosis[166]. Further study in these peritumoural abnormal q areas showed that there were increase rCBV and increase Choline which also indicates cancer activity (Chapter 6). However, in this study, we found less features by using DTI-q, this may because there was another half of the cases that had q abnormal areas smaller or equal to the contrast enhancing areas that may potentially masked the difference. FA is the measurement of the relative anisotropy in DTI, however, the use of FA to differentiate tumour infiltrated oedema was controversial[79,156] and there was no significant voxel intensity difference between the progression and non-progression area in our results.

Our data showed that, in the area of progression there was a higher rCBV compare to the non-progression areas. The increase of the relative cerebral blood flow can be found commonly in GBM due to its neovascularization (Chapter1.3).

FLAIR and contrast enhanced T1C were the two conventional structural MRI that were found as progression features in our study. Although FLAIR represents the vasogenic oedema of the brain and is non-specific and can be affected by steroid treatment or antiangiogenic therapy such as Avastin. (Chapter 1.3). Many studies used the FLAIR to define the non-enhancing peritumoural area and able to detect abnormal cancer cell[36]. Lamee et al, found that about one third of the histology analysis in the FLAIR areas had cancer cell infiltration[70]. Therefore, despite some limitations of the FLAIR, a higher signal intensity found in the progression peritumoural zone can be explained by the possible tumour infiltration. In our study, we found the signal intensity of the contrast enhanced T1 MRI higher in the progression area. Although, the peritumoural ROIs were defined as non-enhancing area, this can be due to the subtle blood brain

barrier interference by the cancer infiltration that beyond human visual detection capability.

In addition to the difference of voxel value extracted from difference MRI sequences. We used quantitative radiomics feature to characterise the peritumoural progression area from the preoperative MRIs. We found a total 112 out of 294 features that are different between progression and non-progression areas. Most studies focused on the features of the contrast enhancing lesion. Gevaert et at, in 2014, showed the radiomics features can correlate with manual radiologist's Visually Accessible Rembrandt Images features, patient clinical survival[34]. Another study used quantified radiomics data from 121 GBM patients to cluster 3 distinct MR phenotypes, the peri-mulifocal, spherical and rim-enhanced[55]. They found each cluster had its different pathway which possibly explain the distinct prognosis.

The second aim of our study was to identify the progression peritumoural area from the preoperative MRI which was calculated by the supervised machine learning, convolutional neural network. Two of the main issues on the machine learning are the size of number for training and having enough qualitative input features. Our results in the radiomics provide a reasonable size of the features to the application of the convolutional neural networks. And total 294 features coded in every voxel generated a large number of the sample size that can be used to train the model. Although the optimal features number and the sample size were not tested in this study. Our attempt to use the convolutional neural network to draw the progression probability map from the preoperative MRI had shown moderately fair results with the overall accuracy around 78%. Although the positive predict value and the sensitivity were lower, however, the specificity and negative predict were good.

There are several limitations in this study. We are not able to take the MRI scan time point into consideration in this study, therefore this may cause potential temporal sampling error. GBM progression may change from time to time, our progression area was created by coregistration of the first true progression image to the reference image. This may underestimate the area of progression in our training group. Another limitation is the limited patient sample size. Although we trained the model voxel by voxel that increased a large amount of sample size, and most of the radiomics study require a large sample size in the machine learning in order to reach a stable training model. Besides, patients' clinical prognosis was different in the training group and the validation group (Table 7.1, OS: 523 versus 407 days, $p < 0.01$). The patients in the validation group received follow up in local hospitals and had worse prognosis. The cause of the difference was unknown, however this may cause a drop of 92.7% of overall accuracy in our initial training to 78% after the external validation.

Conclusion

Multimodal quantitative MR imaging analysis, including structure MRI, perfusion MR and diffusion tensor imaging can demonstrate distinct characteristics in areas of potential later progression on preoperative MRI. Moreover, the application of these imaging features to our cohort, site of tumour progression can be potentially identified via a trained machine learning model. However, due to the limited number of training, overfitting of the trained results cannot be rule out, therefore further validation study should be studied to achieve a more reliable model.

CHAPTER 8

DISCUSSION and CONCLUSION

8.1 General Conclusion

The aim of this thesis was to use multimodal MRI to understand the imaging characteristics of the peritumoural invasive area. The main hypothesis explored were:

1. **A more accurate image co-registration in brain tumour MRI between different time points can be achieved by using a two stage semi-automatic non-linear co-registration method to overcome the massive regional distortion caused by surgery or tumour progression. The first stage is to calculate the transformation between resected lesion and resected cavity, then secondly apply to the brain parenchyma. (Chapter 4)**

   In Chapter 4, we proposed a two stage semi-automatic non-linear co-registration method to coregister 32 tumour progression and post-operative MRI to the preoperative MRI. The target error validation showed that it is more accurate than the standard linear (FLIRT) or non-linear (FNIRT) method in most of the landmarks. There were less deviation of the centroid of tumour (p = 0.002), y coordinate of the cerebral aqueduct (p < 0.0001), y coordinate of the septum pellucidum (p <0.0001), and y/ z coordinate of the third ventricle (p < 0.0001).

2. **A larger extent of resection based on the DTI-defined invasive regions, can result in a better prognosis. Use the above method to coregister the post-operative MRI to the pre-operative MRI can conduct an accurate volumetric study to test the clinical effect of the extent of resection based on different MRI sequences. (Chapter 5)**

The volumetric study of the extent of resection of different MRI were shown in Chapter 5. Complete resection of the enhanced tumour shown on the postcontrast T1-weighted images was achieved in 24 of 31 patients (77%). The mean extent of resection of the abnormal p, q, and FLAIR areas was 57%, 83%, and 59%, respectively. Increased resection of the abnormal p and q areas correlated positively with progression-free survival (p = 0.009 and p = 0.006, respectively). Additionally, a larger, residual, abnormal q volume predicted significantly shorter time to progression (p = 0.008). More extensive resection of the abnormal q and contrast-enhanced area improved overall survival (p = 0.041 and 0.050, respectively). Therefore, a longer progression-free survival and overall survival were seen in glioblastoma patients in whom more DTI-q abnormality was resected.

3. **The peritumoural abnormal DTI-q defined invasive area using MRS and perfusion MRI can have imaging characteristics similar to the main tumour bulk, such as higher Cho/NAA ratio and increase regional perfusion. (Chapter 6)**

In Chapter 6, we included 51 patients with primary glioblastoma and showed that the peritumoural abnormal DTI-q areas have a higher Cho/NAA (p = 0.0346), especially the Cho/Cr (p = 0.0219). The rCBV were not different between the peritumoural DTI-q abnormal and normal area (p = 0.0798).

Different method of the analysis of the MRS voxels were compared in this chapter. There were no significant different by using the visually selection and the 3D voxel-wise approach (p = 0.1046 ~ 0.8993). However, this also highlights the potential use of this objective way to obtain MRS voxel data.

4. **Different phenotypes of the peritumoural DTI-q defined invasive margin can be an independent factor correlating with patient prognosis. (Chapter 6)**

   The patients with larger abnormal q ROIs than contrast enhancing area had a better progression free survival (median: 287 vs 53 days, p = 0.0013) and overall survival (median: 464 vs 274 days, p = 0.0055) than those with smaller peritumoural abnormal q ROIs. These results were controlled by the age, gender, extent of resection based on contrast enhanced lesion, use of Gliadel, IDH-1 mutation status, and MGMT promoter hypermethylation status. Although these peritumoural abnormal DTI-q ROIs are infiltrative tumour cell, the longer survival in patients with larger abnormal DTI-q can be hypothesised due to a better local control by surgical resection and radiation therapy. The EOR based on the contrast enhanced lesion was controlled in two groups, however, the EOR of DTI-q did not test in these group. Therefore, the better clinical outcome may due to a larger EOR of DTI-q. Besides, in our finding, the peritumoral abnormal q ROIs had higher Choline, which represents higher cellular turnover rate. Therefore, under the standard postoperative CCRT, the better local control can be due to higher radiation sensitive. In summary, the phenotype of the peritumoural DTI-q abnormal area can be an independent factor to patients' prognosis.

5. **The two stage non-linear semi-automatic coregistration method to coregister MRI at tumour recurrence/ progression to the pre-operative MRI can identify the regions where eventually recur/ progress. And these peritumoural areas that potentially recur/ progress can have distinct imaging characteristics comparing to other normal peritumoural area by using multimodal MRI and radiomics approach. (Chapter 7)**

In Chapter 7, we had shown distinct imaging characteristics of the peritumoural progression area. There were higher ADC (p < 0.001, 0.029), DTI-p (p < 0.001), FLAIR (p = 0.020 ~ < 0.001), and higher rCBV (p = 0.038 ~ 0.042) in the peritumoural progression area compared to different extent of the non-progression areas. Besides, lower FA (p = 0.041) and contrast enhanced T1 signal (p = 0.026 ~ 0.0004) were found in areas of progression.

In the radiomics features analysis, there were 112 radiomics features that identified in the progression areas. Thirty-five out of the 91 first order radiomics features and 77 out of 203 second order features had significant difference between progression area and non-progression area. These finding concluded that various imaging features can characterise the peritumoural progression area pre-operatively.

6. **The imaging characteristics obtained from the abovementioned can be used to establish a prediction model to identify the possibility of tumour progression in the peritumoural zone of the pre-operative MRI by using the machine learning model (convolutional neural network). (Chapter 7)**

We applied totally 294 radiomics features into the convolutional neural network machine learning model to generate a model to identify areas of potential progression from the preoperative MRI. This can be shown in the probability heat map. The overall accuracy was 92.6% with 80% of overall sensitivity and 97.7% of the overall specificity. However, the accuracy decreases to 78% after external validation. According to the result, we were not able to generate a stable model to identify the progression area from the pre-operative MRI. However, this still showed the potential of the application of the radiomics, together with machine

learning in the understanding of the peritumoural area where progress later on.

8.2 Limitation of the study

The limitations of each studies were discussed in the discussion of Chapter 4, 5, 6 and 7. Several general limitations were described as following.

Determination of the optimal Co-registration method

As Chapter 4 described, it is difficult to co-register MRI with lesion between different time points due to its massive regional deformation. Although we proposed a two stage semi-automatic non-linear co-registration method that shown to be more accurate than standard method. Most of the co-register deviation were < 3mm, however, there were still deviation up to 5mm in some of the coordinate (x and z coordinate of the tumour centroid between progression and pre-operative MRI). This may be a limitation to the volumetric study in Chapter 5 and the determination of the peritumoural progression area in Chapter 7. Therefore, a more accurate and robust method to overcome the regional deformation between time points in lesional brain MRI is needed in the future study.

Inconsistent sampling time of the follow up MRI

In Chapter 3, we described the MRI acquisition time point and consistent protocol of the preoperative diagnostic MRI and the immediate post-operative MRI. Many studies hve addressed the important of the standard of the MRI acquisition[159]. However, the interval of the follow-up MRI were obtained in a more flexible time point. Despite a general principle of MRI examination before and after CCRT, and follow-up every three months, most follow-up MRI were obtained according to the clinical presentation, and

some varied from once a month to twice a year in our cohort. Therefore, this inconsistency of the sampling time may be a confounding factor to the study of tumour progression.

The progression MRI in some clinically stable patients may obtained during the routine follow-up, whist some were done due to clinical deterioration. This may influence the determination of the peritumoural progression area in this study (Chapter 7) which were done by co-registration of the first progression MRI to the pre-operative MRI. Furthermore, when validation of the generated probability progression heat map, we compared the resulted heat map to the first progression MRI of the external validation MRI. The sensitivity could be underestimated, because we did not correct the time to progression between training group and validation group.

Lack of image guided biopsy

One of the main object of this study is to understand about the imaging biomarkers of the peritumoural invasive area in GBM. Kentarci in Mayo Clinics suggested that an ideal imaging biomarker has four characteristics: 1) detecting a fundamental feature of the pathology, 2) being diagnostically sensitive and specific through validation in neuropathologically confirmed cases, 3) being precise with good test re-test reproducibility for monitoring the therapeutic effects on the pathology, 4) being available and accessible for multi-center studies [64]. Of these, the most important is the validation with its biological characteristics.

Our limitation is lack of the image guided biopsy to confirm our finding about image characteristics in the peritumoural progression area. Therefore, although we found a larger extent of resection on the DTI-q defined invasive area can result a better prognosis (Chapter 5) and further MRS study showed that these peritumoural DTI-q

abnormal area had a high Cho/NAA ratio (Chapter 6). It is still lack of direct evidence to conclude actual tumour activity in the invasive margin. Further image guided biopsy study is needed for the peritumoural progressive area.

8.3 Future direction

Studies in this thesis can lead to several works in the future:

An image guided biopsy under multimodal MRI

As previous mentioned, lack of patho-histology evidence is one of the limitation in our study. The image guided biopsy study in the further should take several issues into consideration:

1. Brain shift during and after the resection of GBM

   The brain shift during a brain surgery happens simultaneous after the craniotomy, and may shift furthermore after durotomy due to change of the incratranial pressure[86]. In order to overcome this issue, several techniques such as intra-operative sonography[116] or tracked laser scanner[25] had been developed. However, the brain shift problem can be minimize if the biopsy is taken before the durotomy followed by the schedule tumour removal. This can provide the most accurate spatial information for the biopsy specimen, although a prolong operation time up to 30-45 minutes may be expected.

2. Peritumoural heterogeneity and balance between adequate tissue sampling and patient safety.

   The biopsy targets of the peritumoural area can face the problem of peritumoural heterogeneity. Two approaches can be proposed. One is to do biopsy as much as possible, however, this may increase the risk of complication. However, the

complication can be minimised if the biopsy is done before the craniotomy in the same operation. The other is target to the pre-operative defined peritumoural invasive area. Although the previous method of identifying the progression area (Chapter 7) was based on purely image study, this provide a more targeted location to undergo biopsy.

3. Hypothesis of the microenvironment

   Studies had shown that the GBM cells in the non-enhanced area are different from the contrast enhanced part[5,36]. And the complexity of the molecular pathway in this regions remained not fully discovered. Therefore, a thorough plan of testing the molecular biology property should be carefully planned.

Incorporation of the imaging biomarkers into surgical decision

Our attempts to show the peritumoural invasive margin also showed its clinical benefit in the extent of resection study (Chapter 5). However, the study was undertaken retrospectively and the surgical plan was not based on the proposed invasive margin. Although a prolong PFS and OS can be shown, however, a further prospective study should be considered.

The surgical planning can be in two arms: 1. Aim for the contrast enhanced lesion with intraoperative 5-ALA. 2. Aim for the invasive margin with intraoperative 5-ALA. Since 5-ALA guided surgery can provide most benefit of extent of resection to the patients, it should be used in every case. This proposed study can not only compare the clinical benefit between surgical planning using different imaging modality, but also provide the understanding of the correlation between 5-ALA fluorescence and the proposed advanced MRI.

Improvement of the use of radiomics and machine learning in the assessment of GBM prognosis

As Chapter 7 discussed, the proposed model to identify progression area pre-operatively was not completely established. This may require more case numbers and an adjustment of time to progression. Besides, two other main topics should also be assessed further. One is the determination of input features in the machine learning, the other is choosing of the machine learning model. Feature selection is an important step prior to the training, also the method we used doesn't need feature selection, however, the training results may still be affected by the size of the features. Therefore, further optimization of the training features is needed. The other works can be done in the future is the establishment of a stable machine learning model suitable for our MRI analysis. Since, this thesis was not aim for the study in the bioinformatics science, we created our model by modifying from the established model and further customize to our study purpose. Therefore, a future collaboration with bioinformatics engineers is needed to provide a better model in our study.

APPENDIX A

Patients that used in each study were listed in Appendix Table A-1, and detailed characteristics were shown in Appendix Table A-2.

In Table A-1, showed the available MRI scans at time point of diagnosis, immediate post-operative and tumour progression.

indicates the patients used in the Chapter 4

indicates the patients used in Chapter 5

indicates the patients used in Chapter 6

indicates the patients in the training set of Chapter 7

patients in the external validation set of Chapter 7.

LMD: for those patients had their follow up in the local hospital were marked
Initial NA: the data was not available when the study began

Appendix Table A-1

Lab code	Diagnostic MRI	Post OP MRI	Progression MRI	Chapter 4 SAC	Chapter 5 EOR	Chapter 6 MRS	Chapter 7 Progression
001							
002							
004			LMD	Initial NA	Initial NA		
006							
008							
009							
010							
012			LMD	Initial NA			
013							
018			LMD				
019							
020			LMD		Initial NA		
021							
022			LMD		Initial NA		
024			LMD		Initial NA		
025			LMD		Initial NA		

026							
027							
028							
029							
030							
032							
033					Initial NA		
036							
037							
038			LMD		Initial NA		
039							
041							
042							
044			LMD		Initial NA		
045							
047					Initial NA		
048							
049					Initial NA		
050			LMD	Initial NA	Initial NA		
051			LMD	Initial NA	Initial NA		
052				Initial NA	Initial NA		
054							
055					Initial NA		
057				Initial NA	Initial NA		
058					Initial NA		
059			LMD	Initial NA	Initial NA		
060							
061							
062			LMD	Initial NA	Initial NA		
063					Initial NA		
064				Initial NA	Initial NA		
065				Initial NA	Initial NA		
066							
067							
068					Initial NA		
069					Initial NA		
070							
071			LMD	Initial NA	Initial NA		

073						
074			Initial NA	Initial NA		
078						
080						
081			Initial NA	Initial NA		
083						
084						
085			Initial NA	Initial NA		
086			Initial NA			
087				Initial NA		
088		LMD	Initial NA	Initial NA		
089						
091						
092			Initial NA	Initial NA		
098						
099		LMD	Initial NA	Initial NA		
100						
103		LMD	Initial NA	Initial NA		
104						
107						
108		LMD	Initial NA	Initial NA		
109		LMD	Initial NA	Initial NA		
110			Initial NA	Initial NA		
112						
113						
116			Initial NA	Initial NA		
117		LMD	Initial NA	Initial NA		
118			Initial NA	Initial NA		
120			Initial NA	Initial NA		

Appendix table A-2 Patients Characteristics

Lab Code	sex	Age	OP date	EOR	Unit	Gliadel 0=no; 1=yes	Tumour volume ml	Tumour location *	midline shift cm	IDH-1 0=no; 1=yes	MGMT 0=no; 1=yes	PFS days	OS days
001	M	59	2010/8/2	GTR	C	1	44.92	2	8.5	0	0	246	548
002	M	61	2010/8/6	STR	C	1	48.77	1	1.66	0	1	244	292
004	M	61	2010/9/10	GTR	I	1	40.22	2	1.83	0	0	389	588
008	M	66	2010/10/29	GTR	C	1	79.88	1	7.69	0	0	14	14
009	F	61	2010/11/01	GTR	C	0	53.30	3	5.4	0	0	367	470
010	F	51	2010/11/5	STR	C	0	50.59	1	4.87	0	0	244	292
012	M	61	2010/11/26	GTR	I	1	53.72	1	6.14		1	153	785
013	F	66	2010/12/6	STR	C	1	24.35	2	11.9	0	0	198	890
019	F	65	2011/2/14	GTR	C	0	30.16	3	0	0	1	189	434
020	M	62	2011/2/18	STR	N	0	112.73	2	6.28	0	0	109	235
021	M	52	2011/3/11	GTR	C	1	20.10	3	0	0	0	929	1025
022	M	61	2011/3/18	STR	I	0	64.89	2	6.2	0	0	109	190
024	M	63	2011/4/26	STR	I	1	33.94	2	3.37		1	164	407
025	M	67	2011/5/3	GTR	N	0	31.66	3	9.44	0	0	265	326
026	F	38	2011/5/16	GTR	C	0	8.94	2	3.84	0	1	758	1077
027	F	64	2011/6/10	STR	C	0	11.9	1	0	0	0	182	287
032	F	65	2011/7/11	GTR	C	1	75.04	3	8.78	0	0	262	351
036	M	68	2011/8/12	GTR	C	1	60.31	3	0	0	1	444	501
038	M	57.0	2011/9/16	GTR	N	1	14.97	2	2.81	0	0	264	348
039	F	31	2011/9/19	GTR	C	0	37.17	2	10	0	1	310	475
041	M	63	2011/10/7	GTR	C	0	31.30	1	4.08	0	1	550	1217
042	M	68	2011/10/21	GTR	C	1	77.32	2	8.53	0	0	424	510
044	M	72	2011/11/11	GTR	N	1	34.29	3	0	0	1	143	248
045	M	63	2011/12/2	GTR	C	1	90.59	3	8.74	0	1	1130	1259
050	F	63	2012/1/20	STR	N	1	25.77	2	1.52	0	0	130	424
051	F	51	2012/1/20	STR	N	1	28.00	3	1.96	0	0	165	709
052	M	62	2012/2/17	GTR	N	1	41.81	1	3.47	0	0	507	782
054	M	59	2012/3/9	GTR	C	1	22.24	2	0	1	1	182	287
058	M	65	2012/3/30	GTR	I	1	29.66	3	3.53	0	1	224	1006
059	F	62	2012/4/2	GTR	N	0	29.66	3	3.2	0	1	406	551
060	M	49	2012/4/4	GTR	C	1	52.24	3	2.25	0	1	607	794
061	F	50	2012/4/27	GTR	C	1	43.58	3	7.03	0	1	648	1173
062	M	61	2012/6/1	GTR	I	0	33.51	1	0	0	0	158	384

064	M	39	2012/7/2	GTR	N	0	30.34	3	2.99	0	0	193	422
066	M	36	2012/7/16	GTR	C	1	56.08	1	1	0	0	283	588
067	F	49	2012/7/20	GTR	C	1	55.85	2	0	0	0	276	523
070	M	46	2012/8/6	GTR	C	0	30.34	2	3.54	1	1	589	1333
071	M	69	2012/8/17	STR	N	1	20.12	2	2.39	0	0	115	261
073	M	61	2012/9/24	GTR	C	0	118.55	1	2.24	0	0	221	286
074	M	63	2012/10/15	GTR	N	0	67.95	1	6.96	0	0	119	413
078	M	50	2012/11/30	STR	C	1	17.04	1	0	0	0	109	461
080	M	61	2013/1/4	GTR	C	1	8.41	3	0	0		117	384
081	M	50	2013/1/18	STR	C	0	13.00	3	1.7	0		111	455
085	M	54	2013/3/15	GTR	C	0	48.28	3	2.86	0		248	403
088	F	68	2013/5/13	GTR	C	0	24.82	2	0	0		136	261
091	M	65	2013/6/14	STR	C	0	42.22	2	0	0		378	839
092	M	67	2013/6/25	STR	I	0	64.43	3	4.69	0		90	93
098	F	66	2013/10/18	GTR	C	0	9.34	3	0	0		431	462
099	M	50	2013/10/21	GTR	I	0	11.81	3	0	0		521	578
100	M	63	2013/10/25	STR	C	0	77.59	2	0	0		47	104
103	M	65	2013/11/8	GTR	N	1	26.79	3	0	0		441	605
104	M	67	2013/12/13	GTR	C	0	27.04	1	3.19	0		747	901
107	M	38	2014/1/24	GTR	C	0	8.19	1	0	1		108	445
108	F	34	2014/2/6	GTR	I	0	57.60	1	7.43	1		181	303
109	M	51	2014/2/7	GTR	N	0	12.71	3	4.28	0		678	737
110	F	22	2014/2/17	STR	C	0	55.84	2	14.6	1		175	279
112	M	36	2014/4/11	GTR	C	0	36.26	1	3.4	0		105	287
113	F	68	2014/4/7	STR	C	0	55.09	1	2.6	0		25	284
116	M	70	2014/5/2	GTR	C	0	30.25	2	0	0		277	277
117	F	68	2014/5/19	STR	I	0	92.87	2	10.1	0		212	288
118	F	66	2014/5/23	GTR	C	0	54.87	1	3.5	0	0	104	269
120	F	64	2014/6/21	GTR	C	0	19.77	2	0	0	0	572	572

Tumour volume (ml): based on T1 weighted with contrast MRI

EOR: extent of resection

GTR: gross total resection (based on T1 weighted with contrast MRI)

STR: subtotal resection

Unit: follow-up unit

C: Cambridge; I: Ipswich; N: Norwich

Tumour location: refer to the relationship with eloquent area[120]

1= eloquent; 2 = near eloquent; 3 = non eloquent

APPENDIX B - DTI Analysis Scripts

1. Re-orientation all images
   nii_to_radio <input> radio
2. Unify central point of brain with anterior commissure
   SPM
3. Eddy correction DTI data
   eddy_correct DTI.nii data 0
4. Brain extraction DTI
   bet DTI.nii DTI_brain.nii.gz –f 0.05 –m
5. Manual correction brain extraction with *fslview*
   output: DTI_brain_mask_m
6. Create binary mask for further calculation
   fslmaths DTI_brain_mask_m.nii.gz –div DTI_brain_mask_m.nii.gz
   DTI_brain_mask_m_bin.nii.gz
7. Create extracted brain with manual corrected mask
   fslmaths DTI.nii –mul DTI_brain _mask_m_bin.nii.gz DTI_brain_m.nii.gz
8. DTI analysis
   dtifit -k data -m DTI_brain_m -r DTI.bvecs -b DTI.bvals -o dti
9. Create different maps
   fslmaths dti_MD -mul 1.732 DTI_p
   fslmaths dti_L1 -sub dti_MD -sqr DTI_L1diff
   fslmaths dti_L2 -sub dti_MD -sqr DTI_L2diff
   fslmaths dti_L3 -sub dti_MD -sqr DTI_L3diff
   fslmaths dti_L1diff -add dti_L2diff -add dti_L3diff -sqrt DTI_q

APPENDIX C – General Matlab Imaging Analysis Function

Pixel value extraction

Pixel value extraction from the base images of the specific ROIs was done by the following function.

```
% Load image
data=load_untouch_nii('base_images.nii.gz');
% Load mask file
mask=load_untouch_nii('ROIs.nii');
data=data.img;
mask=logical(mask.img);
% pixel extraction
pixels=data(mask);
M1=mean(pixels1);
```

Images combination and image extraction

Creation new mask files by combining, intersecting and extracting of different ROIs were done by the following functions:

```
% Load mask 1 file
mask1=load_untouch_nii('roi1.nii');
% make it logical
roi1=logical(mask1.img);
% Load mask 2 file
mask2=load_untouch_nii('roi2.nii');
% make it logical
roi2=logical(mask2.img);
% combine two ROIs
roi3=combineroi(roi1,roi2,'union');
% extract overlying areas of two ROIs
roi3=combineroi(roi1,roi2,'intersect');
% extract area of roi1 without roi 2 = roi1 - roi2
roi3=combineroi(roi1,roi2,'unique');
% save new ROI
temp4=mask1; temp4.img=roi1;
save_untouch_nii(temp4, 'new_ROIs.nii.gz')
```

Volume calculation

Volume (vol) calculation of different ROIs for the extent of resection volumetric study was done by the following function:

```
% load ROIs
mask=load_untouch_nii('roi.nii');
% Voxel volume
vv=mask.hdr.dime.pixdim(2)*mask.hdr.dime.pixdim(3)*mask.hdr.dime.pixdim(4);
% aware of the max value in hdr
vol=sum(mask.img(:))*vv/1000;
```

Note:
The analysis of nifty file in the Matlab is proceeded by using the “Tools for NifTi and ANALYZE image” (https://uk.mathworks.com/matlabcentral/fileexchange/8797-tools-for-nifti-and-analyze-image?requestedDomain=www.mathworks.com Copyright (c) 2014, Jimmy Shen)

APPENDIX D – Script of the two stage non-linear semi-automatic coregistration

Steps and code of a semi-automatic method to coregister a preoperative MRI image of a patient with a brain tumour to follow-up images, for example direct or later postoperative. The steps are illustrated in Figure 1 with corresponding step numbers.

1. Brain extraction of the preoperative and follow-up T1-weighted scans with gadolinium

   Code: bet T1C T1C_brain -f 0.5 -B

   Explanation: (bet <in> <out> <options>). Input is an original T1-weighted image <T1C>. A brain extracted image <T1C_brain> and binary brain mask <brain_mask> will be created. The brain mask can be manually corrected using fslview.

2. The brain_mask is inverted creating the brain contour images

   Code: fslmaths brain_mask -mul -1 -add 1 T1C_brain_mask_inv

   Explanation: (fslmaths <input> <options> <output>). The image is multiplied by -1 and 1 is added.

3A. Segmentation to identify ventricles and enhancing tumour area or resection cavity for preoperative and follow-up scans

   Code: fast -t 1 -n 4 -o T1C_brain T1C_brain

   Explanation: (fast <options> <output> <input>). Input is the previously created brain extracted T1-weighted image <T1C_brain>. Segmentation creates a map of the ventricles and contrast enhancing tumour region <pve_0>. It is recommended to check this step and correct manually if needed.

3B. Create binary mask of brain contour, ventricles and lesion for preoperative and follow-up scans

   Code: fslmaths brain_mask_inv -add pve_0 (ref/in)_mask

   Explanation: (fslmaths <in> <option> <in> <output>). The brain contour is added to the

ventricles and lesion.

4. Create linear transformation matrix

   Code: flirt -ref pre/ref_mask -in followup/in_mask -out FL_followupT1C_2_preT1C -omat FL_followupT1C_2_preT1C.mat -cost normmi -searchrx -90 90 -searchry -90 90 -searchrz -90 90 -dof 12 -interp trilinear

   Explanation: Reference image <-ref> is the preoperative binary mask of the brain contour, ventricles and contrast enhancing lesion. Input image <-in> is the follow-up binary mask of the brain contour, ventricles and resection cavity. Output <-omat> is the matrix used in the next step.

5. Create nonlinear transformation matrix which includes binary mask as input

   Code: fnirt --ref=pre/T1C_brain --refmask=pre/ref_mask --in=followup/T1C_brain --inmask=followup/in_mask --aff=FL_followupT1C_2_preT1C.mat --cout=transform --config=config.cnf

   Explanation: The reference image <--ref> is the preoperative T1-weighted image. The reference mask <--refmask> is the binary mask of the brain contour, ventricles and contrast enhancing lesion. The input images are the follow-up T1-weighted scan <--in> and binary mask of the follow-up brain contour, ventricles and resection cavity <--inmask>. Output <--cout> is a transformation matrix.

6. Coregister brain from the follow-up scan with the preoperative scan

   Code: applywarp --ref=pre/T1C_brain --in=followup/T1C_brain --warp=transform --out=T1C_brain_coreg

Explanation: The reference <--ref> is the preoperative brain extracted scan. Input <--in> is the brain extracted follow-up scan. The transformation matrix <--warp> was formed in the previous step.

APPENDIX E- Script of the Extent of Resection Based on DTI Study

Steps cavity/lesion

1. Use cavity from post data, save as lesion_mask.nii.gz
2. Create binairy mask cavity
   fslmaths lesion_mask.nii.gz –div lesion_mask.nii.gz lesion_mask_bin.nii.gz
3. Coregister cavity to T1C pre

   applywarp --ref=pre/Anatomical/T1C_brain_B_m.nii.gz --
   in=post/Anatomical/lesion_mask_bin.nii.gz
   --warp=FL_ postT1C_2_preT1C.nii.gz --
   out=post/Anatomical/lesion_mask_coreg2preT1C
4. Manually check for scattering ROIs outside of main lesion

Steps FLAIR data

5. Apply nii_to_radio to align all images
6. Add 0 0 0 point on anterior commissure
   SPM reorient
7. Brain extraction FLAIR
   bet T2F.nii T2F_brain.nii.gz –f 0.5 -m
8. Manual correction brain extraction
   fslview to edit mask, save as T2F_brain_mask_m
9. Create binary mask
   fslmaths T2F_brain_mask_m.nii.gz –div T2F_brain_mask_m.nii.gz
   T2F_brain_mask_m_bin.nii.gz
10. Create extracted brain with manual corrected mask
    fslmaths T2F.nii –mul T2F_brain_mask_m_bin.nii.gz T2F _brain_m.nii.gz
11. Coregister T2F pre data with T1C pre data
    # run in folder P---

    flirt -ref pre/Anatomical/T1C_brain_B_m.nii.gz -in pre/Anatomical/ T2F_brain_m.nii.gz -
    out FL_post 2F_coreg2preT1C -omat FL_preT2F_2_preT1C.mat -cost normmi -searchrx -
    90 90 -searchry -90 90 -searchrz -90 90 -dof 12 -interp trilinear
    flirt -ref pre/DTI/DTI_brain_m.nii.gz -in pre/Anatomical/ T2F_coreg2preT1C.nii.gz out
    pre/Anatomical/T2F_coreg2preDTI -applyxfm -init FL_ preT1C_2_preDTI.nii.gz -interp
    trilinear
12. Draw T2F mask (threshold painting) and save as pre/Anatomical/preT2F_mask.nii.gz
13. Add pre_lesion_mask_bin.nii.gz to preT2F_mask.nii.gz and save as
    preT2F_lesion_mask.nii.gz

fslmaths pre/Anatomical/lesion_mask_bin.nii.gz -add
pre/Anatomical/preT2F_mask.nii.gz pre/Anatomical/preT2F_lesion_mask.nii.gz

Steps DTI data

14. Draw ROI p (threshold painting + manual correction) and save as pre/DTI/prep_mask.nii.gz
15. Draw ROI q (manually) and save as pre/DTI/preq_mask.nii.gz
16. Add pre_lesion_mask_bin.nii.gz to prep_mask.nii.gz, preq_mask.nii.gz, and save as prep_lesion_mask.nii.gz, preq_lesion_mask.nii.gz

fslmaths pre/Anatomical/lesion_mask_bin.nii.gz -add pre/DTI/prep_mask.nii.gz
pre/DTI/prep_lesion_mask.nii.gz
fslmaths pre/Anatomical/lesion_mask_bin.nii.gz -add pre/DTI/preq_mask.nii.gz
pre/DTI/preq_lesion_mask.nii.gz

Steps ROI determination

17. Resection T1C In GTR patients

Combine post/Anatomical/lesion_mask_coreg2preT1C.nii.gz with
pre/Anatomical/lesion_mask_bin.nii.gz
fslmaths pre/Anatomical/lesion_mask_bin.nii.gz -add
post/Anatomical/lesion_mask_coreg2preT1C.nii.gz
post/Anatomical/lesion_mask_GTR.nii.gz
fslmaths post/Anatomical/lesion_mask_GTR.nii.gz –div
post/Anatomical/lesion_mask_GTR.nii.gz post/Anatomical/lesion_mask_GTR_bin.nii.gz

18. Resection p

Post/Anatomical/lesion_mask_coreg2preT1C.nii.gz intersection with
pre/DTI/prep_lesion_mask.nii.gz
Use Matlab

```
mask1=load_untouch_nii('pre/DTI/prep_lesion_mask.nii.gz');
roi1=logical(mask1.img);
mask2=load_untouch_nii('post/Anatomical/lesion_mask_GTR.nii.gz');
roi2=logical(mask2.img);
roi3=combineroi(roi2,roi1,'intersection');
temp=mask1;
temp.img=roi3;
save_untouch_nii(temp,'post/DTI/Resection_p_mask.nii.gz');
```

19. Resection q

```
mask1=load_untouch_nii('pre/DTI/preq_lesion_mask.nii.gz');
roi1=logical(mask1.img);
```

```
mask2=load_untouch_nii('post/Anatomical/lesion_mask_GTR.nii.gz');
roi2=logical(mask2.img);
roi3=combineroi(roi2,roi1,'intersection');
temp=mask1;
temp.img=roi3;
save_untouch_nii(temp,'post/DTI/Resection_q_mask.nii.gz');
```

20. Resection T2F

```
    mask1=load_untouch_nii('pre/Anatomical/preT2F_lesion_mask.nii.gz');
    roi1=logical(mask1.img);
mask2=load_untouch_nii('post/Anatomical/lesion_mask_GTR.nii.gz');
roi2=logical(mask2.img);
roi3=combineroi(roi2,roi1,'intersection');
temp=mask1;
temp.img=roi3;
save_untouch_nii(temp,'post/Anatomical/Resection_T2F_mask.nii.gz');
```

APPENDIX F – 3D voxel-wise approach MRS data acquisition

Example of the acquisition of Choline (GPC+PCh/Cr)

MakeCSInii_voxnum

```
% This script creates a template CSI grid that will be needed for
% Voxel-wise analysis
%  Need the header.txt and the 'Spec_voxels.xlsx' template
pats={'P'};
for kk=1:length(pats)
    headerinfo=CSIinfo('header.txt');
F=[headerinfo.ImageOrientationPatient(4),headerinfo.ImageOrientationPatient
(1);headerinfo.ImageOrientationPatient(5),headerinfo.ImageOrientationPatien
t(2);headerinfo.ImageOrientationPatient(6),headerinfo.ImageOrientationPatie
nt(3)];
      n=cross(F(:,1),F(:,2));
CSIa=[F(1,1)*headerinfo.PixelSpacing(1),F(1,2)*headerinfo.PixelSpacing(2),n
(1)*headerinfo.SliceThickness,headerinfo.ImagePositionPatient(1);F(2,1)*hea
derinfo.PixelSpacing(1),F(2,2)*headerinfo.PixelSpacing(2),n(2)*headerinfo.S
liceThickness,headerinfo.ImagePositionPatient(2);F(3,1)*headerinfo.PixelSpa
cing(1),F(3,2)*headerinfo.PixelSpacing(2),n(3)*headerinfo.SliceThickness,he
aderinfo.ImagePositionPatient(3);0,0,0,1];
      if exist([pats{kk},'/Coregistered\T2tse_brain.nii']);
      t2=load_untouch_nii([pats{kk},'/Coregistered/T2tse_brain.nii']);
   else
      t2=load_untouch_nii([pats{kk},'/Coregistered/T2tse_brain.nii.gz']);
   end
    T2a=[t2.hdr.hist.srow_x;t2.hdr.hist.srow_y;t2.hdr.hist.srow_z;0,0,0,1];
      % Convert affine to be same as would get from dicom header using
formula above
      T2a=[-T2a(1,:);-T2a(2,:);T2a(3,:);T2a(4,:)];
      T2a=[T2a(:,2),T2a(:,1),T2a(:,3),T2a(:,4)];
      if headerinfo.HeaderType==2
      af=-0.5;
      else
      af=0;
      end
       % Draw spectrosocpy grid for slice used for planning
```

```
grid=zeros(headerinfo.Rows+1,headerinfo.Columns+1,3);
for ii=0:headerinfo.Rows
for jj=0:headerinfo.Columns
    temp=CSIa*[ii+af;jj+af;0;1];
    temp=(T2a\temp)+[1;1;1;0];
    grid(ii+1,jj+1,:)=temp(1:3);
end
end
slice=int8(grid(1,1,3));
imshow(t2.img(:,:,slice)',[])
hold on
for ii=1:17
plot([grid(ii,1,2),grid(ii,end,2)],[grid(ii,1,1),grid(ii,end,1)]);
plot([grid(1,ii,2),grid(end,ii,2)],[grid(1,ii,1),grid(end,ii,1)]);
end
hold off
 % Determine shift in x,y and z for spectroscopy voxel.
temp=CSIa*[af;af;1;1];
temp=(T2a\temp)+[1;1;1;0];
% Conver to a shift per slice of the T2 image
deltax=(grid(1,1,1)-temp(1))/(grid(1,1,3)-temp(3));
deltay=(grid(1,1,2)-temp(2))/(grid(1,1,3)-temp(3));
% Number of slices from T2 image to cover in z
deltaz=floor(grid(1,1,3)-temp(3));
 % Import the spectroscopy data
tempXLSholder=('Spec_voxels.xlsx');
spec=xlsread(tempXLSholder);
% Mask for saving as Nifti
mask=t2;
img=mask.img(:,:,slice);
mask.img=zeros(size(mask.img));
temp=zeros(size(mask.img));
 for col=5:12
for row=5:12
    for snum=0:deltaz-1
temp(:,:,slicesnum)=roipoly(img,[grid(col,row,1)+(deltax*snum),grid(col+1,r
ow,1)+(deltax*snum);grid(col+1,row+1,1)+(deltax*snum),grid(col,row+1,1)+(de
ltax*snum)];grid(col+1,row+1,2)+(deltay*snum),grid(col,row+1,2)+(deltay*snu
```

```
m)]);
            end
            mask.img(temp==1)=spec(row,col);
        end
        end
        % Modify the header so the data is stored as floating point
        mask.hdr.dime.datatype=16;
save_untouch_nii(mask,[pats{kk,'CSIvoxel_VoxNum.nii']);
end
```

Calc_ratio_loop_Cho_forColourMAP

```
% Calculate the ratio of total creatinine to total choline from
spectroscopy data
% This script needs the metabolite 'spreadsheet.csv' to be available for
each patient
pats={'P'};
for ii=1:length(pats)
        res=zeros(16);
        % Import the spectroscopy data
        spec=importdata([pats{ii},'spreadsheet.csv'],',');
        % Sort the data values based on column and row
        spec.data=sortrows(spec.data);
         % Identify which columns of the spec data to use for the overlay
        ChoCrcol=find(strcmp(' GPC+PCh/Cr+PCr',spec.colheaders));
        Crcol=find(strcmp(' Cr+PCr',spec.colheaders));
         % Want to extract voxels based on column then row
        for jj=1:size(spec.data,1)
            col=spec.data(jj,1);
            row=spec.data(jj,2);
        % Calculate Cho/Cr ratio for voxels where both have SD <= 20%
            if spec.data(jj,ChoCrcol-1)<=20&&spec.data(jj,Crcol+1)<=20
                res(row,col)=spec.data(jj,ChoCrcol/Crcol);
            end
        end
        % Save the data to an excel sheet
        xlswrite([pats{ii},'ChoCr_ratio_data_forColourMAP.xls'],res)
end
%This .xls output will be used to create the respective .nii
```

MakeCSInii_Metabolite_loop

```
% FIRST need to create metabolite spreadsheets using Calc_ratio_loop for
the respective metabolites...
% Make sure the respective header.txt is in each patient file

pats={'P'};
for kk=1:length(pats)
    headerinfo=CSIinfo([pats{kk},'header.txt']);
% Create affine matrix from header information patient
F=[headerinfo.ImageOrientationPatient(4),headerinfo.ImageOrientationPatient
(1);headerinfo.ImageOrientationPatient(5),headerinfo.ImageOrientationPatien
t(2);headerinfo.ImageOrientationPatient(6),headerinfo.ImageOrientationPatie
nt(3)];
      n=cross(F(:,1),F(:,2));
CSIa=[F(1,1)*headerinfo.PixelSpacing(1),F(1,2)*headerinfo.PixelSpacing(2),n
(1)*headerinfo.SliceThickness,headerinfo.ImagePositionPatient(1);F(2,1)*hea
derinfo.PixelSpacing(1),F(2,2)*headerinfo.PixelSpacing(2),n(2)*headerinfo.S
liceThickness,headerinfo.ImagePositionPatient(2);F(3,1)*headerinfo.PixelSpa
cing(1),F(3,2)*headerinfo.PixelSpacing(2),n(3)*headerinfo.SliceThickness,he
aderinfo.ImagePositionPatient(3); 0,0,0,1];

% load base line reference, normallt T2
if exist([pats{kk},'T2tse_brain.nii']);
  t2=load_untouch_nii([pats{kk},'/Coregistered/T2tse_brain.nii']);
   else
      t2=load_untouch_nii([pats{kk},'/Coregistered/T2tse_brain.nii.gz']);
   end
T2a=[t2.hdr.hist.srow_x;t2.hdr.hist.srow_y;t2.hdr.hist.srow_z;0,0,0,1];
      % Convert affine to be same as would get from dicom header using
formula above
      T2a=[-T2a(1,:);-T2a(2,:);T2a(3,:);T2a(4,:)];
      T2a=[T2a(:,2),T2a(:,1),T2a(:,3),T2a(:,4)];
      % left corner of the first spectroscopy voxel, the other describes
the middle of the top left spoectroscopy volxel.
      % Need to add an adjustment factor for the second type.
      if headerinfo.HeaderType==2
      af=-0.5;
```

```
else
af=0;
end
% Draw spectrosocpy grid for slice used for planning
grid=zeros(headerinfo.Rows+1,headerinfo.Columns+1,3);
for ii=0:headerinfo.Rows
for jj=0:headerinfo.Columns
    temp=CSIa*[ii+af;jj+af;0;1];
    temp=(T2a\temp)+[1;1;1;0];
    grid(ii+1,jj+1,:)=temp(1:3);
end
end
slice=int8(grid(1,1,3));
imshow(t2.img(:,:,slice)',[])
hold on
for ii=1:17
plot([grid(ii,1,2),grid(ii,end,2)],[grid(ii,1,1),grid(ii,end,1)]);
plot([grid(1,ii,2),grid(end,ii,2)],[grid(1,ii,1),grid(end,ii,1)]);
end
hold off
% Determine shift in x,y and z for spectroscopy voxel.
temp=CSIa*[af;af;1;1];
temp=(T2a\temp)+[1;1;1;0];
% Conver to a shift per slice of the T2 image
deltax=(grid(1,1,1)-temp(1))/(grid(1,1,3)-temp(3));
deltay=(grid(1,1,2)-temp(2))/(grid(1,1,3)-temp(3));
% Number of slices from T2 image to cover in z
deltaz=floor(grid(1,1,3)-temp(3));
% Import the spectroscopy data
spec=xlsread([pats{kk},'ChoCr_ratio_data_forColourMAP.xls']);
% Mask for saving as Nifti
mask=t2;
img=mask.img(:,:,slice);
mask.img=zeros(size(mask.img));
temp=zeros(size(mask.img));
for col=5:12
for row=5:12
for snum=0:deltaz-1
```

```
temp(:,:,slicesnum)=roipoly(img,[grid(col,row,1)+(deltax*snum),grid(col+1,r
ow,1)+(deltax*snum),grid(col+1,row+1,1)+(deltax*snum),grid(col,row+1,1)+(de
ltax*snum)],[grid(col,row,2)+(deltay*snum),grid(col+1,row,2)+(deltay*snum),
grid(col+1,row+1,2)+(deltay*snum),grid(col,row+1,2)+(deltay*snum)]);
        end
            mask.img(temp==1)=spec(row,col);
        end
        end
        % Modify the header so the data is stored as floating point
        mask.hdr.dime.datatype=16;
        save_untouch_nii(mask,[pats{kk},'CSIvoxel_ChoCr.nii']);
end
```

Data_loop_MRS

```
% Template file
[temp_data,temp_text]=xlsread('Data Extraction Template Jimmy_CSI.xlsx');
% I can only use patients for whom I have NAWM, p-, q- and spectroscopy CSI
grid
pats={'P'};
for ii=1:length(pats)

pdata=load_untouch_nii([pats{ii},'/pre/CSI/coregistered_dti_p.nii.gz']);
qdata=load_untouch_nii([pats{ii},'/pre/CSI/coregistered_dti_q.nii.gz']);
rcbv_data=load_untouch_nii([pats{ii},'/pre/CSI/coregistered_rCBV.nii.gz']);
    % Load ADC data files
adc_data=load_untouch_nii([pats{ii},'/pre/CSI/coregistered_ADC.nii.gz']);
     adc_data.img=double(adc_data.img);
    %TEST 1
    % Adding ROI data
    NE=load_untouch_nii([pats{ii},'/T2F_mask.nii']);
    %TESTING addition of all ROIs
    %    ROI_1 = recurROI          ;q not T1C
    %    ROI_2 = non-recur ROI 5    ;NotqNotT1C
    %    ROI_3 = non Recur ROI 10   ;T1C (lesion)
    ROI_1=load_untouch_nii([pats{ii},'/qNotT1C_mask.nii.gz']);
    ROI_2=load_untouch_nii([pats{ii},'/NotqNotT1C_mask.nii.gz']);
    ROI_3=load_untouch_nii([pats{ii},'/lesion.nii']);
```

```
% Check that T1C and T2F masks exist and if so load them
T1C_ok=0;T2F_ok=0;
    T1C=load_untouch_nii([pats{ii},'/lesion.nii']);
    T1C_ok=1;
    T2F=load_untouch_nii([pats{ii},'/T2F_mask.nii']);
    T2F_ok=1;
% Need to combine the T1C, FLAIR to make a master roi for each patient
master_roi=combineroi(logical(T1C.img),logical(T2F.img),'union');
NEplusCE=load_untouch_nii([pats{ii},'/T2F_mask.nii']);

% Check that spec data exists and load
csi_ok=0;
if exist([pats{ii},'/CSIvoxel_ChoCr.nii'],'file')
    csi1=load_untouch_nii([pats{ii},'/CSIvoxel_ChoNAACr.nii']);
    csi2=load_untouch_nii([pats{ii},'/CSIvoxel_InsCr.nii']);
    csi3=load_untouch_nii([pats{ii},'/CSIvoxel_ChoCr.nii']);
    csi4=load_untouch_nii([pats{ii},'/CSIvoxel_NAACr.nii']);
    csi6=load_untouch_nii([pats{ii},'/CSIvoxel_GSHCr.nii']);
    csi7=load_untouch_nii([pats{ii},'/CSIvoxel_GlxCr.nii']);
    csi9=load_untouch_nii([pats{ii},'/CSIvoxel_LacCr.nii']);
    csi_vox=load_untouch_nii([pats{ii},'/CSIvoxel_VoxNum.nii']);
    csi_ok=1;
end

% Now that data is loaded can start analysis
% Get the pixel coords of all pixels in the master roi
[p_x,p_y,p_z]=ind2sub(size(master_roi),find(master_roi));
% Need the centoid of the qroi
T1C_plusNEC_cent=regionprops(T1C.img,'centroid');
% Round off the value to whole numbers
T1C_plusNEC_cent=(T1C_plusNEC_cent.Centroid);
% Calculate total area and total perimeter of the CE roi
totArea_T1C_plusNEC=nnz(T1C.img);
totPerim_T1C_plusNEC=0;
for jj=1:size(T1C.img,3)
    temp=MFfunc2D(T1C.img(:,:,jj));
    totPerim_T1C_plusNEC=totPerim_T1C_plusNEC+temp(2);
end
```

```
    % Calculate total area and total perimeter of the Master ROI roi
    totArea_NEplusCE=nnz(NEplusCE.img);
    totPerim_NEplusCE_roi=0;
    for jj=1:size(NEplusCE.img,3)
        temp=MFfunc2D(NEplusCE.img(:,:,jj));
        totPerim_NEplusCE_roi=totPerim_NEplusCE_roi+temp(2);
    end
    % Will do an output table for each patient and the p and q rois
seperately
outdata=cell(length(p_x)+1,size(temp_text,2));%cell(11,size(temp_text,2));
    % Fill in the headings
    for jj=1:size(temp_text,2)
        outdata{1,jj}=temp_text{1,jj};
    end
    % Fill in the rows for the q ROI
    for jj=1:length(p_x)
        % Patient characteristics
        % % %outdata{jj+1,1}=pat;
        outdata{jj+1,1}=temp_data(ii,1); % PatientsID
        outdata{jj+1,2}=pats{ii}; %outdata{jj+1,2}=temp_text{kk,2}; %
patient number
        outdata{jj+1,3}=temp_text{ii+1,3}; % PatientID
        outdata{jj+1,4}=temp_data(ii,4); % wbic id
        outdata{jj+1,5}=temp_text{ii+1,5}; % Sex
        outdata{jj+1,6}=temp_data(ii,6); % SexCat
        outdata{jj+1,7}=temp_data(ii,7); % Age =temp_data(ii-1,5)
        outdata{jj+1,8}=temp_data(ii,8); % AgeCat =temp_data(ii-1,5)
        outdata{jj+1,9}=temp_text{ii+1,9}; % EOR
        outdata{jj+1,10}=temp_data(ii,10); % EORCat  MIGHT BE DATA
        outdata{jj+1,11}=temp_data(ii,11); %Gliadel
        outdata{jj+1,12}=temp_data(ii,12); % Status
        outdata{jj+1,13}=temp_data(ii,13); % OS
        outdata{jj+1,14}=temp_data(ii,14); % PFS
        outdata{jj+1,15}=temp_data(ii,15); % MGMT
        outdata{jj+1,16}=temp_data(ii,16); % R132H
        % Total area and perimeter of contrast ROI
        outdata{jj+1,17}=totArea_T1C_plusNEC;
        outdata{jj+1,18}=totPerim_T1C_plusNEC;
```

```
        % Total area and perimeter of FLAIR ROI
        outdata{jj+1,19}=totArea_NEplusCE;
        outdata{jj+1,20}=totPerim_NEplusCE_roi;
        % Relative position of the pixel
        pos=[T1C_plusNEC_cent(2)-p_x(jj),T1C_plusNEC_cent(1)-
p_y(jj),T1C_plusNEC_cent(3)-p_z(jj)];
        outdata{jj+1,21}=pos(1);
        outdata{jj+1,22}=pos(2);
        outdata{jj+1,23}=pos(3);
            % Spectroscopy data
            if csi_ok&&csi_vox.img(p_x(jj),p_y(jj),p_z(jj))~=0;
                outdata{jj+1,31}=csi_vox.img(p_x(jj),p_y(jj),p_z(jj));
                % Vox_num ratio
            end
            if csi_ok&&csi1.img(p_x(jj),p_y(jj),p_z(jj))~=0;
                outdata{jj+1,32}=csi1.img(p_x(jj),p_y(jj),p_z(jj));
                % Cho:NAA ratio
            end
            if csi_ok&&csi2.img(p_x(jj),p_y(jj),p_z(jj))~=0;
                outdata{jj+1,33}=csi2.img(p_x(jj),p_y(jj),p_z(jj));
                % Ins:Cr ratio
            end
            if csi_ok&&csi3.img(p_x(jj),p_y(jj),p_z(jj))~=0;
                outdata{jj+1,34}=csi3.img(p_x(jj),p_y(jj),p_z(jj));
                % Cho:Cr ratio
            end
            if csi_ok&&csi4.img(p_x(jj),p_y(jj),p_z(jj))~=0;
                outdata{jj+1,35}=csi4.img(p_x(jj),p_y(jj),p_z(jj));
                % NAA:Cr ratio
            end
            if csi_ok&&csi6.img(p_x(jj),p_y(jj),p_z(jj))~=0;
                outdata{jj+1,36}=csi6.img(p_x(jj),p_y(jj),p_z(jj));
                % GSH:Cr ratio
            end
            if csi_ok&&csi7.img(p_x(jj),p_y(jj),p_z(jj))~=0;
                outdata{jj+1,37}=csi7.img(p_x(jj),p_y(jj),p_z(jj));
                % Glu+Gln:Cr ratio
            end
```

```
            if csi_ok&&csi9.img(p_x(jj),p_y(jj),p_z(jj))~=0;
                outdata{jj+1,38}=csi9.img(p_x(jj),p_y(jj),p_z(jj));
                % Lac:Cr ratio
            end

     % INside/outside all ROIs
        outdata{jj+1,42}=ROI_1.img(p_x(jj),p_y(jj),p_z(jj));
        outdata{jj+1,43}=ROI_2.img(p_x(jj),p_y(jj),p_z(jj));
        outdata{jj+1,44}=ROI_3.img(p_x(jj),p_y(jj),p_z(jj));
    end
writecsv(outdata,['VoxelWise_CSI_Output/',pats{ii},'_ROIs_voxel_data.csv'])
end
```

Load Data (in R)

#HGG Load Data Algorithm
memory.limit(size=20000)
#Load Data
HGG_001<-read.csv('F:/MRS/VoxelWise_CSI_Output/P001_ROIs_voxel_data.csv', header = TRUE)
(repeat to load all patients' data)
#All patients
ALL_ROI_DATA<-rbind(HGG_001…)
write.csv(ALL_ROI_DATA,'F:/MRS/VoxelWise_CSI_Output/Merged_DATA.csv')
rm()
#End

Algorithm spec_voxel_Jimmy

#HGG Multimodality Statistical Algorithm
#Increase Memory limit
memory.limit(size=20000)
#Load Packages Required
library(ggplot2)
library(lme4)
options(digits=10,width=85, show.signif.stars = FALSE,
        lattice.theme = function() canonical.theme("pdf", color = FALSE),
        str = strOptions(strict.width = "cut"))

```
library(lme4)
library(mcmc)
library(languageR)
library(afex)
library(lmerTest)
library(mtcars)
#Open data
HGG<-read.csv('F:/MRS/VoxelWise_CSI_Output/Merged_DATA.csv', header = TRUE)
#Check data
#edit(HGG)
#Format variables
HGG$Patient.1<-as.factor(HGG$Patient.1)
HGG$voxel_spec<-as.factor(HGG$voxel_spec)
HGG$Age<-as.numeric(as.character(HGG$Age))
HGG$R132H<-as.numeric(as.character(HGG$R132H))
HGG$MGMT<-as.numeric(as.character(HGG$MGMT))
HGG$Status<-as.numeric(as.character(HGG$Status))
HGG$ROI1<-as.numeric(as.character(HGG$ROI1))
HGG$ROI2<-as.numeric(as.character(HGG$ROI2))
HGG$ROI3<-as.numeric(as.character(HGG$ROI3))
HGG$Cho.NAA<-as.numeric(as.character(HGG$Cho.NAA))
HGG$Ins.Cr<-as.numeric(as.character(HGG$Ins.Cr))
HGG$Cho.Cr<-as.numeric(as.character(HGG$Cho.Cr))
HGG$NAA.Cr<-as.numeric(as.character(HGG$NAA.Cr))
HGG$GSH.Cr<-as.numeric(as.character(HGG$GSH.Cr))
HGG$GluGln.Cr<-as.numeric(as.character(HGG$GluGln.Cr))
HGG$Lac.Cr<-as.numeric(as.character(HGG$Lac.Cr))
HGG$OS<-as.numeric(as.character(HGG$OS))
HGG$PFS<-as.numeric(as.character(HGG$PFS))
HGG$rCBV.data[HGG$rCBV.data==0] <- NA
HGG$NIrCBV.data[HGG$NIrCBV.data==0] <- NA
HGG$ADC.data[HGG$ADC.data==0] <- NA
HGG$MD.data[HGG$MD.data==0] <- NA
HGG$p.data[HGG$p.data==0] <- NA
HGG$q.data[HGG$q.data==0] <- NA
#Step 1 - Takes all data and provides single value across each spectroscopy voxel by patient
HGG_spec<-aggregate(.~ voxel_spec + Patient.1,HGG,function(x) c(mean =
mean(x)),na.action=na.pass)
```

```
#Check variables
str(HGG_spec)
#Establish hypotheses
#1. Are there metabolic differences amongst my ROIs?
#-
#Step 2 - Takes all spectroscopy voxels that fall into ROI of interest dependent on what fraction is present in your ROI
#HGG_spec.ROI1<-subset(HGG_spec, ROI1>0.5)
#HGG_spec.ROI2<-subset(HGG_spec, ROI2>0.5)
HGG_spec.ROI3<-subset(HGG_spec, ROI3>0.5)
#Step 3 - Calculates average of all spectroscopy voxels by patient in your ROI of interest
#HGG_spec.ROI1.Final<-aggregate(.~ Patient.1, HGG_spec.ROI1,function(x) c(mean = mean(x,na.rm=TRUE)),na.action=na.pass)
#HGG_spec.ROI2.Final<-aggregate(.~ Patient.1, HGG_spec.ROI2,function(x) c(mean = mean(x,na.rm=TRUE)),na.action=na.pass)
HGG_spec.ROI3.Final<-aggregate(.~ Patient.1, HGG_spec.ROI3,function(x) c(mean = mean(x,na.rm=TRUE)),na.action=na.pass)
#write.csv(HGG_spec.ROI1.Final,'F:/MRS/VoxelWise_CSI_Output/Spec_ROI1.csv')
#write.csv(HGG_spec.ROI2.Final,'F:MRS/VoxelWise_CSI_Output/Spec_ROI2.csv')
write.csv(HGG_spec.ROI3.Final,'F:/MRS/VoxelWise_CSI_Output/Spec_ROI3.csv')
#End
```

References

1. Aerts HJ, Velazquez ER, Leijenaar RT, Parmar C, Grossmann P, Carvalho S, et al: Decoding tumour phenotype by noninvasive imaging using a quantitative radiomics approach. **Nat Commun 5:**4006, 2014
2. Aldape K, Zadeh G, Mansouri S, Reifenberger G, von Deimling A: Glioblastoma: pathology, molecular mechanisms and markers. **Acta Neuropathol 129:**829-848, 2015
3. Almeida JP, Chaichana KL, Rincon-Torroella J, Quinones-Hinojosa A: The value of extent of resection of glioblastomas: clinical evidence and current approach. **Curr Neurol Neurosci Rep 15:**517, 2015
4. Aronen HJ, Pardo FS, Kennedy DN, Belliveau JW, Packard SD, Hsu DW, et al: High microvascular blood volume is associated with high glucose uptake and tumor angiogenesis in human gliomas. **Clinical Cancer Research 6:**2189-2200, 2000
5. Aubry M, De Tayrac M, Etcheverry A, Clavreul A, Saikali S, Menei P, et al: From the core to beyond the margin: a genomic picture of glioblastoma intratumor heterogeneity. **Oncotarget 20:**12094-12109, 2015
6. Balmaceda C, Critchell D, Mao X, Cheung K, Pannullo S, DeLaPaz RL, et al: Multisection 1H magnetic resonance spectroscopic imaging assessment of glioma response to chemotherapy. **J Neurooncol 76:**185-191, 2006
7. Berberat J, McNamara J, Remonda L, Bodis S, Rogers S: Diffusion tensor imaging for target volume definition in glioblastoma multiforme. **Strahlenther Onkol 190:**939-943, 2014
8. Berens ME, Giese A: "...those left behund." Biology and Oncology of Invasive Glioma Cells. **Neoplasia 1:**208-219, 1999
9. Blasel S, Franz K, Ackermann H, Weidauer S, Zanella F, Hattingen E: Stripe-like increase of rCBV beyond the visible border of glioblastomas: site of tumor infiltration growing after neurosurgery. **J Neurooncol 103:**575-584, 2011
10. Boonzaier NR, Piccirillo SG, Watts C, Price SJ: Assessing and monitoring intratumor heterogeneity in glioblastoma: how far has multimodal imaging come? **CNS Oncol. 4:**399-410, 2015
11. Boxerman JL, Schmainda KM, Weisskoff RM: Relative Cerebral Blood Volume Maps Corrected for Contrast Agent Extravasation Significantly Correlate with Glioma Tumor Grade, Whereas Uncorrected Maps Do Not. **AJNR Am J Neuroradiol 22:**859-867, 2006
12. Brandes AA, Franceschi E, Tosoni A, Blatt V, Pession A, Tallini G, et al: MGMT promoter methylation status can predict the incidence and outcome of pseudoprogression after concomitant radiochemotherapy in newly diagnosed glioblastoma patients. **J Clin Oncol 26:**2192-2197, 2008
13. Brandes AA, Tosoni A, Franceschi E, Sotti G, Frezza G, Amista P, et al: Recurrence

pattern after temozolomide concomitant with and adjuvant to radiotherapy in newly diagnosed patients with glioblastoma: correlation With MGMT promoter methylation status. **J Clin Oncol 27:**1275-1279, 2009

14. Brodbelt A, Greenberg D, Winters T, Williams M, Vernon S, Collins VP, et al: Glioblastoma in England: 2007-2011. **Eur J Cancer 51:**533-542, 2015
15. Cancer Genome Atlas Research N: Comprehensive genomic characterization defines human glioblastoma genes and core pathways. **Nature 455:**1061-1068, 2008
16. Castillo M, Smith JK, Kwock L: Correlation of myo-inositol levels and grading of cerebral astrocytomas. **AJNR Am J Neuroradiol 21:**1645-1649, 2000
17. Cha S: Update on Brain Tumor Imaging: From Anatomy to Physiology. **AJNR Am J Neuroradiol 27:**475-487, 2006
18. Chakravarti A, Wang M, Robins HI, Lautenschlaeger T, Curran WJ, Brachman DG, et al: RTOG 0211: a phase 1/2 study of radiation therapy with concurrent gefitinib for newly diagnosed glioblastoma patients. **Int J Radiat Oncol Biol Phys 85:**1206-1211, 2013
19. Chitphakdithai N, Chiang VL, Duncan JS: Non-rigid registration of longitudinal brain tumor treatment MRI. **Conf Proc IEEE Eng Med Biol Soc 2011:**4893-4896, 2011
20. Choi C, Ganji SK, DeBerardinis RJ, Hatanpaa KJ, Rakheja D, Kovacs Z, et al: 2-hydroxyglutarate detection by magnetic resonance spectroscopy in IDH-mutated patients with gliomas. **Nat Med 18:**624-629, 2012
21. Cuddapah VA, Robel S, Watkins S, Sontheimer H: A neurocentric perspective on glioma invasion. **Nat Rev Neurosci 15:**455-465, 2014
22. Davnall F, Yip CS, Ljungqvist G, Selmi M, Ng F, Sanghera B, et al: Assessment of tumor heterogeneity: an emerging imaging tool for clinical practice? **Insights Imaging 3:**573-589, 2012
23. De Bonis P, Anile C, Pompucci A, Fiorentino A, Balducci M, Chiesa S, et al: The influence of surgery on recurrence pattern of glioblastoma. **Clin Neurol Neurosurg 115:**37-43, 2013
24. Deng Z, Yan Y, Zhong D, Yang G, Tang W, Lu F, et al: Quantitative analysis of glioma cell invasion by diffusion tensor imaging. **J Clin Neurosci 17:**1530-1536, 2010
25. Ding S, Miga MI, Noble JH, Cao A, Dumpuri P, Thompson RC, et al: Semiautomatic registration of pre- and postbrain tumor resection laser range data: method and validation. **IEEE Trans Biomed Eng 56:**770-780, 2009
26. Dorner L, Mustafa A, Rohr A, Mehdorn HM, Nabavi A: Growth pattern of tumor recurrence following bis-chloroethylnitrosourea (BCNU) wafer implantation in malignant glioma. **J Clin Neurosci 20:**429-434, 2013
27. Eljamel S: 5-ALA Fluorescence Image Guided Resection of Glioblastoma Multiforme: A Meta-Analysis of the Literature. **Int J Mol Sci 16:**10443-10456, 2015
28. Ellingson BM, Cloughesy TF, Lai A, Nghiemphu PL, Pope WB: Nonlinear registration of

diffusion-weighted images improves clinical sensitivity of functional diffusion maps in recurrent glioblastoma treated with bevacizumab. **Magn Reson Med 67:**237-245, 2012

29. Ellingson BM, Malkin MG, Rand SD, Connelly JM, Quinsey C, LaViolette PS, et al: Validation of functional diffusion maps (fDMs) as a biomarker for human glioma cellularity. **J Magn Reson Imaging 31:**538-548, 2010
30. Ellingson BM, Sahebjam S, Kim HJ, Pope WB, Harris RJ, Woodworth DC, et al: Pretreatment ADC histogram analysis is a predictive imaging biomarker for bevacizumab treatment but not chemotherapy in recurrent glioblastoma. **AJNR Am J Neuroradiol 35:**673-679, 2014
31. Ellingson BM, Wen PY, Cloughesy TF: Modified Criteria for Radiographic Response Assessment in Glioblastoma Clinical Trials. **Neurotherapeutics**, 2017
32. F.H. H, A. P: Assumptions in the radiotherapy of glioblastoma. **Neurology 30:**907-911, 1980
33. Fedorov A, Beichel R, Kalpathy-Cramer J, Finet J, Fillion-Robin JC, Pujol S, et al: 3D Slicer as an image computing platform for the Quantitative Imaging Network. **Magn Reson Imaging 30:**1323-1341, 2012
34. Gevaert O, Mitchell LA, Achrol AS, Xu J, Echegaray S, Steinberg GK, et al: Glioblastoma multiforme: Exploratory radiogenomic analysis by using quantitative image features. **Radiology 273:**168-174, 2014
35. Gilbert MR, Dignam JJ, Armstrong TS, Wefel JS, Blumenthal DT, Vogelbaum MA, et al: A randomized trial of bevacizumab for newly diagnosed glioblastoma. **N Engl J Med 370:**699-708, 2014
36. Gill BJ, Pisapia DJ, Malone HR, Goldstein H, Lei L, Sonabend A, et al: MRI-localized biopsies reveal subtype-specific differences in molecular and cellular composition at the margins of glioblastoma. **Proc Natl Acad Sci U S A 111:**12550-12555, 2014
37. Gillies RJ, Kinahan PE, Hricak H: Radiomics: Images Are More than Pictures, They Are Data. **Radiology 287:**563-577, 2016
38. Gomes J, Zayadi AA, Guzman A: Occupational and environmental risk factors of adult primary brain cancers: A systemic review. **Int J Occup Environ Med 2:**82-111, 2011
39. Grabowski MM, Recinos PF, Nowacki AS, Schroeder JL, Angelov L, Barnett GH, et al: Residual tumor volume versus extent of resection: predictors of survival after surgery for glioblastoma. **J Neurosurg 121:**1115-1123, 2014
40. Grosu AL, Weber WA, Riedel E, Jeremic B, Nieder C, Franz M, et al: L-(methyl-11C) methionine positron emission tomography for target delineation in resected high-grade gliomas before radiotherapy. **Int J Radiat Oncol Biol Phys 63:**64-74, 2005
41. Gupta A, Young RJ, Karimi S, Sood S, Zhang Z, Mo Q, et al: Isolated diffusion restriction precedes the development of enhancing tumor in a subset of patients with

glioblastoma. **AJNR Am J Neuroradiol 32:**1301-1306, 2011

42. Gupta R, Webb-Myers R, Flanagan S, Buckland ME: Isocitrate dehydrogenase mutations in diffuse gliomas: clinical and aetiological implications. **J Clin Pathol 64:**835-844, 2011
43. Hadjipanayis CG, Widhalm G, Stummer W: What is the Surgical Benefit of Utilizing 5-Aminolevulinic Acid for Fluorescence-Guided Surgery of Malignant Gliomas? **Neurosurgery 77:**663-673, 2015
44. Haralick RM, Shamugam K, Dinstein I: Textural features for image classification. **IEEE Transactions on Systems, Man, and Cybernetics 3:**610-621, 1973
45. Hardesty DA, Sanai N: The value of glioma extent of resection in the modern neurosurgical era. **Front Neurol 3:**140, 2012
46. Hegi ME, Diserens AC, Gorlia T, Hamou MF, de Tribolet N, Weller M, et al: MGMT gene silencing and benefit from temozolomide in glioblastoma. **N Engl J Med 352:**997-1003, 2005
47. Heigi ME, Diserens AC, Gorlia T: MGMT gene silencing and benefit from temozolomide in glioblastoma. **N Engl J Med 35:**997-1003, 2005
48. Hentschel SJ, Sawaya R: Optimizing Outcomes With Maximal Surgical Resection of Malignant Glioma. **Cancer Control 10:**109-114, 2003
49. Hilario A, Sepulveda JM, Perez-Nunez A, Salvador E, Millan JM, Hernandez-Lain A, et al: A prognostic model based on preoperative MRI predicts overall survival in patients with diffuse gliomas. **AJNR Am J Neuroradiol 35:**1096-1102, 2014
50. Hiramatsu R, Kawabata S, Furuse M, Miyatake S, Kuroiwa T: Identification of early and distinct glioblastoma response patterns treated by boron neutron capture therapy not predicted by standard radiographic assessment using functional diffusion map. **Radiat Oncol 8:**192, 2013
51. Horska A, Barker PB: Imaging of brain tumors: MR spectroscopy and metabolic imaging. **Neuroimaging Clin N Am 20:**293-310, 2010
52. Hu LS, Ning S, Eschbacher JM, Gaw N, Dueck AC, Smith KA, et al: Multi-Parametric MRI and Texture Analysis to Visualize Spatial Histologic Heterogeneity and Tumor Extent in Glioblastoma. **PLoS One 10:**e0141506, 2015
53. Huang B, Zhang H, Gu L, Ye B, Jian Z, Stary C, et al: Advances in Immunotherapy for Glioblastoma Multiforme. **J Immunol Res 2017:**3597613, 2017
54. Itakura H, Achrol AS, Mitchell LA, Loya JJ, Liu T, Westbroek EM, et al: Magnetic resonance image features identify glioblastoma phenotypic subtypes with distinct molecular pathway activities. **Sci Transl Med 7:**303ra138, 2015
55. Itakura H, Achrol AS, Mitchell LA, Loya JJ, Liu T, Westbroek EM, et al: Magnetic resonance image features identify glioblastoma phenotypic subtypes with distinct molecular pathway activities. **Sci Transl Med 7:**1-10, 2015

56. Jain R, Poisson LM, Gutman D, Scarpace L, Hwang SN, Holder CA, et al: Outcome prediction in patients with glioblastoma by using imaging, clinical, and genomic biomarkers: focus on the nonenhancing component of the tumor. **Radiology 272:**484-493, 2014
57. Jena R, Price SJ, Baker C, Jefferies SJ, Pickard JD, Gillard JH, et al: Diffusion Tensor Imaging: Possible Implications for Radiotherapy Treatment Planning of Patients with High-grade Glioma. **Clinical Oncology 17:**581-590, 2005
58. Jenkinson M, Bannister P, Brady M, Smith S: Improved Optimization for the Robust and Accurate Linear Registration and Motion Correction of Brain Images. **NeuroImage 17:**825-841, 2002
59. Jenkinson M, Beckmann CF, Behrens TE, Woolrich MW, Smith SM: Fsl. **Neuroimage 62:**782-790, 2012
60. Jenkinson M, Smith S: A global optimisation method for robust affine registration of brain images. **Medical Image Analysis 5:**143-156, 2001
61. Julia-sape M, Acosta D, Majos C, Moreno-torres A, Wesseling P, Acebes JJ, et al: Comparison between neuroimaging classifications and histopathological diagnoses using an international multicenter brain tumor magnetic resonance imaging database. **J Neurosurg 105:**6-14, 2006
62. Kallenberg K, Bock HC, Helms G, Jung K, Wrede A, Buhk JH, et al: Untreated glioblastoma multiforme: increased myo-inositol and glutamine levels in the contralateral cerebral hemisphere at proton MR spectroscopy. **Radiology 253:**805-812, 2009
63. Kalpathy-Cramer J, Gerstner ER, Emblem KE, Andronesi OC, Rosen B: Advanced magnetic resonance imaging of the physical processes in human glioblastoma. **Cancer Res 74:**4622-4637, 2014
64. Kantarci K: Imaing biomarkers in neurodegenerative disease. **Proc. Intl. Soc. Mag. Reson. Med.** , 2010
65. Keles GE, Lamborn KR, Chang SM, Prados MD, Berger MS: Volume of residual disease as a predictor of outcome in adult patients with recurrent supratentorial glioblastomas multiforme who are undergoing chemotherapy. **J Neurosurg 100:**41-46, 2004
66. Klein A, Andersson J, Ardekani BA, Ashburner J, Avants B, Chiang MC, et al: Evaluation of 14 nonlinear deformation algorithms applied to human brain MRI registration. **Neuroimage 46:**786-802, 2009
67. Kreis R: Issues of spectral quality in clinical 1H-magnetic resonance spectroscopy and a gallery of artifacts. **NMR Biomed 17:**361-381, 2004
68. Lacroix M, Abi-Said D, Fourney DR, Gokaslan ZL, Shi W, DeMonte F, et al: A multivariate analysis of 416 patients with glioblastoma multiforme: prognosis, extent of resection, and survival. **J Neurosurg 95:**190-198, 2001

69. Law M, Yang S, Wang H, Babb JS, Johnson G, Cha S, et al: Glioma grading: sensitivity, specificity, and predictive values of perfusion MR imaging and proton MR spectroscopic imaging compared with conventional MR imaging. **AJNR Am J Neuroradiol 24:**1989–1998, 2003
70. Lemee JM, Clavreul A, Aubry M, Com E, de Tayrac M, Eliat PA, et al: Characterizing the peritumoral brain zone in glioblastoma: a multidisciplinary analysis. **J Neurooncol 122:**53-61, 2015
71. Lemee JM, Clavreul A, Menei P: Intratumoral heterogeneity in glioblastoma: don't forget the peritumoral brain zone. **Neuro Oncol 17:**1322-1332, 2015
72. Li X, Zhu Y, Kang H, Zhang Y, Liang H, Wang S, et al: Glioma grading by microvascular permeability parameters derived from dynamic contrast-enhanced MRI and intratumoral susceptibility signal on susceptibility weighted imaging. **Cancer Imaging 15:**4, 2015
73. Li YM, Suki D, Hess K, Sawaya R: The influence of maximum safe resection of glioblastoma on survival in 1229 patients: Can we do better than gross-total resection? **J Neurosurg 124:**977-988, 2016
74. Louis DN, Perry A, Reifenberger G, von Deimling A, Figarella-Branger D, Cavenee WK, et al: The 2016 World Health Organization Classification of Tumors of the Central Nervous System: a summary. **Acta Neuropathol 131:**803-820, 2016
75. Lu S, Ahn D, Johnson G, Cha S: Peritumoral diffusion tensor imaging of high-grade gliomas and metastatic brain tumors. **AJNR Am J Neuroradiol 24:**937-941, 2003
76. Lu S, Ahn D, Johnson G, Law M, Zagzag D, Grossmann P: Diffusion-tensor MR imaging of intracranial neoplasia and associated peritumoral edema_ introduction of the tumor infiltration index. **Radiology 232:**221-228, 2004
77. Mabray MC, Barajas RF, Jr., Cha S: Modern brain tumor imaging. **Brain Tumor Res Treat 3:**8-23, 2015
78. McKnight TR, Lamborn KR, Love TD, Berger MS, Chang S, Dillon WP, et al: Correlation of magnetic resonance spectroscopic and growth characteristics within Grades II and III gliomas. **J.Neurosurg. 106:**660-666, 2007
79. Min ZG, Niu C, Rana N, Ji HM, Zhang M: Differentiation of pure vasogenic edema and tumor-infiltrated edema in patients with peritumoral edema by analyzing the relationship of axial and radial diffusivities on 3.0T MRI. **Clin Neurol Neurosurg 115:**1366-1370, 2013
80. Minniti G, Amelio D, Amichetti M, Salvati M, Muni R, Bozzao A, et al: Patterns of failure and comparison of different target volume delineations in patients with glioblastoma treated with conformal radiotherapy plus concomitant and adjuvant temozolomide. **Radiother Oncol 97:**377-381, 2010
81. Moffat BA, Chenevert TL, Meyer CR, McKeever PE, Hall DE, Hoff BA, et al: The

functional diffusion map: an imaging biomarker for the early prediction of cancer treatment outcome. **Neoplasia 8:**259-267, 2006

82. Mohamed A, Zacharaki EI, Shen D, Davatzikos C: Deformable registration of brain tumor images via a statistical model of tumor-induced deformation. **Med Image Anal 10:**752-763, 2006
83. Mohsen LA, Shi V, Jena R, Gillard JH, Price SJ: Diffusion tensor invasive phenotypes can predict progression-free survival in glioblastomas. **Br J Neurosurg 27:**436-441, 2013
84. Mori S, Barker PB: Diffusion Magnetic Resonance Imaging: Its Principals and Application. **The Anatomical Record (NEW ANAT.) 257:**102=109, 1999
85. Mukherjee P, Berman JI, Chung SW, Hess CP, Henry RG: Diffusion tensor MR imaging and fiber tractography: theoretic underpinnings. **AJNR Am J Neuroradiol 29:**632-641, 2008
86. Nabavi A, Black PM, Gering DT, Westin CF, Mehta V: Serial Intraoperative MR Imaging of Brain Shift. **Neurosurgery 48:**787-797, 2001
87. Nazarenko I, Hede SM, He X, Hedren A, Thompson J, Lindstrom MS, et al: PDGF and PDGF receptors in glioma. **Ups J Med Sci 117:**99-112, 2012
88. Ng WH, Wan GQ, Too HP: Higher glioblastoma tumour burden reduces efficacy of chemotherapeutic agents: in vitro evidence. **J Clin Neurosci 14:**261-266, 2007
89. Nithiananthan S, Schafer S, Mirota DJ, Stayman JW, Zbijewski W, Reh DD, et al: Extra-dimensional Demons: a method for incorporating missing tissue in deformable image registration. **Med Phys 39:**5718-5731, 2012
90. Oh S, Kim S: Deformable image registration in radiation therapy. **Radiat Oncol J 35:**101-111, 2017
91. Oliveira FP, Tavares JM: Medical image registration: a review. **Comput Methods Biomech Biomed Engin 17:**73-93, 2014
92. Omuro A, DeAngelis LM: Glioblastoma and other malignant gliomas: a clinical review. **JAMA 310:**1842-1850, 2013
93. Ostrom QT, Bauchet L, Davis FG, Deltour I, Fisher JL, Langer CE, et al: The epidemiology of glioma in adults: a "state of the science" review. **Neuro Oncol 16:**896-913, 2014
94. Ostrom QT, Gittleman H, Liao P, Rouse C, Chen Y, Dowling J, et al: CBTRUS Statistical Report: Primary Brain and Central Nervous System Tumors Diagnosed in the United States in 2007-2011. **Neuro Oncol 16 Suppl 4:**iv1-iv63, 2014
95. Ozawa T, Riester M, Cheng YK, Huse JT, Squatrito M, Helmy K, et al: Most human non-GCIMP glioblastoma subtypes evolve from a common proneural-like precursor glioma. **Cancer Cell 26:**288-300, 2014
96. Paldino MJ, Desjardins A, Friedman HS, Vredenburgh JJ, Barboriak DP: A change in the apparent diffusion coefficient after treatment with bevacizumab is associated with decreased survival in patients with recurrent glioblastoma multiforme. **Br J Radiol**

85:382-389, 2012

97. Parmar C, Grossmann P, Bussink J, Lambin P, Aerts HJ: Machine Learning methods for Quantitative Radiomic Biomarkers. **Sci Rep 5:**13087, 2015
98. Parmar C, Rios Velazquez E, Leijenaar R, Jermoumi M, Carvalho S, Mak RH, et al: Robust Radiomics feature quantification using semiautomatic volumetric segmentation. **PLoS One 9:**e102107, 2014
99. Parsons DW, Jones S, Zhang X, Lin JC, Leary RJ, Angenendt P, et al: An integrated genomic analysis of human glioblastoma multiforme. **Science 321:**1807-1812, 2008
100. Pena A, Green HA, Carpenter TA, Price SJ, Pickard JD, Gillard JH: Enhanced visualization and quantification of magnetic resonance diffusion tensor imaging using the p:q tensor decomposition. **Br J Radiol 79:**101-109, 2006
101. Petrecca K, Guiot MC, Panet-Raymond V, Souhami L: Failure pattern following complete resection plus radiotherapy and temozolomide is at the resection margin in patients with glioblastoma. **J Neurooncol 111:**19-23, 2013
102. Pirazkall A, Mcknight TR, Graves EE, Carol MP, Sneed PK, Wara WW, et al: MR-spectroscopy guided target delineation for high-grade gliomas. **Int J Radiat Oncol Biol Phys 50:**915-928, 2001
103. Preul MC, Caramanos Z, Villemure JG, Shenouda G, LeBlanc R, Langleben A, et al: Using proton magnetic resonance spectroscopic imaging to predict in vivo the response of recurrent malignant gliomas to tamoxifen chemotherapy. **Neurosurgery 46:**306-318, 2000
104. Price SJ: Imaging Markers of Isocitrate Dehydrogenase-1 Mutations in Gliomas. **Neurosurgery 62:**166-170, 2015
105. Price SJ: Improved delineation of glioma margins and regions of infiltration with use of diffusion tensor imaging: an image-guided biopsy study. **American journal of neuroradiology 27:**1969-1974, 2006
106. Price SJ: The role of advanced MR imaging in understanding brain tumour pathology. **Br J Neurosurg 21:**562-575, 2007
107. Price SJ, Allinson K, Liu H, Boonzaier NR, Yan JL, Lupson VC, et al: Less Invasive Phenotype Found in Isocitrate Dehydrogenase–mutated Glioblastomas than in Isocitrate Dehydrogenase Wild-Type Glioblastomas: A Diffusion-Tensor Imaging Study. **Radiology Epub**, 2017
108. Price SJ, Burnet NG, Donovan T, Green HAL, Peña A, Antoun NM, et al: Diffusion Tensor Imaging of Brain Tumours at 3T: A Potential Tool for Assessing White Matter Tract Invasion? **Clinical Radiology 58:**455-462, 2003
109. Price SJ, Gillard JH: Imaging biomarkers of brain tumour margin and tumour invasion. **Br J Radiol 84 Spec No 2:**S159-167, 2011
110. Price SJ, Green HA, Dean AF, Joseph J, Hutchinson PJ, Gillard JH: Correlation of MR

relative cerebral blood volume measurements with cellular density and proliferation in high-grade gliomas: an image-guided biopsy study. **AJNR Am J Neuroradiol 32:**501-506, 2011

111. Price SJ, Pena A, Burnet NG, Jena R, Green HA, Carpenter TA, et al: Tissue signature characterisation of diffusion tensor abnormalities in cerebral gliomas. **Eur Radiol 14:**1909-1917, 2004
112. Price SJ, Waldman AD: Advances in Imaging Brain Cancer.119-140, 2013
113. Price SJ, Young AM, Scotton WJ, Ching J, Mohsen LA, Boonzaier NR, et al: Multimodal MRI can identify perfusion and metabolic changes in the invasive margin of glioblastomas. **J Magn Reson Imaging 43:**487-494, 2016
114. R S, ME H, Idbath A: Tumor treating fields added to standard chemotherapy in newly diagnosed glioblastoma (GBM): final results of a randomized, multicenter, phase III trial, in **2017 Annual Meeting of the American Association for Cancer Research.** Washington, DC., 2017, Vol Abstract LBA AACR CT007
115. Risholm P, Samsett E, Talos IF, Wells W: A non-rigid registration framework that accommodates resection and retraction. **Inf Process Med Imaging 21:**447-458, 2009
116. Rivaz H, Chen SJ, Collins DL: Automatic deformable MR-ultrasound registration for image-guided neurosurgery. **IEEE Trans Med Imaging 34:**366-380, 2015
117. Rumboldt Z, Camach DLA, Lake D, Welsh CT, Castillo M: Apparent diffusion coefficients for differentiation of cerebellar tumors in children. **AJNR Am J Neuroradiol 27:**1362-1369, 2002
118. Sahm F, Capper D, Jeibmann A, Habel A, Paulus W, Troost D, et al: Addressing diffuse glioma as a systemic brain disease with single-cell analysis. **Arch Neurol 69:**523-526, 2012
119. Sanai N, Polley MY, McDermott MW, Parsa AT, Berger MS: An extent of resection threshold for newly diagnosed glioblastomas. **J Neurosurg 115:**3-8, 2011
120. Sawaya RE, Hammound M, Schoppa D, Hess KR, Wu SZ, Shi WM, et al: Neurosurgical outcomes in a modern series of 400 craniotomies for treatment of parenchymal tumors. **Neurosurgery 42:**1044-1055, 1998
121. Scherer HJ: Structural Development in Gliomas. **Am J Cancer 34:**335-351, 1938
122. Schucht P, Knittel S, Slotboom J, Seidel K, Murek M, Jilch A, et al: 5-ALA complete resections go beyond MR contrast enhancement: shift corrected volumetric analysis of the extent of resection in surgery for glioblastoma. **Acta Neurochir (Wien) 156:**305-312; discussion 312, 2014
123. Schuster J, Lai RK, Recht LD, Reardon DA, Paleologos NA, Groves MD, et al: A phase II, multicenter trial of rindopepimut (CDX-110) in newly diagnosed glioblastoma: the ACT III study. **Neuro Oncol 17:**854-861, 2015
124. Scott JN, Brasher PMA, Sevick RJ, Rewcastle NB, Forsyth P: How often are

nonenhancing supratentorial gliomas malignant? A
population study. **Neurology 24:**947-949, 2002
125. Sherriff J, Tamangani J, Senthil L, Cruickshank G, Spooner D, Jones B, et al: Patterns of relapse in glioblastoma multiforme following concomitant chemoradiotherapy with temozolomide. **Br J Radiol 86:**20120414, 2013
126. Shibamoto Y, Baba F, Oda K, Hayashi S, Kokubo M, Ishihara S, et al: Incidence of brain atrophy and decline in mini-mental state examination score after whole-brain radiotherapy in patients with brain metastases: a prospective study. **Int J Radiat Oncol Biol Phys 72:**1168-1173, 2008
127. Simon M, Hosen I, Gousias K, Rachakonda S, Heidenreich B, Gessi M, et al: TERT promoter mutations: a novel independent prognostic factor in primary glioblastomas. **Neuro Oncol 17:**45-52, 2015
128. Smith SM: Fast robust automated brain extraction. **Hum Brain Mapp 17:**143-155, 2002
129. Sontheimer H: A role for glutamate in growth and invasion of primary brain tumors. **Journal of Neurochemistry 105:**287-295, 2008
130. Sotiras A, Davatzikos C, Paragios N: Deformable medical image registration: a survey. **IEEE Trans Med Imaging 32:**1153-1190, 2013
131. Srinivasan GN, Shobha G: Statistical Texture Analysis. **Proceedings of World Academy of Science, Engineering and**
Technology 36:1264-1269, 2008
132. Sternberg EJ, Lipton ML, Burns J: Utility of diffusion tensor imaging in evaluation of the peritumoral region in patients with primary and metastatic brain tumors. **AJNR Am J Neuroradiol 35:**439-444, 2014
133. Steven AJ, Zhuo J, Melhem ER: Diffusion kurtosis imaging: an emerging technique for evaluating the microstructural environment of the brain. **AJR Am J Roentgenol 202:**W26-33, 2014
134. Stummer W, Meinel T, Ewelt C, Martus P, Jakobs O, Felsberg J, et al: Prospective cohort study of radiotherapy with concomitant and adjuvant temozolomide chemotherapy for glioblastoma patients with no or minimal residual enhancing tumor load after surgery. **J Neurooncol 108:**89-97, 2012
135. Stummer W, Pichlmeier U, Meinel T, Wiestler OD, Zanella F, Reulen H-J: Fluorescence-guided surgery with 5-aminolevulinic acid for resection of malignant glioma: a randomised controlled multicentre phase III trial. **The Lancet Oncology 7:**392-401, 2006
136. Stummer W, Reulen HJ, Meinel T, Pichlmeier U, Schumacher W, Tonn JC, et al: Extent of resection and survival in glioblastoma multiforme: identification of and adjustment for bias. **Neurosurgery 62:**564-576; discussion 564-576, 2008
137. Stummer W, van den Bent MJ, Westphal M: Cytoreductive surgery of glioblastoma as

the key to successful adjuvant therapies: new arguments in an old discussion. **Acta Neurochir (Wien) 153:**1211-1218, 2011

138. Stupp R HM, Mason WP: Eff ects of radiotherapy with concomitant and adjuvant temozolomide versus radiotherapy alone on survival in glioblastoma in a randomised phase III study: 5-year analysis of the EORTC-NCIC trial. **Lancet Oncol 10:**459-466, 2009
139. Stupp R, Mason WP, van den Bent MJ, Weller M, Fisher B, Taphoorn MJ, et al: Radiotherapy plus concomitant and adjuvant temozolomide for glioblastoma. **N Engl J Med 352:**987-996, 2005
140. Stupp R, Weber DC: The role of radio- and chemotherapy in glioblastoma. **Onkologie 28:**315-317, 2005
141. Stupp R, Wong ET, Kanner AA, Steinberg D, Engelhard H, Heidecke V, et al: NovoTTF-100A versus physician's choice chemotherapy in recurrent glioblastoma: a randomised phase III trial of a novel treatment modality. **Eur J Cancer 48:**2192-2202, 2012
142. Sugahara T, Korogi Y, Kochi M, Ikushima I, Hirai T, Okuda T, et al: Correlation of MR imaging-determined cerebral blood volume maps with histologic and angiographic determination of vascularity of gliomas. **AJR.American Journal of Roentgenology 171:**1479-1486, 1998
143. Sugahara T, Korogi Y, Kochi M, Ikushima I, Shigematu Y, Hirai T, et al: Usefulness of diffusion-weighted MRI with echo-planar technique in the evaluation of cellularity in gliomas. **J Magn Reson Imaging 9:**53-60, 1999
144. Teng L, Nakada M, Yayashi Y, Yoneyama T, Zhao SG, Hamada JI: **Current Applications of 5-ALA in Glioma Diagnostics and Therapy**: InTech, 2013
145. Teng L, Nakada M, Zhao SG, Endo Y, Furuyama N, Nambu E, et al: Silencing of ferrochelatase enhances 5-aminolevulinic acid-based fluorescence and photodynamic therapy efficacy. **Br J Cancer 104:**798-807, 2011
146. Thomas AA, Arevalo-Perez J, Kaley T, Lyo J, Peck KK, Shi W, et al: Dynamic contrast enhanced T1 MRI perfusion differentiates pseudoprogression from recurrent glioblastoma. **J Neurooncol 125:**183-190, 2015
147. Tran T, Ross B, Lin A: Magnetic resonance spectroscopy in neurological diagnosis. **Neurol Clin 27:**21-60, xiii, 2009
148. Tsien C, Galban CJ, Chenevert TL, Johnson TD, Hamstra DA, Sundgren PC, et al: Parametric response map as an imaging biomarker to distinguish progression from pseudoprogression in high-grade glioma. **J Clin Oncol 28:**2293-2299, 2010
149. Tsougos I, Svolos P, Kousi E, Fountas K, Theodorou K, Fezoulidis I, et al: Differentiation of glioblastoma multiforme from metastatic brain tumor using proton magnetic resonance spectroscopy, diffusion and perfusion metrics at 3 T. **Cancer Imaging 12:**423-436, 2012
150. Van Cauter S, Varaart J, Sijbers J, Peeters RR, Himmelreich U, De Keyzer F, et al: Gliomas:

Diffusion Kurtosis MR Imaging in Grading. **Radiology 263:**492-501, 2012

151. van der Hoorn A, Yan JL, Larkin TJ, Boonzaier NR, Matys T, Price SJ: Validation of a semi-automatic co-registration of MRI scans in patients with brain tumors during treatment follow-up. **NMR Biomed 29:**882-889, 2016
152. van Dijken BR, van Laar PJ, Holtman GA, van der Hoorn A: Diagnostic accuracy of magnetic resonance imaging techniques for treatment response evaluation in patients with high-grade glioma, a systematic review and meta-analysis. **Eur Radiol [Epub ahead of print]**, 2017
153. Verhaak RG, Hoadley KA, Purdom E, Wang V, Qi Y, Wilkerson MD, et al: Integrated genomic analysis identifies clinically relevant subtypes of glioblastoma characterized by abnormalities in PDGFRA, IDH1, EGFR, and NF1. **Cancer Cell 17:**98-110, 2010
154. Waldman AD, Jackson A, Price SJ, Clark CA, Booth TC, Auer DP, et al: Quantitative imaging biomarkers in neuro-oncology. **Nat Rev Clin Oncol 6:**445-454, 2009
155. Walker C, Baborie A, Crooks D, Wilkins S, Jenkinson MD: Biology, genetics and imaging of glial cell tumours. **Br J Radiol 84 Spec No 2:**S90-106, 2011
156. Wang W, Steward CE, Desmond PM: Diffusion Tensor Imaging in Glioblastoma Multiforme and Brain Metastases: The Role of p, q, L, and Fractional Anisotropy. **American Journal of Neuroradiology 30:**203-208, 2008
157. Wang Z, Bovik AC: Image Quality Assessment: From Error Visibility to Structural Similarity. **IEEE TRANSACTIONS ON IMAGE PROCESSING 13:**600-612, 2014
158. Warmuth C, Gunther M, Zimmer C: Quantification of Blood Flow in Brain Tumors: Comparsion of Arterial Spin Label and Dynamic Susceptibility-weighted Contrast Enhanced MR Imaging. **Radiology 288:**523-532, 2003
159. Wen PY, Cloughesy TF, Ellingson BM, Reardon DA, Fine HA, Abrey L, et al: Report of the Jumpstarting Brain Tumor Drug Development Coalition and FDA clinical trials neuroimaging endpoint workshop (January 30, 2014, Bethesda MD). **Neuro Oncol 16:**vii36-vii47, 2014
160. Wen PY, Kesari S: Malignant Gliomas in Adults. **N Engl J Med 359:**492-507, 2008
161. Wen PY, Macdonald DR, Reardon DA, Cloughesy TF, Sorensen AG, Galanis E, et al: Updated response assessment criteria for high-grade gliomas: response assessment in neuro-oncology working group. **J Clin Oncol 28:**1963-1972, 2010
162. Westphal M, Hilt DC, Bortey E, Delavaut P, Olivares R, Warnke PC, et al: A phase 3 trial of local chemotherapy with biodegradable carmustine (BCNU) wafers (Gliadel wafers) in patients with primary malignant glioma. **Neuro Oncol 5:**79-88, 2003
163. Wijnen JP, Idema AJ, Stawicki M, Lagemaat MW, Wesseling P, Wright AJ, et al: Quantitative short echo time 1H MRSI of the peripheral edematous region of human brain tumors in the differentiation between glioblastoma, metastasis, and meningioma. **J Magn Reson Imaging 36:**1072-1082, 2012

164. Wilson TA, Karajannis MA, Harter DH: Glioblastoma multiforme: State of the art and future therapeutics. **Surg Neurol Int 5:**64, 2014
165. Xie Q, Mittal S, Berens ME: Targeting adaptive glioblastoma: an overview of proliferation and invasion. **Neuro Oncol 16:**1575-1584, 2014
166. Yan JL, van der Hoorn A, Larkin TJ, Boonzaier NR, Matys T, Price SJ: Extent of resection of peritumoral diffusion tensor imaging-detected abnormality as a predictor of survival in adult glioblastoma patients. **J Neurosurg 126:**234-241, 2017
167. Yang X, Tridandapani S, Beitler J, Yu DS, Yoshida EJ, Curran WJ, et al: Ultrasound GLCM texture analysis of radiation-induced parotid-gland injury in head-and-neck cancer radiotherapy: An in vivo study of late toxicity. **Am Assoc Phys Med 39:**5732-5739, 2012
168. Young RM, Simon MC: Untuning the tumor metabolic machine: HIF-alpha: pro- and antitumorigenic? **Nat Med 18:**1024-1025, 2012
169. Zacharaki EI, Hogea CS, Shen D, Biros G, Davatzikos C: Non-diffeomorphic registration of brain tumor images by simulating tissue loss and tumor growth. **Neuroimage 46:**762-774, 2009
170. Zhang Y, Brady M, Smith S: Segmentation of brain MR images through a hidden Markov random field model and the expectation-maximization algorithm. **IEEE Trans Med Imaging 20:**45-57, 2001
171. Zou Y, Bai HX, Wang Z, Yang L: Comparison of immunohistochemistry and DNA sequencing for the detection of IDH1 mutations in gliomas. **Neuro Oncol 17:**477-478, 2015